



Dissipative Solitons: The Structural Chaos And The Chaos Of Destruction

Vladimir L. Kalashnikov

Institute for Photonics, Technical University of Vienna, Vienna, Austria
(E-mail: kalashnikov@tuwien.ac.at)

Abstract. Dissipative soliton, that is a localized and self-preserving structure, develops as a result of two types of balances: self-phase modulation vs. dispersion and dissipation vs. nonlinear gain. The contribution of dissipative, i.e. environmental, effects causes the complex “far from equilibrium” dynamics of a soliton: it can develop in a localized structure, which behaves chaotically. In this work, the chaotic laser solitons are considered in the framework of the generalized complex nonlinear Ginzburg-Landau model. For the first time to our knowledge, the model of a femtosecond pulse laser taking into account the dynamic gain saturation covering a whole resonator period is analyzed. Two main scenarios of chaotization are revealed: i) multipusing with both short- and long-range forces between the solitons, and ii) noiselike pulse generation resulting from a parametrical interaction of the dissipative soliton with the linear dispersive waves. The noiselike pulse is characterized by an extremely fine temporal and spectral structure, which is similar to that of optical supercontinuum.

Keywords: Dissipative soliton, Complex nonlinear Ginzburg-Landau equation, Chaotic soliton dynamics.

1 Introduction

The nonlinear complex Ginzburg-Landau equation (NCGLE) has a lot of applications in quantum optics, modeling of Bose-Einstein condensation, condensate-matter physics, study of non-equilibrium phenomena, and nonlinear dynamics, quantum mechanics of self-organizing dissipative systems, and quantum field theory [1]. In particular, this equation being a generalized form of the so-called master equation provides an adequate description of pulses generated by a mode-locked laser [2]. Such pulses can be treated as the dissipative solitons (DSs), that are the localized solutions of the NCGLE [3]. It was found, that the DS can demonstrate a highly non-trivial dynamics including formation of multi-soliton complexes [4], soliton explosions [5], noise-like solitons [6], etc. The resulting structures can be very complicated and consist of strongly or weakly interacting solitons (so-called soliton molecules and gas) [7] as well as the short-range noise-like oscillations inside a larger wave-packet [8]. The nonlinear dynamics of these structures can cause both regular and chaotic-like behavior.

In this article, the different scenarios of the soliton structural chaos will be considered for the chirped DSs formed in the all-normal group-delay dis-



persion region [9]. The first scenario is an appearance of the chaotic fine graining of DS. For such a structure, the mechanism of formation is identified with the parametric instability caused by the resonant interaction of DS with the continuum. The second scenario is formation of the multi-soliton complexes governed by both short-range forces (due to solitons overlapping) and long-range forces (due to gain dynamics). The underlying mechanism of formation is the continuum amplification, which results in the soliton production or/and the dynamical coexistence of DSs with the continuum.

2 Chirped dissipative solitons of the NCGLE

Formally, the NCGLE consists of the nondissipative (hamiltonian) and dissipative parts. The nondissipative part can be obtained from variation of the Lagrangian [10]:

$$\mathcal{L} = \frac{i}{2} \left[A^*(x, t) \frac{\partial A(x, t)}{\partial t} - A(x, t) \frac{\partial A^*(x, t)}{\partial t} \right] + \frac{\beta}{2} \frac{\partial A(x, t)}{\partial t} \frac{\partial A^*(x, t)}{\partial t} - \frac{\gamma}{2} |A(x, t)|^2, \quad (1)$$

where $A(x, t)$ is the field envelope depending on the propagation distance x and the “transverse” coordinate t (that is the local time in our case), β is the group-delay dispersion (GDD) coefficient (negative for the so-called normal dispersion case), and γ is the self-phase modulation (SPM) coefficient [11]. The dissipative part is described by the driving force:

$$\mathcal{Q} = -i\Gamma A(x, t) + i \frac{\rho}{1 + \sigma \int_{-\infty}^{\infty} |A|^2 dt'} \left[A(x, t) + \tau \frac{\partial^2}{\partial t^2} A(x, t) \right] + i\kappa \left[|A(x, t)|^2 - \zeta |A(x, t)|^4 \right] A(x, t), \quad (2)$$

where Γ is the net-dissipation (loss) coefficient, ρ is the saturable gain (σ is the inverse gain saturation energy if the energy E is defined as $E \equiv \int_{-\infty}^{\infty} |A|^2 dt'$), τ is the parameter of spectral dissipation (so-called squared inverse gainband width), and κ is the parameter of self-amplitude modulation (SAM). The SAM is assumed to be saturable with the corresponding parameter ζ .

Then, the desired CNGLE can be written as

$$\begin{aligned} & i \frac{\partial A(x, t)}{\partial x} - \frac{\beta}{2} \frac{\partial^2}{\partial t^2} A(x, t) - \gamma |A(x, t)|^2 A(x, t) = \\ & = -i\Gamma A(x, t) + i \frac{\rho}{1 + \sigma \int_{-\infty}^{\infty} |A|^2 dt'} \left[A(x, t) + \tau \frac{\partial^2}{\partial t^2} A(x, t) \right] + \\ & \quad + i\kappa \left[|A(x, t)|^2 - \zeta |A(x, t)|^4 \right] A(x, t). \end{aligned} \quad (3)$$



Eq. (3) is not integrable and only sole exact soliton-like solution is known for it [11,12]. Nevertheless, the so-called variational method [10] allows exploring the solitonic sector of (3). The force-driven Lagrange-Euler equations

$$\frac{\partial \int_{-\infty}^{\infty} \mathcal{L} dt}{\partial \mathbf{f}} - \frac{\partial}{\partial x} \frac{\partial \int_{-\infty}^{\infty} \mathcal{L} dt}{\partial \mathbf{f}} = 2\Re \int_{-\infty}^{\infty} \mathcal{Q} \frac{\partial A}{\partial \mathbf{f}} dt \quad (4)$$

allow obtaining a set of the ordinary first-order differential equations for a set \mathbf{f} of the soliton parameters if one assumes the soliton shape in the form of some trial function $A(x, t) \approx \mathcal{F}(t, \mathbf{f})$. One may chose [13]

$$\mathcal{F} = a(x) \operatorname{sech}\left(\frac{t}{T(x)}\right) \exp\left[i\left(\phi(x) + \psi(x) \ln\left(\operatorname{sech}\left(\frac{t}{T(x)}\right)\right)\right)\right], \quad (5)$$

with $\mathbf{f} = \{a(x), T(x), \phi(x), \psi(x)\}$ describing amplitude, width, phase, and chirp of the soliton, respectively.

Substitution of (5) into (4) results in four equations for the soliton parameters. These equations are completely solvable for a steady-state propagation (i.e. when $\partial_x a = \partial_x T = \partial_x \psi = 0, \partial_x \phi \neq 0$). The analysis demonstrates that the solitonic sector can be completely characterized by two-dimensional master diagram, that is the DS is two-parametrical and the corresponding dimensionless parameters are $c \equiv \tau\gamma/|\beta|\kappa$ and the “energy” $\mathcal{E} \equiv Eb\sqrt{\kappa\zeta}/\tau$ (here $b \equiv \gamma/\kappa$).

The master diagram is shown in Fig. 1. The curves correspond to the stability threshold defined as $\Gamma - \rho / \left(1 + \sigma \int_{-\infty}^{\infty} |A|^2 dt\right) = 0$. Positivity of this value provides the vacuum stability. As will be shown, the vacuum destabilization is main source of the soliton instability causing, in particular, the chaotic dynamics. The master diagram in Fig. 1 reveals a very simple asymptotic for the maximum energy of DS: $E \approx 17 |\beta| / \sqrt{\kappa\zeta\tau}$. The continuum rises above this energy.

3 Resonant excitation of continuum

The stability threshold shown in Fig. 1 corresponds to an unperturbed DS of (3). The physically meaningful perturbation results from a higher-order dispersion correction to the Lagrangian: $\mathcal{L} = \mathcal{L}_0 + \frac{i\delta}{2} \frac{\partial^2 A}{\partial t^2} \frac{\partial A^*}{\partial t}$, where \mathcal{L}_0 is the unperturbed Lagrangian (1) and δ is the third-order dispersion (TOD) parameter.

The DS of unperturbed Eq. (3) does not interact with the continuum and the collapse-like instability is suppressed by $\zeta > 0$. Nevertheless, the DS peak power on the asymptotic stability threshold of Fig. 1 is $\approx 1.1/\zeta > 1/\zeta$ that, in accordance with [8] has to result in the chaotic behavior. However, such a chaotic layer in the vicinity of stability threshold has not been revealed by our numerical simulations. A possible explanation is that the solitonic sector (5)

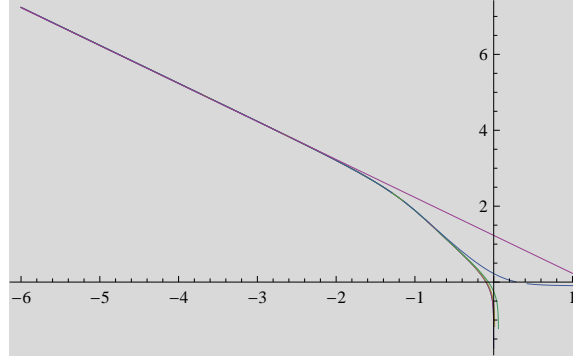


Fig. 1. Master diagram for the chirped DS. The vertical axis is $\log_{10} \mathcal{E}$ and the horizontal axis is $\log_{10} c$. The stability thresholds are shown for $b=100$ (brown), 5 (green), 2 (cyan) and the asymptotic $\mathcal{E} = 17/c$ (magenta). The DS is stable below the corresponding curves.

is not isolated and there exists another stable solitonic sector corresponding to the DS with the so-called “finger-like” spectra [9,14]. Such a spectrum has a main part of the power in the vicinity of the spectrum center. As a result, a spectral loss decreases that corresponds to energy growth close to the boundary of the DS stability. In turn, a concentration of power close to the spectrum center corresponds to a similar power concentration around a pulse peak in the time domain, that allows the stable DSs with the peak powers $> 1/\zeta$ and, thus, a new solitonic sector appears. Such a sector corresponds to

$$\mathcal{F} = \frac{a(x)}{\sqrt{\theta(x) + \cosh\left(\frac{t}{T(x)}\right)}} \exp \left[i \left(\phi(x) + \psi(x) \ln \left(\theta(x) + \cosh \left(\frac{t}{T(x)} \right) \right) \right) \right] \quad (6)$$

with $\theta(x) > 1$ and requires a further exploration.

Nevertheless for any solitonic sector, $\delta \neq 0$ can result in an appearance of interaction with the continuum at some frequency [15]. Hence, the stability threshold becomes lower than that shown in Fig. 1. As the resonance occurs in the spectral domain, an exploration of the DS spectrum is most informative in this case. The numerical results corresponding to a mode-locked Cr:ZnSe oscillator [16] are shown in Fig. 2. Non-zero δ can be treated as a frequency-dependence of net-GDD (dashed curves). As a result of such dependence, the zero GDD shifts towards the DS spectrum with the growing $|\delta|$ (black solid curve and black dashed line correspond to $\delta = 0$). The vertex of truncated DS spectrum (solid curves) traces the GDD line (dashed lines) logarithmically. When the zero GDD (see orange dashed line) reaches the DS spectrum, the resonant generation of continuum (dispersive wave) begins (longer wavelength

side of the spectrum demonstrates such a wave; orange and violet curves in Fig. 2).

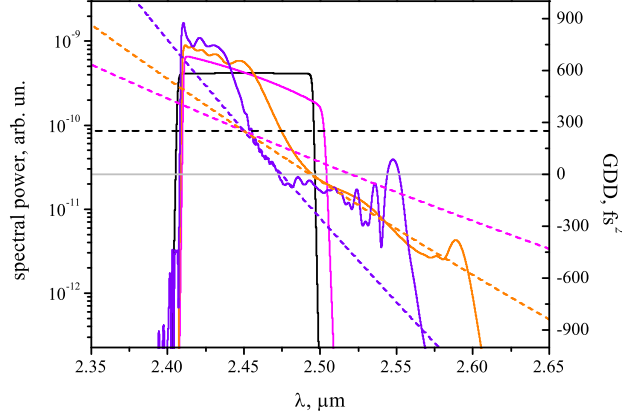


Fig. 2. Spectra of the chirped DSs (solid curves) corresponding to the different net-GDD (dashed curves). The GDD slope depends on the TOD value.

As a result of resonant interaction with the dispersive wave, when the zero GDD approaches the central wavelength of an unperturbed DS spectrum ($\approx 2.5 \mu\text{m}$ in our case), the irregular beatings of the DS peak power develop (violet curve in Fig. 3, left). In the time domain, the resonant interaction forms a fine (femtosecond) structure in the vicinity of pulse peak (Fig. 3, right). Such a structure enhances with the shift of zero GDD towards the central wavelength of an unperturbed DS spectrum and spreads to a whole spectrum. As a result, the DS envelope becomes to be strongly distorted (gray curve Fig. 3, right) and disintegrates.

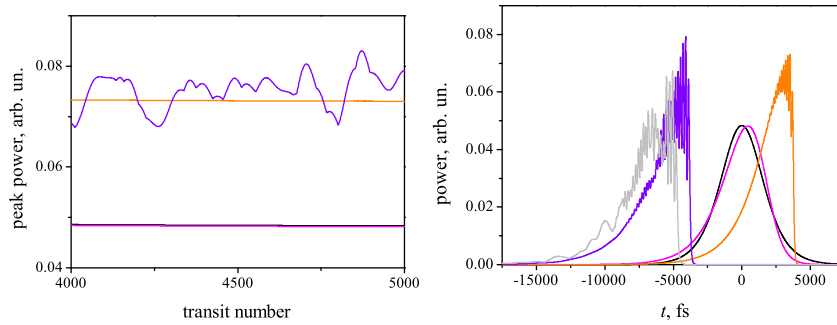


Fig. 3. Peak power evolution (left) and DS envelopes (right) for the GDD curves of Fig. 2.

4 Nonresonant excitation of continuum

Another correction to (3) is defined by the energy-dependent gain/loss terms in (2). As a result, a large-scale solitonic (multi-soliton) structure appears (Fig. 4) and, the picosend satellites appear both nearby (few picosecond) the main pulse and far (nanoseconds) from it. Strong interaction between the pulses with the contribution from a gain dynamics results in a chaotic behavior. For the chirped DS, the dynamic loss/gain saturation causes a parametric resonance, as well. Hence, the DS becomes finely structured [17].

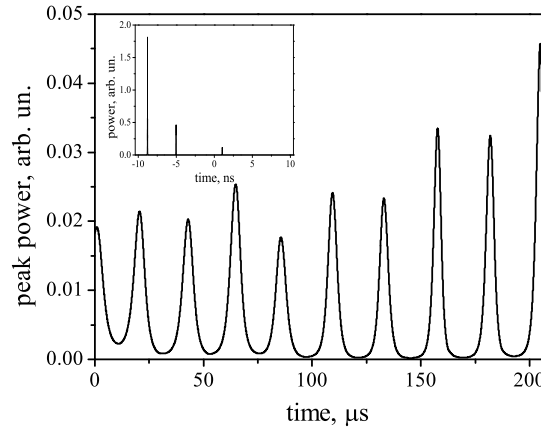


Fig. 4. Multiple DS evolution in the presence of the dynamic gain saturation.

5 Conclusion

Unlike a classical soliton, a chirped DS possesses a nontrivial internal structure. As a result, the dynamics of such DS can be very complicated. In particular, a chaotic interaction with an excited vacuum (continuum) develops. Such an interaction can be nonresonant (as it takes a place for the Schrödinger soliton) and resonant. The last results in the chaotic behavior with a strict localization of the DS spectrum and power envelope even for a “far from equilibrium” regime. The strong localization of a chaotic structure results in the chirped DS, which remains to be traceable in an even chaotic regime. Such a traceability promises a lot of applications in the spectroscopy, for instance.

Acknowledgements

This work was supported by the Austrian Science Foundation (FWF project P20293).



References

- 1.I.S. Aranson, L. Kramer. The world of the complex Ginzburg-Landau equation. *Rev. Mod. Phys.*, 74:99–143, 2002.
- 2.F.X. Kärtner, U. Morgner, Th. Schibli, R. Ell, H.A. Haus, J.G. Fujimoto, E.P. Ippen. Few-cycle pulses directly from a laser. In F.X. Kärtner, editor, *Few-cycle Laser Pulse Generation and its Applications*, pages 73-178, Berlin, 2004. Springer.
- 3.N. Akhmediev, A. Ankiewicz. Dissipative solitons in the complex Ginzburg-Landau and Swift-Hohenberg equations. In N. Akhmediev, A. Ankiewicz, editors, *Dissipative Solitons*, pages 1–18, Berlin, 2005. Springer.
- 4.J.M. Soto-Crespo, Ph. Grelu. Temporal multi-soliton complexes generated by passively mode-locked lasers. In N. Akhmediev, A. Ankiewicz, editors, *Dissipative Solitons*, pages 207–240, Berlin, 2005. Springer.
- 5.S.T. Cundiff. Soliton dynamics in mode-locked lasers. In N. Akhmediev, A. Ankiewicz, editors, *Dissipative Solitons*, pages 183–206, Berlin, 2005. Springer.
- 6.M. Horowitz, Y. Barad, Y. Silberberg. Noiselike pulses with a broadband spectrum generated from an erbium-doped fiber laser. *Opt. Letters*, 22:799–801, 1997.
- 7.A. Zavyalov, R. Iliev, O. Egorov, F. Lederer. Dissipative soliton molecules with independently evolving or flipping phases in mode-locked fiber lasers. *Phys. Rev. A*, 80:043829, 2009.
- 8.S. Kobtsev, S. Kukarin, S. Smirnov, S. Turitsyn, A. Latkin. Generation of double-scale femto/pico-second optical lumps in mode-locked fiber lasers. *Optics Express*, 17:20707–20713, 2009.
- 9.V.L. Kalashnikov. Chirped dissipative solitons. In L.F. Babichev, V.I. Kuvshinov, editors, *Nonlinear Dynamics and Applications*, pages 58–67, Minsk, 2010. Republican Institute of higher school.
- 10.D. Anderson, M. Lisak, and A. Berntson. A variational approach to nonlinear equations in optics. *Pramana J. Phys.* 57:917-936, 2001.
- 11.N. Akhmediev, A. Ankiewicz. *Solitons: Nonlinear Pulses and Beams*, London, 1997. Chapman&Hall.
- 12.R. Conte, M. Musette. Solitary waves of nonlinear nonintegrable equations. In N. Akhmediev, A. Ankiewicz, editors, *Dissipative Solitons*, pages 373–406, Berlin, 2005. Springer.
- 13.V.L. Kalashnikov, A. Apolonski. Energy scalability of mode-locked oscillators: a completely analytical approach to analysis. *Optics Express*, 18:25757–25770, 2010.
- 14.E. Podivilov, V.L. Kalashnikov. Heavily-chirped solitary pulses in the normal dispersion region: new solutions of the cubic-quintic complex Ginzburg-Landau equation. *JETP Letters*, 82:467–471, 2005.
- 15.V.L. Kalashnikov. Dissipative solitons: perturbations and chaos formation. In *Proceedings of 3rd Chaotic Modeling and Simulation International Conference*, pages 69-1–8. 1-4 June, 2010, Chania, Greece.
- 16.V.L. Kalashnikov, E. Sorokin. Soliton absorption spectroscopy. *Phys. Rev. A*, 81:033840-1–8, 2010.
- 17.V.L. Kalashnikov. Chirped-pulse oscillators: an impact of the dynamic gain saturation. arXiv:0807.1050 [physics.optics].





Simulation of Content-Driven Cosmic Expansion

John Kastl

US Navy, Keyport WA, USA
E-mail: john.kastl@navy.mil

Abstract:

The standard cosmic expansion model, in which gravity acts to decelerate the expansion, has its problems. This paper explores an alternative model, which has a content-driven mechanism, and in which gravity does not play a role in the overall expansion. Cosmic expansion was simulated with a three-step iterative algorithm, three fundamental parameters, and Planck-scale initial conditions. Model characteristics include self-regulated expansion, causal mechanisms for the Big Bang and Inflation, non-fundamental time (t), parametric Ht (the product of t and the Hubble parameter (H)), a dynamic deceleration parameter (q), Ht lagging $(1+q)^{-1}$, and attractors in the q - Ht phase diagram. Simulation results support refinement of the standard model and open the door for similarly exploring and comparing other cosmic expansion models.

Key words: cosmology, modeling, simulation, complex systems

1. Introduction

Proponents of the most generally accepted cosmic expansion model (the standard model) posit that gravity has acted to decelerate the expansion since the Universe burst forth from a singularity at time zero (Shu 1982). The expansion metric is the scale factor (R), which has units of length. The deceleration metric is the dimensionless deceleration parameter ($q = -a \cdot \ddot{a} / \dot{a}^2$, where $a = R/R_{\text{now}}$).

The standard model has its issues, including singularity-generated infinities at time zero, its false premise (Gimenez 2009) that gravity plays a role in the overall expansion, and its lack of causal mechanisms for the Big Bang and Inflation. Also, accelerated expansion, as indicated by supernovae observations (Riess et al. 1998, Perlmutter et al. 1999), cannot be found in the standard model. Saul Perlmutter (2003), referring to fine tuning coincidences and the mysterious substances of dark energy and dark matter, writes that it seems likely that we are missing some fundamental physics and one is tempted to speculate that these ingredients are add-ons, like the Ptolemaic epicycles, to preserve an incomplete theory.

This paper explores a content-driven approach to cosmic expansion (Kastl 2011) and argues that indications of current acceleration are in error. An iterative algorithm, which focuses on Mach's Principle, the past lightcone, and an hypothesis that the increasing content on our past lightcone provides the causal mechanism for cosmic expansion, is constructed to numerically simulate cosmic expansion. The Big Bang is simulated at Planck time and Inflation is found in the Matter Era.



2. Model and Simulation

2.1 Algorithm. The algorithm for content-driven expansion (figure 1) is iterative and discreet and does not require Nature to understand complex math or perform massive computations. Time (t), which was neither in the iterative loop nor one of the three fundamental parameters, was progressed using $\Delta t = R/c$, where R is the cosmic scale factor and c is the speed of light.

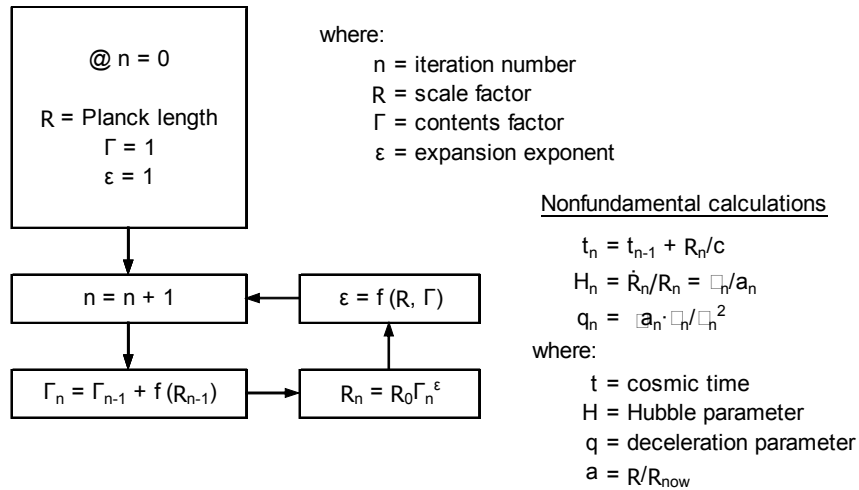


Figure 1. Iterative expansion algorithm. The three fundamental parameters (R, Γ, and ε) are in the three-step iterative loop – the iteration number (n) was not in the actual calculations. Dimensionless Γ and ε have an initial value of 1. With R₀ set to Planck length, t₀=Planck time, □₀=c, H₀=1/t₀, Ht₀=1, ä₀=0, and q₀=0.

2.2 Progressing time with $\Delta t = R/c$

R/c is the time for light to traverse the distance R. With R_{now}≈20Mly, Δt_{now} (today's tick of the clock) is ~20My (Δt=R/c). Midway through the development of the simulation, Δt=R/c was replaced when a more supportable method was found in Δt=ΔR/R/H, which follows from $H \equiv \dot{R}/R$. Surprisingly, replacing Δt=R/c with Δt=ΔR/R/H had no impact on the simulation, and the simpler Δt=R/c was reinstated.

For an object with velocity (v), relativistic $\Delta t = R \cdot (1 - (v/c)^2)^{0.5} / c$ would be more accurate. If v for the Solar System were 630km·s⁻¹ (Jones 2004) relative to the microwave background radiation, using the relativistic Δt in place of Δt=R/c would not have significantly altered the simulation's results.

2.3 Expansion exponent

To calculate ε, the local ε (ε_{local}) was first progressed from 1 to infinity using:

$$\epsilon_{\text{local}}(R) = 10^{((\ln(R/R_0))^3 / (17000 + (\ln(R/R_0))^{2.95}))}$$

A content-allocated average of past values of ε_{local} was then calculated using:



$$\varepsilon_n = (\varepsilon_{n-1} \cdot \Gamma_{n-1} + \varepsilon_{\text{local}}) / \Gamma_n$$

2.4 Asymptotic q_∞ and Ht_∞

Theory-connected asymptotic q_∞ and Ht_∞ were in sync with GR (figure 2). At radiation-dominated Planck time, $q_\infty=1$ and $Ht_\infty=1/2$. For matter-dominated expansion, $q_\infty=1/2$ and $Ht_\infty=2/3$. In the distant future, q_∞ approached 0 and Ht_∞ approached 1 (vacuum-dominated).

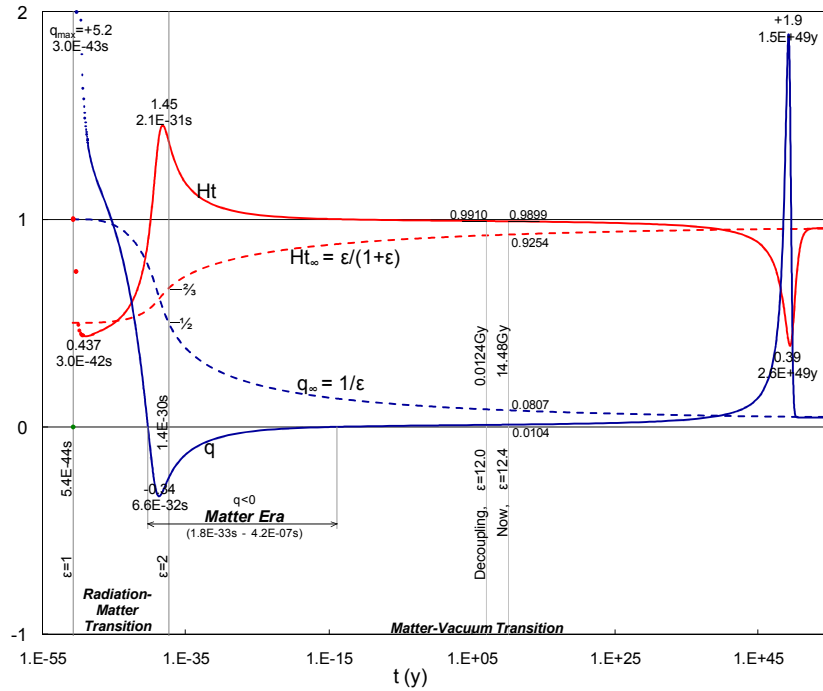


Figure 2. $q(t)$ and $Ht(t)$ and $q_\infty(t)$ and $Ht_\infty(t)$. The Matter Era is defined by negative q . The Radiation-Matter Transition and Matter-Vacuum Transition are delineated by $\varepsilon=2$.

2.5 Dynamic q and Ht

Distinct from theory-connected q_∞ and Ht_∞ , q and Ht projected a dynamic expansion (figure 2). From the non-zero Planck-scale beginning of time, q cycles from 0 to more than 5 to -0.34 to +1.9 and back to 0, and Ht cycles from 1 to 0.437 to 1.45 to 0.39 and back to 1. In all cases, Ht_{max} lagged q_{min} and Ht_{min} lagged q_{max} . In contrast to past and future expansion, in the current epoch the expansion was effectively ‘coasting’ with $q \approx 0$ and $Ht \approx 1$. The current epoch is defined here as the time since Decoupling at redshift $z=1090.88$ (Hinshaw et al. 2009) when the primordial soup cleared.



2.6 Inflation, the Matter Era, and era transitions

Early in the development of the simulation, the Matter Era was roughly defined as beginning with $Ht_e=0.583$ (half way between $1/2$ and $2/3$) and ending with $Ht_e=0.833$ (half way between $2/3$ and 1). When a definitive time was found for $\varepsilon=2$ (associated with the Matter Era's $Ht_e=2/3$), a line of demarcation between the Radiation-Matter Transition and the Matter-Vacuum Transition was established, and the three eras were abandoned. Later came the revelation that when q was negative, Ht_∞ rose from 0.562 to 0.881 – roughly the same values that had previously been used to define the Matter Era. Linking the Matter Era to Inflation, the three eras were reinstated.

2.7 Time of Decoupling

By setting redshift (z) to zero at $t_{\text{now}}=14.48\text{Gy}$ and using R to track z (using $z+1=R_{\text{now}}/R$) to 1090.88 (Hinshaw et al. 2009), the time of Decoupling was found to be 12.4My . The current literature typically places the time of Decoupling at much earlier 0.3My to 1.0My (e.g., 0.377My (Hinshaw et al. 2009)). The only other outlier is a $Ht=1$ coasting model's 13My (Gimenez 2009), which is in relative agreement with this paper's $Ht_{\text{now}}=0.9899$ and 12.4My time of Decoupling. Hinshaw's 0.377My appears to be based on $z+1=(t_{\text{now}}/t)^{Ht}$, $t_{\text{now}}=13.72\text{Gy}$, and $Ht=2/3$, although Hinshaw's $H_{\text{now}}=70.5\text{km}\cdot\text{s}^{-1}\cdot\text{Mpc}^{-1}$ ($=1/13.87\text{Gy}$) and $t_{\text{now}}=13.72\text{Gy}$ produce $Ht_{\text{now}}=0.9892$, not $2/3$.

2.8 q-Ht phase diagram

Dynamic q - Ht fluctuations appeared in the q - Ht phase diagram (figure 3) as large lobes that roughly took on the shape of the attractor rail. Paralleling the finding that Ht_{max} lagged q_{min} and Ht_{min} lagged q_{max} , with the q - Ht trace orbiting clockwise around a moving attractor on the attractor rail, Ht lagged $(1+q)^{-1}$. Four exceptions to the Ht -Lag rule occurred when $\text{Lag}=0$ (i.e., when the q - Ht trace contacted the Zero Lag Curve).

Lag was found to be $\beta \cdot t^2 \cdot d^2 Ht / dt^2$, where $\beta=0.421$ now and $\beta=0.458$ at Decoupling. Lag now and at Decoupling are near zero and virtually unchanged (0.000177 versus 0.000165) and $t^2 \cdot d^2 Ht / dt^2$ has changed only modestly (0.00042 now versus 0.00036 at Decoupling). As evidenced by the large lobes in the Radiation and Vacuum eras, early-Radiation and late-Vacuum Lag is more dynamic.

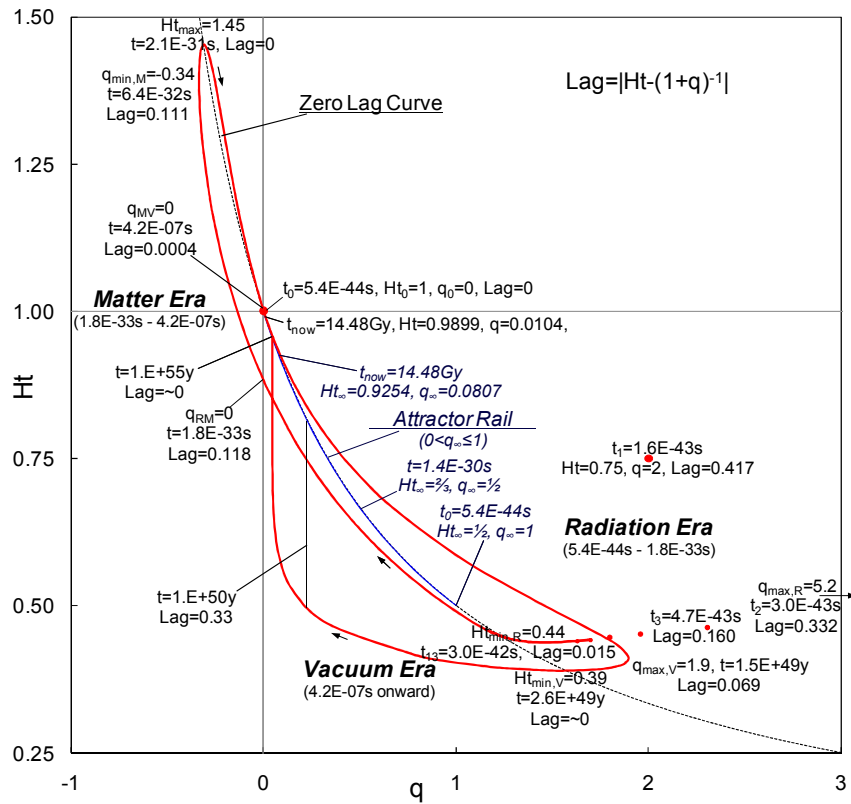


Figure 3. q - Ht phase diagram. q_∞ and Ht_∞ morph into an attractor rail – a line of attractors that q - Ht would gravitate to if ε were constant. The $0 < q_\infty \leq 1$ attractor rail partially overlays the Zero Lag Curve.

2.9 Age of the Universe

The Simon-Verde-Jimenez (SVJ) data points (Simon et al. 2005) were used to establish the age of the Universe (t_{now}). While $t_{\text{now}} = 13.72\text{Gy}$ (Hinshaw et al. 2009) is more widely accepted, $t_{\text{now}} = 14.48\text{Gy}$ is a better fit with the SVJ data points (figure 4). $1/H_{\text{now}} = 14.63\text{Gy}$ (from $t_{\text{now}} = 14.48\text{Gy}$ and $Ht_{\text{now}} = 0.9899$) is within the literature's range of 13.4Gy (Riess et al. 2005) to 15.7Gy (Sandage et al. 2006). As with calculating the age at Decoupling, z was calculated here using $z = R_{\text{now}}/R - 1$.

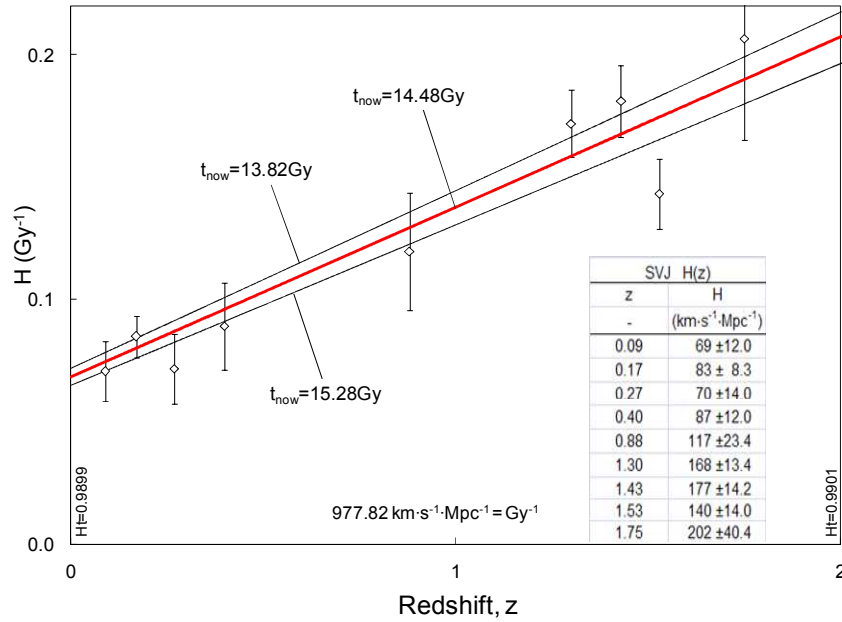


Figure 4. $H(z)$ for high- z radiogalaxy SVJ data points with $\sigma=1$ error bars and curves for t_{now} of 13.82Gy, 14.48Gy, and 15.28Gy. Redshift (z) was calculated for the $H(z)$ curves using $z=R_{\text{now}}/R(t)-1$.

3. Discussions

3.1 No current acceleration

This effort to numerically simulate cosmic expansion began with the belief that any indication of a current accelerated expansion ($q_{\text{now}} < 0$) was in error. The Cosmos was not expanding out of control, and a Big Rip was not forecast. We believed in self-regulating expansion. Not too surprisingly, we found just that. The results of this simulation indicate that $q_{\text{now}} = +0.0104$. If current evidence of a negative q_{now} were to be confirmed, the results of this simulation would be refuted. It is highly doubtful, however, that q_{now} is negative, since the best estimates for H_{now} and t_{now} place $Ht_{\text{now}} = 0.9892$ (Hinshaw et al. 2009). If $\text{Lag}_{\text{now}} < 0.0002$ (as indicated by this simulation), $Ht_{\text{now}} = 0.9892$ would force $q_{\text{now}} > +0.0107$ ($q_{\text{now}} = (Ht_{\text{now}} \pm \text{Lag}_{\text{now}})^{-1} - 1$) and a negative q_{now} would force $Ht_{\text{now}} > 0.9998$ ($Ht_{\text{now}} = (1 + q_{\text{now}})^{-1} \pm \text{Lag}_{\text{now}}$). If, instead, Hinshaw's $Ht_{\text{now}} = 0.9892$ were coupled with $q_{\text{now}} = -0.6$ (Shapiro et al. 2005), Lag ($= |Ht(1+q)^{-1}|$) would be greater than 1.5, which would be indicative of an implausibly wild dynamic that was not seen in this simulation (Lag never exceeded 0.5).

3.2 Zero Lag and observational cosmology

Errors in observational data – especially evident in deriving distances – have been the bane of astronomy since before the time of Hubble. The SVJ data



points (figure 4) demonstrate the significance of the error and how underestimated that error typically is. As seen in section 3.1, $\text{Lag}_{\text{now}} < 0.0002$ can be a valuable aid in rooting out inconsistencies and in determining what the real values are. With $\text{Lag} \approx 0$ in the current epoch ($z=0$ to $z=1091$), $Ht = (1+q)^{-1}$ can be used to good approximation to better refine values for H_{now} , t_{now} , and q_{now} .

3.3 Unexpected findings

Aside from the above-mentioned bias towards a self-regulated expansion, the findings of this paper did not come from prescient expectations or deliberate attempts to address specific issues. The findings came from the computer-generated output of the simulation, where dynamic q and Ht – distinct from theory-connected q_{∞} and Ht_{∞} – emerged. From these findings came answers to some significant questions that confront science today.

3.4 Inflation

Perhaps first amongst these questions concern Inflation. During the simulation's initial development, with an unchanging ϵ , there was no Inflation. Allowing ϵ to increase with time created a dynamic q that turned negative in the Matter Era. Inflation occurred in the Matter Era, and the mechanism for both Inflation and the demise of Inflation was found in an ever-increasing ϵ . Helping to further explain the dynamics of Inflation, a book-balancing deflationary Ht trough and peak q occur in the Vacuum Era. One clear empirical indicator that Inflation did occur is that $Ht_{\text{now}} > 0.93$: without Inflation, Ht_{now} would be less than Ht_{∞} (0.93).

3.5 The inflaton

Particle physics has no place for the inflaton and this simulation has no need for it. Simplicity dictates that the inflaton does not exist.

3.6 Before Planck time

When cosmologists attempt to extrapolate cosmic expansion back to a time before Planck time, they see physics breaking down and singularities developing. Both quantum mechanics (QM) and the results of this simulation would say that there is no time before Planck time. Given our QM-based Ansatz ($R_0 = \text{Planck length}$ and $t_0 = \text{Planck time}$), the simulation's consistency with QM is more input than output.

3.7 Nonfundamental time

As stated earlier, this simulation does not treat time as a fundamental parameter. Like the t_0 consistency with QM discussed above, the nonfundamental nature of time is more input than output. The robustness of the simulation's results without a fundamental time, however, attests to the nonfundamental stature of time.

3.8 Entropy and the arrow of time



The low-to-high direction for both entropy and time would imply a connection. $\Delta t = R/c$ says that the tick of the cosmic clock is proportional to R . Given that R and c are both positive, $\Delta t = R/c$ does not allow for the reversibility of time, and this unidirectional character of time is what we experience as the arrow of time. Entropy, in contrast, while generally having the same unidirectional nature as time, is related to information and thus Γ . The connection between entropy and the arrow of time is thus the connection between Γ and R .

4. Conclusions

Using a content-driven iterative algorithm that had three fundamental parameters and a three-step iterative loop, complexity arose from simplicity. The algorithm generated a forward-progressing, multifaceted representation of cosmic expansion that is concordant with observation and consistent with SR, QM, and GR.

Dynamic q and H_t emerge, a book-balancing payback for Inflation is found late in the Vacuum Era, a causal mechanism is found for the Big Bang and Inflation, and a discrete and self-regulated expansion is seen. The expansion's discreteness resonates with black-hole thermodynamics, string theory, and spin networks. The expansion's emerging complexity and self-regulation hint at self-organization.

With the model's unmatched simplicity, the depth and breadth of findings, and resolution of cosmological issues, the simulation of content-driven expansion supports refinement of the standard model and opens the door for exploring and comparing other cosmic expansion models.

References

- Gimenez, J.C. 2009, *Apeiron* Vol. 16, No. 2
- Hinshaw, G. et al. 2009, *ApJ Supplement Series* 180, 242
- Jones, M.H. et al. 2004, *An Introduction to Galaxies and Cosmology*, p. 298
- Kastl, J.F. 2011 (submitted), *Gravity, Inertia, Cosmic Expansion: A Content-Driven Mechanism*, Gravity Research Foundation
- Perlmutter, S. et al. 1999, *ApJ*, 517, 565
- Perlmutter, S., 2003, *Supernovae, Dark Energy, and the Accelerating Universe*
- Riess, A.G. et al. 1998, *AJ*, 116, 1009
- Riess, A.G. et al. 2005, *ApJ*, 627, 579
- Sandage, A. et al. 2006, *ApJ*, 653, 843
- Shapiro C.A. et al. 2005, *What Do We Know About Cosmic Acceleration?*
- Shu, F.H. 1982, *The Physical Universe: An Introduction to Astronomy*, University Science Books
- Simon, J., Verde, L., Jimenez, R. 2005, *Physics Review D*, 71 123001



Hamilton Equations of General Relativity in Observer's Mathematics

Boris Khots, Dr.Sci.¹ and Dmitriy Khots, Ph.D.²

¹ Compressor Controls Corp, Des Moines, IA, USA
(E-mail: bkhots@cccglobal.com)

² Independent researcher, Omaha, NE, USA
(E-mail: dkhots@cox.net)

Abstract. This work considers the Hamilton equations of general relativity in a setting of arithmetic, algebra, and topology provided by Observer's Mathematics (see [1], [2], [3]). Certain results and communications pertaining to solution of these problems are provided.

Keywords: Hamilton, observer, Lagrange, probability.

1 Introduction

The Hamilton equations are generally written as follows:

$$\dot{p} = -\frac{\partial \mathcal{H}}{\partial q}$$

$$\dot{q} = \frac{\partial \mathcal{H}}{\partial p}$$

In the above equations, the dot denotes the ordinary derivative with respect to time of the functions $p = p(t)$, called generalized momenta, and $q = q(t)$, called generalized coordinates, taking values in some vector space, and $\mathcal{H} = \mathcal{H}(p, q, t)$ is the so-called Hamiltonian, or (scalar valued) Hamiltonian function. Thus, more explicitly, one can equivalently write

$$\frac{d}{dt}p(t) = -\frac{\partial}{\partial q}\mathcal{H}(p(t), q(t), t)$$

$$\frac{d}{dt}q(t) = \frac{\partial}{\partial p}\mathcal{H}(p(t), q(t), t)$$

and specify the domain of values in which the parameter t (time) varies.

2 Basic Physical Interpretation

The simplest interpretation of the Hamilton equations is as follows, applying them to a one-dimensional system consisting of one particle of mass m under time independent boundary conditions: the Hamiltonian \mathcal{H} represents the



energy of the system, which is the sum of kinetic and potential energy, traditionally denoted T and V , respectively. Here q is the x -coordinate and p is the momentum, mv . Then

$$\mathcal{H} = T + V$$

$$T = \frac{p^2}{2m}$$

$$V = V(q) = V(x)$$

Now, the time-derivative of the momentum p equals the Newtonian force, and so here the first Hamilton equation means that the force on the particle equals the rate at which it loses potential energy with respect to changes in x , its location.

The time-derivative of q here means the velocity: the second Hamilton equation here means that the particle's velocity equals the derivative of its kinetic energy with respect to its momentum. (Because the derivative with respect to p of $p^2/2m$ equals $p/m = mv/m = v$.)

3 Using Hamilton's Equations

In terms of the generalized coordinates q and generalized velocities \dot{q} , we can perform the following steps:

1. Write out the Lagrangian $\mathcal{L} = T - V$. Express T and V as though Lagrange's equation were to be used.
2. Calculate the momenta by differentiating the Lagrangian with respect to velocity:

$$p(q, \dot{q}, t) = \frac{\partial \mathcal{L}}{\partial \dot{q}}$$

3. Express the velocities in terms of the momenta by inverting the expressions in step 2.
4. Calculate the Hamiltonian using the usual definition of \mathcal{H} as the Legendre transformation of \mathcal{L} via

$$\mathcal{H} = \dot{q} \frac{\partial \mathcal{L}}{\partial \dot{q}} - \mathcal{L} = \dot{q}p - \mathcal{L}$$

Substitute for the velocities using the results in step (3).

5. Apply Hamilton's equations.

4 Deriving Hamilton's Equations

We can derive Hamilton's equations by looking at how the total differential of the Lagrangian depends on time, generalized positions q and generalized velocities \dot{q} .

$$d\mathcal{L} = \left(\frac{\partial \mathcal{L}}{\partial q} dq + \frac{\partial \mathcal{L}}{\partial \dot{q}} d\dot{q} \right) + \frac{\partial \mathcal{L}}{\partial t} dt$$



Now the generalized momenta were defined as $p = \frac{\partial \mathcal{L}}{\partial \dot{q}}$ and Lagrange's equations tell us that

$$\frac{d}{dt} \frac{\partial \mathcal{L}}{\partial \dot{q}} - \frac{\partial \mathcal{L}}{\partial q} = 0$$

We can rearrange this to get

$$\frac{\partial \mathcal{L}}{\partial q} = \dot{p}$$

and substitute the result into the total differential of the Lagrangian

$$d\mathcal{L} = (\dot{p}dq + p d\dot{q}) + \frac{\partial \mathcal{L}}{\partial t} dt$$

$$d\mathcal{L} = (\dot{p}dq + d(p\dot{q}) - \dot{q}dp) + \frac{\partial \mathcal{L}}{\partial t} dt$$

and rearrange again to get

$$d(p\dot{q} - \mathcal{L}) = (-\dot{p}dq + \dot{q}dp) - \frac{\partial \mathcal{L}}{\partial t} dt$$

The term on the left-hand side is just the Hamiltonian that we have defined before, so we find that

$$d\mathcal{H} = (-\dot{p}dq + \dot{q}dp) - \frac{\partial \mathcal{L}}{\partial t} dt = \left[\frac{\partial \mathcal{H}}{\partial q} dq + \frac{\partial \mathcal{H}}{\partial p} dp \right] + \frac{\partial \mathcal{H}}{\partial t} dt$$

where the second equality holds because of the definition of the total differential of \mathcal{H} in terms of its partial derivatives. Associating terms from both sides of the equation above yields Hamilton's equations

$$\frac{\partial \mathcal{H}}{\partial q} = -\dot{p}, \quad \frac{\partial \mathcal{H}}{\partial p} = \dot{q}, \quad \frac{\partial \mathcal{H}}{\partial t} = -\frac{\partial \mathcal{L}}{\partial t}$$

5 As a Reformulation of Lagrangian Mechanics

Starting with Lagrangian mechanics, the equation of motion is based on generalized coordinates q and matching generalized velocities \dot{q} . We write the Lagrangian as

$$\mathcal{L}(q, \dot{q}, t)$$

with the subscripted variables understood to represent these variables of that type. Hamiltonian mechanics aims to replace the generalized velocity variables with generalized momentum variables, also known as conjugate momenta. By doing so, it is possible to handle certain systems, such as aspects of quantum mechanics, that would otherwise be even more complicated.

For each generalized velocity, there is one corresponding conjugate momentum, defined as:



$$p = \frac{\partial \mathcal{L}}{\partial \dot{q}}$$

The Hamiltonian is the Legendre transform of the Lagrangian:

$$\mathcal{H}(q, p, t) = \dot{q}p - \mathcal{L}(q, \dot{q}, t)$$

If the transformation equations defining the generalized coordinates are independent of t , and the Lagrangian is a product of functions (in the generalized coordinates) which are homogeneous of order 0, 1 or 2, then it can be shown that \mathcal{H} is equal to the total energy $E = T + V$.

Each side in the definition of \mathcal{H} produces differential:

$$d\mathcal{H} = \left[\frac{\partial \mathcal{H}}{\partial q} dq + \frac{\partial \mathcal{H}}{\partial p} dp \right] + \frac{\partial \mathcal{H}}{\partial t} dt = \left[\dot{q} dp + p d\dot{q} - \frac{\partial \mathcal{L}}{\partial q} dq - \frac{\partial \mathcal{L}}{\partial \dot{q}} d\dot{q} \right] - \frac{\partial \mathcal{L}}{\partial t} dt$$

Substituting the previous definition of the conjugate momenta into this equation and matching coefficients, we obtain the equations of motion of Hamiltonian mechanics, known as the canonical equations of Hamilton:

$$\frac{\partial \mathcal{H}}{\partial q} = -\dot{p}, \quad \frac{\partial \mathcal{H}}{\partial p} = \dot{q}, \quad \frac{\partial \mathcal{H}}{\partial t} = -\frac{\partial \mathcal{L}}{\partial t}$$

6 Observer's Mathematics Point of View

The main relation in classical case is

$$(p + \partial p) \times (\dot{q} + \partial \dot{q}) - p \times \dot{q} = p \times \partial \dot{q} + \dot{q} \times \partial p$$

In Observer's Mathematics in W_n (from m -observer point of view with $m > 4n$), the left hand side (LHS) becomes:

$$(p +_n \partial p) \times_n (\dot{q} +_n \partial \dot{q}) -_n p \times_n \dot{q}$$

while the right hand side (RHS) becomes

$$p \times_n \partial \dot{q} +_n \dot{q} \times_n \partial p$$

Crucial difference is that LHS is not always equal to RHS.

Next, we prove the following four theorems.

Theorem 1. *If $p, \dot{q} \in W_2$, from m -observer point of view with $m > 8$, then*

$$P((p +_2 \partial p) \times_2 (\dot{q} +_2 \partial \dot{q}) -_2 p \times_2 \dot{q} = p \times_2 \partial \dot{q} +_2 \dot{q} \times_2 \partial p) = 0.8$$

where P is the probability.



Proof. If we put $\partial p = 0.01$ and $\partial \dot{q} = 0.01$ and take $p = xy.za$ and $\dot{q} = uv.wb$, $x, y, z, u, v, w \in \{0, 1, \dots, 9\}$ with $a \neq 9$, $b \neq 9$, then we have this identity. But if $a = 9$ or $b = 9$, then this identity becomes wrong.

Theorem 2. *If $p, \dot{q} \in W_n$, from m -observer point of view with $m > 4n$, then*

$$P((p +_n \partial p) \times_n (\dot{q} +_n \partial \dot{q}) -_n p \times_n \dot{q} = p \times_n \partial \dot{q} +_n \dot{q} \times_n \partial p) = P_{m,n} < 1$$

Proof. Similar to proof of Theorem 1.

Theorem 3. *If $p, \dot{q} \in W_n$, from m -observer point of view with $m > 4n$, then*

$$\begin{aligned} P(\partial \mathcal{H} = \partial(p \times_n \dot{q} -_n \mathcal{L}(q, \dot{q}, t)) = \\ = \dot{q} \times_n \partial p -_n \frac{\partial \mathcal{L}}{\partial q}(q, \dot{q} +_n \partial \dot{q}, t +_n \partial t) \times_n \partial q -_n \frac{\partial \mathcal{L}}{\partial t}(q, \dot{q} +_n \partial \dot{q}, t) \times_n \partial t) = P_{m,n} < 1 \end{aligned}$$

Proof. Similar to proof of Theorem 1.

Theorem 4. *If $p, \dot{q} \in W_n$, from m -observer point of view with $m > 4n$, then*

$$\begin{aligned} P(\partial \mathcal{H} = \partial(p \times_n \dot{q} -_n \mathcal{L}(q, \dot{q}, t)) = \\ = \dot{q} \times_n \partial p -_n \frac{\partial \mathcal{L}}{\partial q}(q, \dot{q}, t) \times_n \partial q -_n \frac{\partial \mathcal{L}}{\partial t}(q, \dot{q}, t) \times_n \partial t) = P_{m,n,\mathcal{L}} < 1 \end{aligned}$$

Proof. Similar to proof of Theorem 1.

7 Acknowledgements

The authors would like to thank Professor Christos H. Skiadas for his invitation to participate in CHAOS2011.

References

- 1.B. Khots and D. Khots. Mathematics of relativity webbook. url: www.mathrelativity.com, 2004.
- 2.B. Khots and D. Khots. An introduction to mathematics of relativity. *Lecture Notes in Theoretical and Mathematical Physics*, 7:269-306, 2006.
- 3.B. Khots and D. Khots. Physical aspects of observer's mathematics. *American Institute of Physics (AIP)*, 1101:311-313, 2009.





Fluid mixing in finite vortex structures

Korniy Kostkin

Taras Shevchenko National university of Kyiv, Kyiv, Ukraine

E-mail: kornejk@gmail.com

Abstract: Considered two of the vortex structure, each of which consists of lying on a straight line vortices. The first structure consists of three vortices, the second has five. Considered the motion of the structures and fluid mixing under the influence of these structures.

Keywords: Contour tracking, Fluid mixing, Simulation, Vortex.

1. Introduction

The first and simplest example of the motion system of point vortices is a task about motion of two vortices, which is considered the Helmholtz H. in 1902. The first experiments about learning the vortex effects in the liquid were made in 1906. The movable body was usually cylinder. At sufficiently high velocity outside of the cylinder to turn right and the left begun to form vortices. At first they are moved away from the body with some speed that gradually decreases and the distance between the vortices increases slightly. Similar studies performed pockets Karman, Rubah, and other scientists. Considered [2, 4, 6] random motion of infinite linear systems of point vortices. Are given [1] equations of motion of incompressible fluid in the case of planar flow. Investigated [5] motion of vortices in some finite systems.

2. The case of three vortices

Consider a chain consisting of three point vortices, which are from each other at the same distance a and have the same intensity χ . The complex potential outside of the liquid vortex intensity χ , which is at the center point z_0 can be found from the equation:

$$\omega = i \chi \ln(z - z_0).$$

Let our system has this view: the central vortex is located at the origin of coordinates, the other - on both sides of it. The complex potential of the liquid around a system:

$$\omega_3 = i \chi \ln(z) + i \chi \ln(z \pm a) \quad (1)$$

To find the speed of vortices seize the theorem of Kelvin. First, determine the speed of the vortex, located at the origin. Extreme vortex, acting on it to produce



speed $V_0^a = \chi / 2\pi a$ and $V_0^{-a} = -\chi / 2\pi a$, equal in absolute value but opposite in direction. Thus, the total rate of the central vortex is $V_0 = 0$. By Kelvin theorem, speed of each of the other two vortices $V_a = \chi / 2\pi a + \chi / 4\pi a$, but they also have the opposite direction. Thus, the motion of the system can say is: the central vortex will be in rest, and extreme rotate around on a trajectory with a radius of circular a . The speed of their rotation V_a and they will be located on one straight line.

Consider the stability of the system. Content vortex, located at the origin, for some value l of the axis X in the positive direction. His speed under the influence of two other:

$$V_0^1 = \frac{\chi}{2\pi(a-l)} - \frac{\chi}{2\pi(a+l)} = \frac{2\chi l}{2\pi(a^2 - l^2)}.$$

After the shift speed and the whirlwind should move away from the original position. Consider the speed of other vortices. Vortex, located at the point $(a, 0)$ will have speed:

$$V_a^1 = \frac{\chi}{2\pi(a-l)} + \frac{\chi}{4\pi a},$$

Vortex, located at the point $(-a, 0)$:

$$V_{-a}^1 = \frac{\chi}{2\pi(a+l)} + \frac{\chi}{4\pi a}.$$

By rejecting vortex system is not returned in its original position and the vortices become more remote from the original coordinates. Also shown [3] that a deviation from any of the vortices in some coordinates (X, Y) , or with a shift of vortices of a particular law, with increasing time, rejecting also continuously increasing. Therefore, we can say that the set of point vortices in a state of unstable balance. Any deviation of the system will not be returned to its original position, and collapses.

Consider the fluid motion under the influence of such a vortex system. According to the expression for the complex potential (1) can be functions of flow equations for fluid flow created by a system:

$$2i\psi = \omega(z) - \bar{\omega}(\bar{z}). \quad (2)$$

From equation (2) obtain an expression for the family lines of flow:

$$\begin{aligned} \psi = & \frac{\chi}{4\pi} \ln((x - a)^2 + y^2) + \frac{\chi}{4\pi} \ln(x^2 + y^2) + \\ & + \frac{\chi}{4\pi} \ln((x + a)^2 + y^2) - \frac{3\chi}{8\pi} (x^2 + y^2). \end{aligned} \quad (3)$$

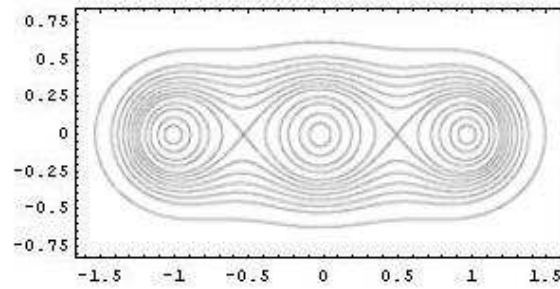


Fig. 1. Instant line of current.

Fig. 1 shows the instantaneous flow of fluid lines in the vicinity of the structure. Apparently, each vortex has its own so-called atmosphere. It's a certain amount of fluid that moves around the vortex for a closed trajectory. We also closed separatrix, are dense in the form of a triple-eights, in which the intersection point of the liquid velocity is zero. Outside the separatrix fluid moves around the entire structure.

The general equation of motion of fluid around the structure can be represented as:

$$\frac{dx}{dt} = \frac{\partial \psi(x, y, t)}{\partial y}, \quad \frac{dy}{dt} = -\frac{\partial \psi(x, y, t)}{\partial x}, \quad (4)$$

Where $\psi(x, y, t)$ - a function of fluid flow defined by the relation (3).

For the numerical simulation of liquid moving was developed algorithm based on the following principles:

- marked trajectories of vortices movement;
- selected initial area of the liquid;
- shown as changed area for moving;
- area selection remains constant;
- the deformation limit of the selection remains inseparable.



Modeling of the liquid under the action of three identical point vortices is presented in Fig. 2.

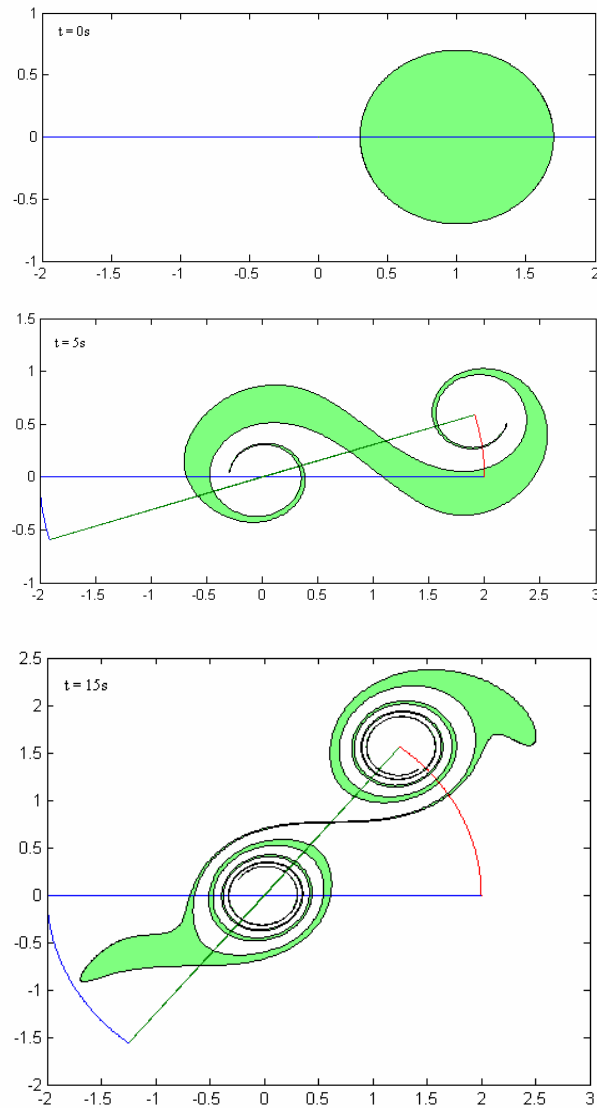


Fig. 2. Mixing at the same intensities of vortices.

The modeling of the situation when the system is fixed. Chain consists of three point vortices, which are from each other at the same distance. Side vortices



have the same intensity 2χ . Central vortex has intensity $-\chi$. The simulation results presented in Fig. 3.

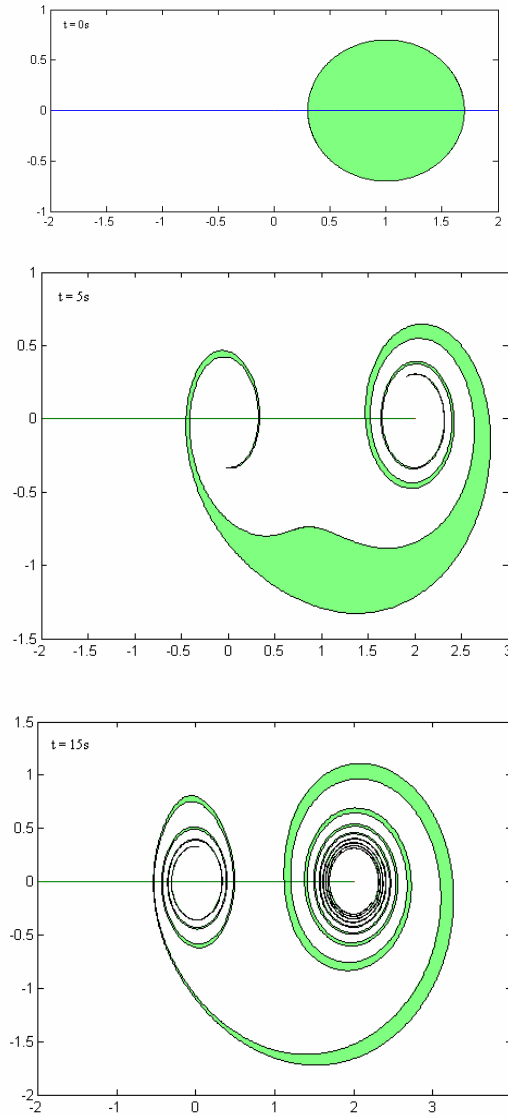


Fig. 3. Mixing in fixed system.

As seen from the simulation, the trajectory of vortex line. Fluid out of the atmosphere vortex will rotate together with the system, and fluid in the atmosphere also revolve around the vortices.



3. The case of the five vortices

Consider a chain consisting of five point vortices, which are from each other at the same distance and have the same intensity. Location systems are the same as in the case of three vortices. The complex potential of the liquid around a system can calculate as:

$$\omega_5 = i\chi \ln(z) + i\chi \ln(z \pm a) + i\chi \ln(z \pm 2a). \quad (5)$$

Consider the speed of the chain. Similarly to the previous case we can show that the central vortex is at rest. Others revolve around it in orbits that resemble the petals in shape. The system is in a state of unstable equilibrium, for any rejection of one or more vortices will not be returned to its original position, but increasingly moving away from him.

Consider the fluid motion under the influence of such a vortex system. Using relation (2) and (5), we obtain equations for fluid flow lines:

$$\begin{aligned} \psi = & \frac{\chi}{4\pi} \ln((x \pm a)^2 + y^2) + \frac{\chi}{4\pi} \ln(x^2 + y^2) + \\ & + \frac{\chi}{4\pi} \ln((x \pm 2a)^2 + y^2) - \frac{25\chi}{96\pi} (x^2 + y^2). \end{aligned} \quad (6)$$

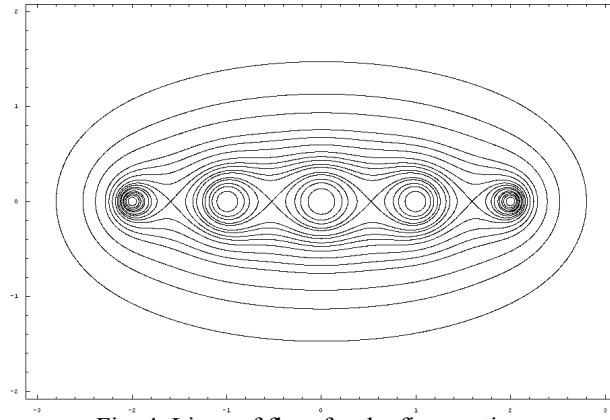


Fig. 4. Lines of flow for the five vortices

Fig. 4 shows a complete picture of instantaneous fluid flow lines around a given vortex. Apparently, each vortex has its own atmosphere. Three central vortices are closed separatrices and the atmosphere. Another closed separatrix, are dense with two outer vortex with three central atmosphere. At all points of crossing separatrices fluid velocity is zero. The general equation of the liquid can be written from equations (4) and (6).



The result of fluid motion is presented in Fig. 5.

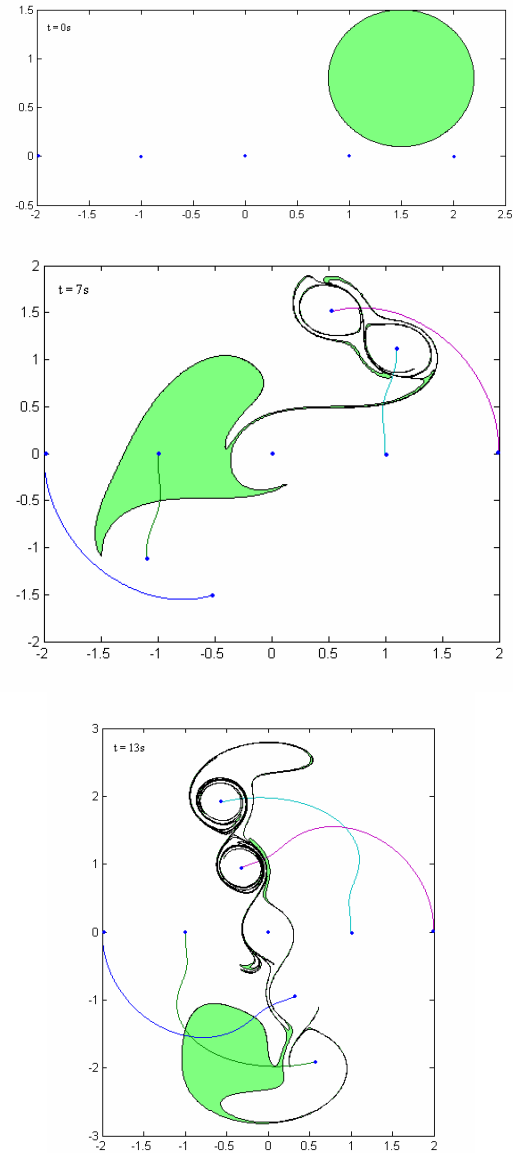


Fig. 5. Mixing in case of the five vortices

As seen from the simulation, the trajectory of nonlinear vortices. Liquid is less by distance from the central vortex to vortex separatrix atmosphere of extreme gift can get their own atmospheres vortices. While the fluid outside this distance will revolve around the system.



3. Conclusions

Considered two finite configurations of vortex chains. Investigated the robustness and the movement of vortices. The equation for determining the complex potential given fluid around the vortex structures and equations of fluid flow lines. Constructed a graphic representation of flow lines of fluid. Computational modeling of fluid mixing vortex structures.

References

1. A. V. Borisov, I. S. Mamaev, and S. M. Ramodanov. Dynamic advection. *Nonlinear Dynamics* 3: 521–530, 2010.
2. H. Villat. *Theory of vortices*, ONTI, Moscow, 1936.
3. K. K. Kostkin. Stability of the vortex chain. *Visnyk Taras Shevchenko National university of Kyiv* 2:57–60, 2010.
4. N. E. Kochin, I. A. Kibel and N. V. Roze. *Theoretical Hydromechanics*, Fizmatgiz, Moscow, 1963.
5. V. V. Meleshko and M. Yu. Konstantinov. *The dynamics of vortex structures*, Naykova dymka, Kyiv, 1993.
6. L. M. Milne – Thomson. *Theoretical Hydromechanics*, Mir, Moscow, 1964.



A sub microscopic description of the formation of crop circles

Volodymyr Krasnoholovets¹ and Ivan Gandzha²

Indra Scientific, Square du Solbosch 26, Brussels, B-1050, Belgium

¹v_kras@yahoo.com, ²gandzha@iop.kiev.ua

Abstract

We describe a sub microscopic mechanism which is responsible for the appearance of crop circles on the surface of the Earth. It is shown that the inner reason for the mechanism is associated with intra-terrestrial processes that occur in the outer core and the mantle of the terrestrial globe. We assume that magnetostriction phenomena should take place at the boundary between the liquid and the solid nickel-iron layers of the terrestrial globe. Our previous studies showed that at the magnetostriction a flow of inertons takes out of the striction material (inertons are carriers of the field of inertia, they represent a substructure of the matter waves, or the particle's psi-wave function; they transfer mass properties of elementary particles and are able to influence massive objects changing their inner state and behaviour). At the macroscopic striction in the interior of the Earth, pulses of inerton fields are irradiated, and through non-homogeneous channels of the globe's mantle and crust they reach the surface of the Earth. Due to the interaction with walls of these channels, fronts of inerton flows come to the surface as fringe images. These inerton flows affect local plants and bend them, which results in the formation of the so-called crop circles. It is argued that the appearance of crop circles under the radiation of inertons has something in common with the mechanism of formation of images in a kaleidoscope, which happens under the illumination of photons.

Key words: crop circles, inertons, mantle and crust channel, magnetostriction of rocks

1. Introduction

Crop circles attract attention of many researchers. Studies (see, e.g. Refs. 1-3) show that in these circles stalks are bent up to ninety degrees without being broken and something softened the plant tissue at the moment of flattening. Something stretches stalks from the inside; sometimes this effect is so powerful that the node looks as exploded from the inside out. In many places crop formation is accompanied with a high degree of magnetic susceptibility, which is caused by adherent coatings of stalks with the commingled iron oxides, hematite (Fe_2O_3) and magnetite (Fe_3O_4) fused into a heterogeneous mass [2].

Researchers [2-4] hypothesized that crop formations involve organised ion plasma vortices, which deliver lower atmosphere energy components of sufficient magnitude to produce bending of stalks, the formation of expulsion cavities in plant stems and significant changes in seedling development. It should be noted that an idea of the origin of crop circles associated with the atmosphere energy and/or UFO is wildly accepted.



On the other hand, researchers who study geophysical processes and the earthquakes note about possible regional semi-global magnetic fields that might be generated by vortex-like cells of thermal-magmatic energy, rising and falling in the earth's mantle [5]. Another important factor is magnetostriction of the crust – the alteration of the direction of magnetization of rocks by directed stress [6,7].

Moreover, recent study [8] has suggested a possible mechanism of earthquake triggering due to magnetostriction of rocks in the crust. The phenomenon of magnetostriction in geophysics is stipulated by mechanical deformations of magnetic minerals accompanied by changes of their remanent or induced magnetization. These deformations are specified by magnetostriction constants, which are proportional coefficients between magnetization changes and mechanical deformations. A real value of the magnetostriction constant of the crust is estimated as about 10^{-5} ppm/nT, which is a little larger than for pure iron. Yamazaki's calculation [8] shows that effects connected to the magnetostriction of rocks in the crust can produce forces nearly 100 Pa/year and even these comparatively small stress changes can trigger earthquakes.

Of course, weaker deformations associated with magnetostriction of rocks also take place. These are the magnetostriction deformations that we put in the foundation of the present study of field circles.

2. Preliminary

Our theoretical and experimental studies have shown that the phenomenon of magnetostriction is accompanied with the emission of inerton fields from the magnetostrictive material studied. What is the inerton field?

Bounias and one of the authors [9-12] proposed a detailed mathematical theory of the constitution of the real physical space. In line with this theory, real space is constrained to be a mathematical lattice of closely packed topological balls with approximately the Planck size, $\sqrt{\hbar G/c^3} \sim 10^{-35}$ m. It was proven that such a lattice is a fractal lattice and that it also manifests tessellation properties. It has been called a *tessel-lattice*. In the tessell-lattice volumetric fractalities of cells are associated with the physical concept of mass. A particle represents a volumetrically deformed cell of the tessell-lattice. The motion of such a particle generates elementary excitations of the tessell-lattice around the particle. These excitations, which move as a cloud around the particle, represent the particle's force of inertia. That is why they were called *inertons* [13,14]. The corresponding submicroscopic mechanics developed in the real space can easily be connected to conventional orthodox quantum mechanics constructed in an abstract phase space. Submicroscopic mechanics associates the particle's cloud of inertons with the quantum mechanical wave ψ -function of this particle. Thus, the developing concept turns back a physical sense to the wave ψ -function: this function represents the field of inertia of the particle under consideration. Carriers of the field of inertia are inertons. A free inerton, which is released from the particle's cloud of inertons, possess a velocity that exceeds the velocity of light c [15].

In condensed media entities vibrating at the equilibrium positions periodically irradiate and absorb their clouds of inertons back [16]; owing to such a behaviour the mass of entities varies. This means that under special conditions the matter may irradiate a portion of its inertons. Lost inertons then can be absorbed by the other system, which has to result in changes of physical properties of the system.

One of such experiments was carried out in work [17]. Continuous-wave laser illumination of ferroelectric crystal of LiNbO_3 resulted in the production of a long-living stable electron droplet with a size of about 100 μm , which freely moved with a velocity of



about 0.5 cm/s in the air near the surface of the crystal experiencing the Earth's gravitational field. The role of the restraining force of electrons in the droplet was attributed to the inerton field, a substructure of the particles' matter waves, which was expelled from the surface of crystal of LiNbO_3 together with photoelectrons by a laser beam. Properties of electrons after absorption of inertons changed very remarkably – they became heavy electrons whose mass at least million of times exceeded the rest mass of free electrons. Only those heavy electrons could elastically withstand their Coulomb repulsion associated with the electrical charge, which, of course, is impossible in the case of free electrons.

We have shown [16] that in the chemical industry inerton fields are able to play the role of a field catalyst or, in other words, inerton fields can serve to control the speed of chemical reactions. In the reactive chamber we generated inerton fields by using magnetostriction agents: owing to the striction the agents non-adiabatically contract, which is culminated in the irradiation of sub matter, i.e. inertons, from the agents. Then under the inerton radiation, the formation of a new chemical occurred in several seconds, though usually these chemical reactions last hours.

Therefore, these results allow us to involve inerton fields, which originate from the ground, in a study of the formation of crop circles.

The thickness of the crust is about 20 km. The mantle extends to a depth above 3000 km. The mantle is made of a thick solid rocky substance. Due to dynamical processes in the interior of the Earth, magnetostrictive rocks contract with a coefficient of about 10^{-5} [8], which is a trigger mechanism for the appearance of a flow of inerton radiation. This flow of inertons shoots up from a depth by coming through the mantle and crust channel. Such channels are usual terrestrial materials with some non-homogenous inclusions down to tens or hundreds of kilometres from the surface of the terrestrial globe (compare with bio-energy channels in our body: the crude morphological structure is the same, but the fine morphological structure is different, which allows these bio-energy channels to display a higher conductivity).

A mantle-crust channel can be modelled as a cylindrical tube, which has a cross-section area equal to A , along which a flow of inertons travels out from the interior of the globe. The inner surface of the channel has to reflect inerton radiation, at least partly, so that the flow of inertons will continue to follow along the channel to its output, i.e. the surface of the Earth.

3. Elastic rod bending model

Let us evaluate conditions under which the stalks of herbaceous plants will bend affected by mantle inertons.

A stalk of a plant can be modelled for the first approximation by an elastic rod (Fig. 1). We suppose that it is deformed by an external force f distributed uniformly over the rod length l . This external force is a force caused by a flow of inertons going from the ground due to a weak collision of the mantle and crust rocks as described above. The rod profile in the projections to the horizontal and vertical axes is described as follows [18].

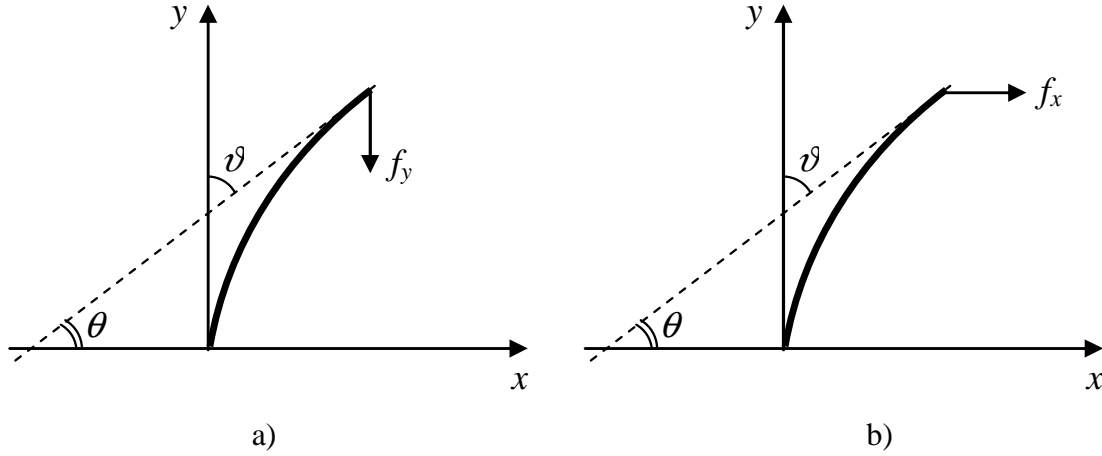


Figure 1. Elastic rod model.

I. Vertical force f_y (Fig. 1a)

$$x = \sqrt{\frac{2IE}{f_y}} (\sqrt{1 - \cos \vartheta_l} - \sqrt{\cos \vartheta - \cos \vartheta_l}), \quad (1)$$

$$y = \sqrt{\frac{IE}{2f_y}} \int_0^{\vartheta} \frac{\cos \vartheta d\vartheta}{\sqrt{\cos \vartheta - \cos \vartheta_l}}. \quad (2)$$

Here $I = \pi R^4 / 4$ is the rod's moment of inertia, R is the rod's radius, and E is the Young's modulus of the rod's material. The length of the rod is explicitly given as

$$l = \sqrt{\frac{IE}{2f_y}} \int_0^{\vartheta} \frac{d\vartheta}{\sqrt{\cos \vartheta - \cos \vartheta_l}}. \quad (3)$$

At the maximum bending we have $\vartheta_{\max} = \vartheta_l = \pi/2$, so that

$$l = \sqrt{\frac{IE}{2f_y}} \int_0^{\pi/2} \frac{d\vartheta}{\sqrt{\cos \vartheta}} = \sqrt{\frac{IE}{f_y}} K(1/2), \quad (4)$$

where $K(1/2) \approx 1.854$ is the complete elliptic integral of the first kind. Hence, we come to an expression for the force required to bend the rod by a $\pi/2$ angle:

$$f_y = \frac{IE}{l^2} K^2(1/2) \approx 3.44 \frac{IE}{l^2}. \quad (5)$$

II. Horizontal force f_x (Fig. 1b)

$$x = \sqrt{\frac{IE}{2f_x}} \int_0^{\vartheta} \frac{\sin \vartheta d\vartheta}{\sqrt{\sin \vartheta_l - \sin \vartheta}}, \quad (6)$$

$$y = \sqrt{\frac{2IE}{f_x}} (\sqrt{\sin \vartheta_l} - \sqrt{\sin \vartheta_l - \sin \vartheta}). \quad (7)$$



The length of the rod is explicitly given as

$$l = \sqrt{\frac{IE}{2f_x}} \int_0^{\vartheta_l} \frac{d\vartheta}{\sqrt{\sin \vartheta_l - \sin \vartheta}}. \quad (8)$$

In this case the maximum bending angle should be smaller than $\pi/2$ (no such a force exists that can bend the rod by this angle). So, we select the maximum bending angle at $\vartheta_l = \pi/3$ and write the corresponding relationship between the rod's length and the acting force:

$$l \approx \sqrt{\frac{IE}{2f_x}} 2.61 \text{ or } f_x \approx 3.41 \frac{IE}{l^2}, \quad (9)$$

which is nearly the same as in the previous case (5).

Now let us evaluate the value of the breaking force $f = f_x \cong f_y$. We have to substitute numerical values $l = 0.5$ m, $R = 1.5 \times 10^{-3}$ m for the rod and the value of elasticity (Young's) modulus E to expressions (5) or (9). The value of E has been measured for many different grasses, see, e.g., Refs. 19-23. According to these data, E varies approximately from 0.8 to about 10^9 kg/(m·s²). For instance, in the case of wheat we can take $E \approx 3 \times 10^9$ kg/(m·s²), which gives $f \approx 0.16$ N.

Besides, the authors [19-23] emphasize that for grassy stalks in addition to the elasticity modulus one has to take into account the bending stress, the yield strength (tensile strength) and the shearing stress. These parameters range from 7×10^6 to about 50×10^6 kg/(m·s²) and, hence, significantly decrease the real value of f , which is capable to bend stalks. For example, putting for E the value of the maximal tensile stress 50×10^6 kg/(m·s²) we derive for the bending force $f \approx 0.0027$ N.

The gravity force acting on the rod is

$$f_g = mg = \rho Vg = \pi \rho R^2 l g \approx 0.033 \text{ N} \quad (10)$$

where ρ is the rod's material density about $\rho = 10^3$ kg/m³, m and V are its mass and volume, and $g = 9.8$ m/s² is the acceleration due to gravity.

Comparing the gravity force f_g with the banding force f we may conclude that the latter is not enough to fracture a grassy stalk. Only the breaking forces (5) and (9) can exceeds the gravity force (10).

4. Motion in the rotating central field

The inner surface of a mantle-crust channel can be described by a retaining potential U , which is holding a flow of inertons spreading along the channel from an underground source. Let μ be the mass of an effective batch of terrestrial inertons from this source, which interact with a grassy stalk. The planar motion of such a batch of inertons in the central field is described by the Lagrangian

$$L = \frac{\mu}{2} (\dot{r}^2 + r^2 \dot{\varphi}^2) - U(r, \varphi), \quad (11)$$



which is here written in polar coordinates r and φ ; dot standing for the derivative with respect to time. To model a spreading inerton field, the potential should include a dependence on the angular velocity, $U(r, \dot{\varphi})$, which means that we involve the proper rotation of the Earth relative to the flow of inertons. For instance, the potential can be chosen in the form of the sum of two potentials:

$$U(r, \dot{\varphi}) = \frac{\alpha}{2} r^2 + \frac{\beta}{2} r^2 \dot{\varphi}. \quad (12)$$

In the right hand side of expression (12) the first term is a typical central-force harmonic potential, which describes an elastic behaviour of the batch of inertons in the channel and the surrounding space; the second term includes a dependence on the azimuthal velocity, which means that it depicts the rotation-field potential. The introduction of this potential allows us to simulate more correctly the reflection of inertons from the walls of the mantle channel, which of course only conditionally can be considered round in cross-section.

The equations of motion are then written as

$$\frac{d}{dt} \frac{\partial L}{\partial \dot{q}_i} - \frac{\partial L}{\partial q_i} = 0, \quad i = 1, 2, \quad q_1 \equiv \rho, \quad q_2 \equiv \varphi, \quad (13)$$

or in the explicit form

$$\ddot{r} - r\dot{\varphi}^2 + \frac{\alpha}{\mu} r + \frac{\beta}{\mu} r\dot{\varphi} = 0, \quad (14)$$

$$r\ddot{\varphi} + 2\dot{r}\left(\dot{\varphi} - \frac{\beta}{2\mu}\right) = 0. \quad (15)$$

These equations can be integrated explicitly or solved numerically at the given initial conditions $r(0)$, $\dot{r}(0)$, $\varphi(0)$, $\dot{\varphi}(0)$, and the trajectory of motion can be plotted in rectangular coordinates $\{r \cos \varphi, r \sin \varphi\}$. The second equation represents the conservation of the angular momentum M :

$$\frac{d}{dt} \left[\mu r^2 \left(\dot{\varphi} - \frac{\beta}{2\mu} \right) \right] = 0 \quad \text{or} \quad M = \mu r^2 \left(\dot{\varphi} - \frac{\beta}{2\mu} \right) = \text{const}. \quad (16)$$

Figures 2 and 5 show two possible trajectories at particular values of the parameters.

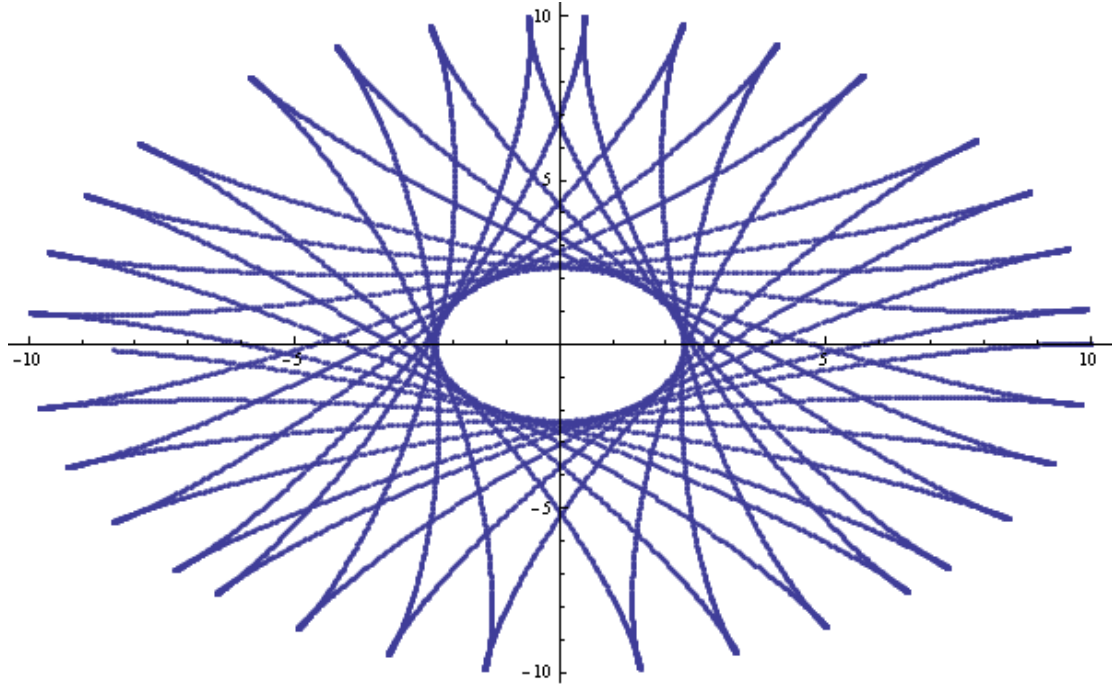


Figure 2. Trajectory of the motion of intertons in the rotating central field with parameters $\alpha/\mu=1 \text{ s}^{-2}$, $\beta/\mu=0.5 \text{ s}^{-1}$; $r(0)=10 \text{ m}$, $\dot{r}(0)=0$, $\varphi(0)=0$, $\dot{\varphi}(0)=0.01 \text{ s}^{-1}$.

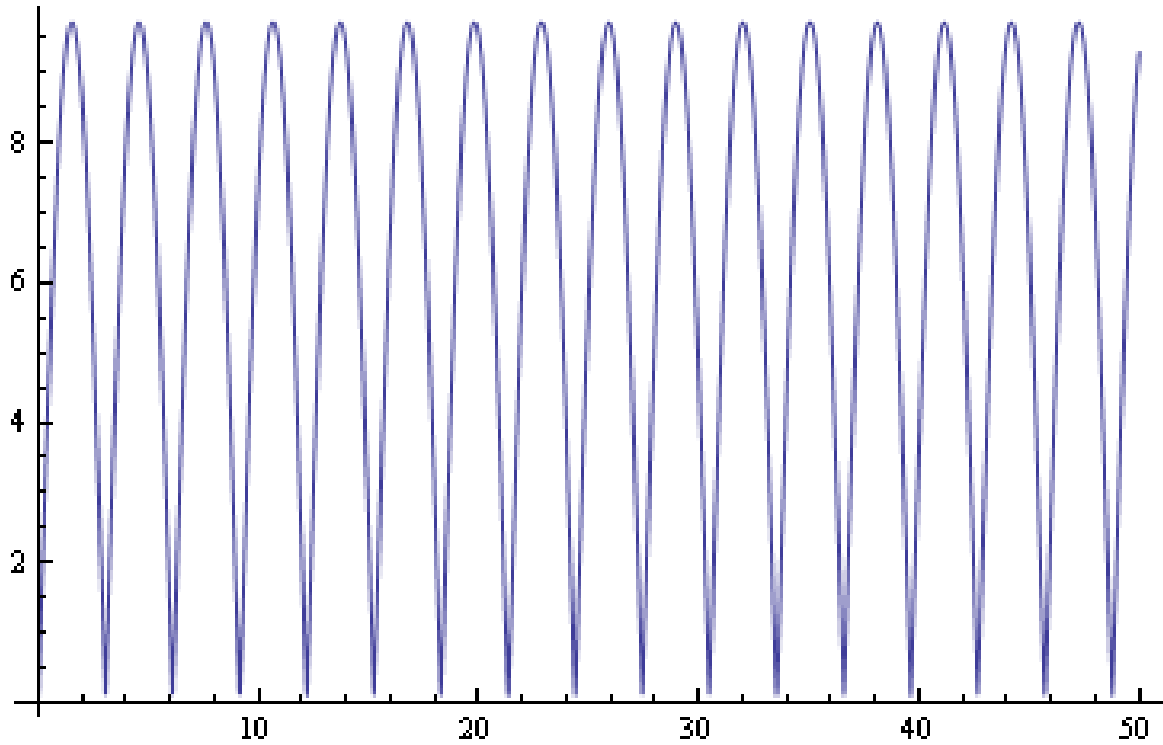


Figure 3. Velocity $|\dot{\vec{r}}| = \sqrt{\dot{r}^2 + r^2\dot{\varphi}^2}$ of the batch of intertons versus time for the case of the trajectory shown in Fig. 2. The maximal velocity is $v_{\max} = 10 \text{ m/s}$.

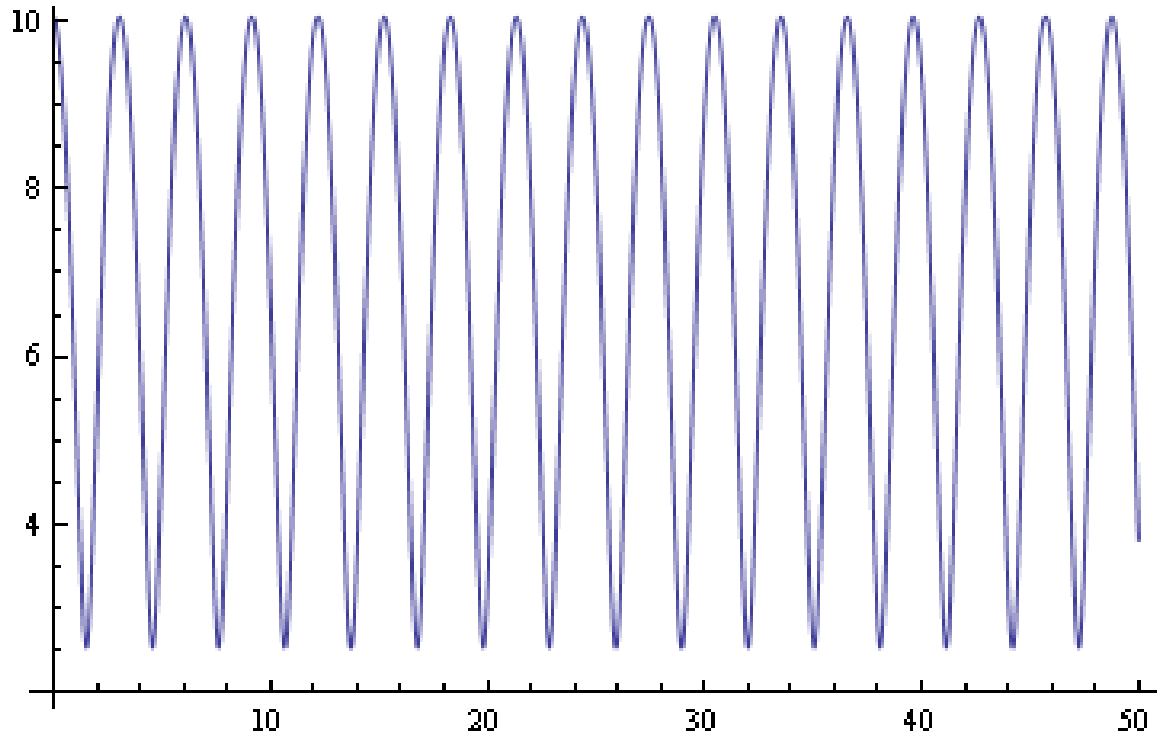


Figure 4. Acceleration $|\ddot{\vec{r}}| = \sqrt{(\ddot{r} - r\dot{\varphi}^2)^2 + (2\dot{r}\dot{\varphi} + r\ddot{\varphi})^2}$ of the batch of inertons versus time for the case of the trajectory shown in Fig. 2. The maximal acceleration is $a_{\max} \approx 10 \text{ m/s}^2$.

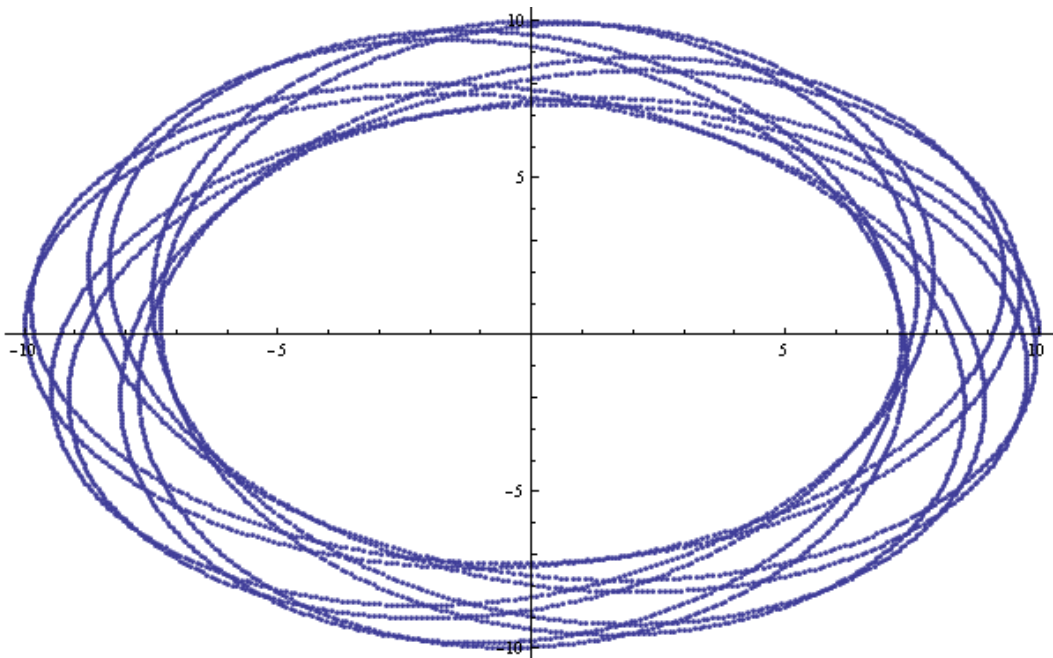


Figure 5. Trajectory of the motion of inertons in the rotating central field with parameters $\alpha/\mu = 1 \text{ s}^{-2}$, $\beta/\mu = 0.5 \text{ s}^{-1}$; $r(0) = 10 \text{ m}$, $\dot{r}(0) = 0$, $\varphi(0) = 0$, $\dot{\varphi}(0) = 1 \text{ s}^{-1}$.

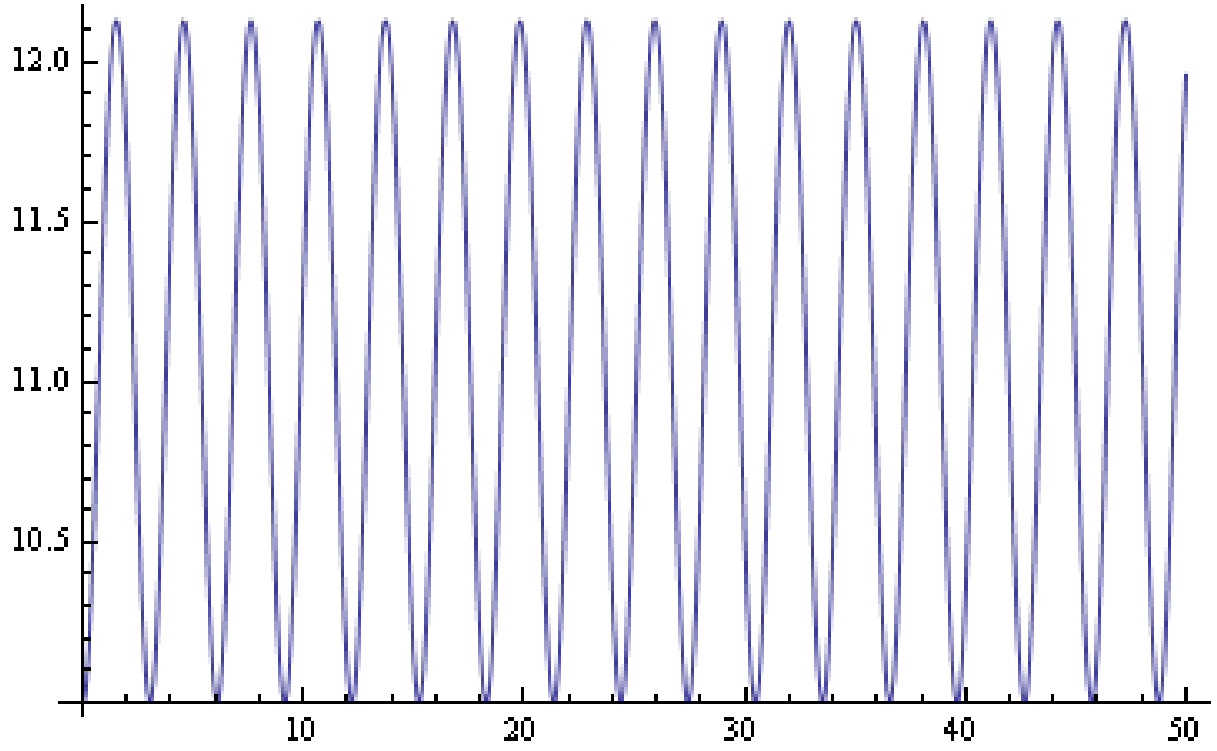


Figure 6. Velocity $|\dot{\vec{r}}| = \sqrt{\dot{r}^2 + r^2 \dot{\phi}^2}$ of the batch of inertons versus time for the case of the trajectory shown in Fig. 5. The maximal velocity is $v_{\max} \approx 12$ m/s.

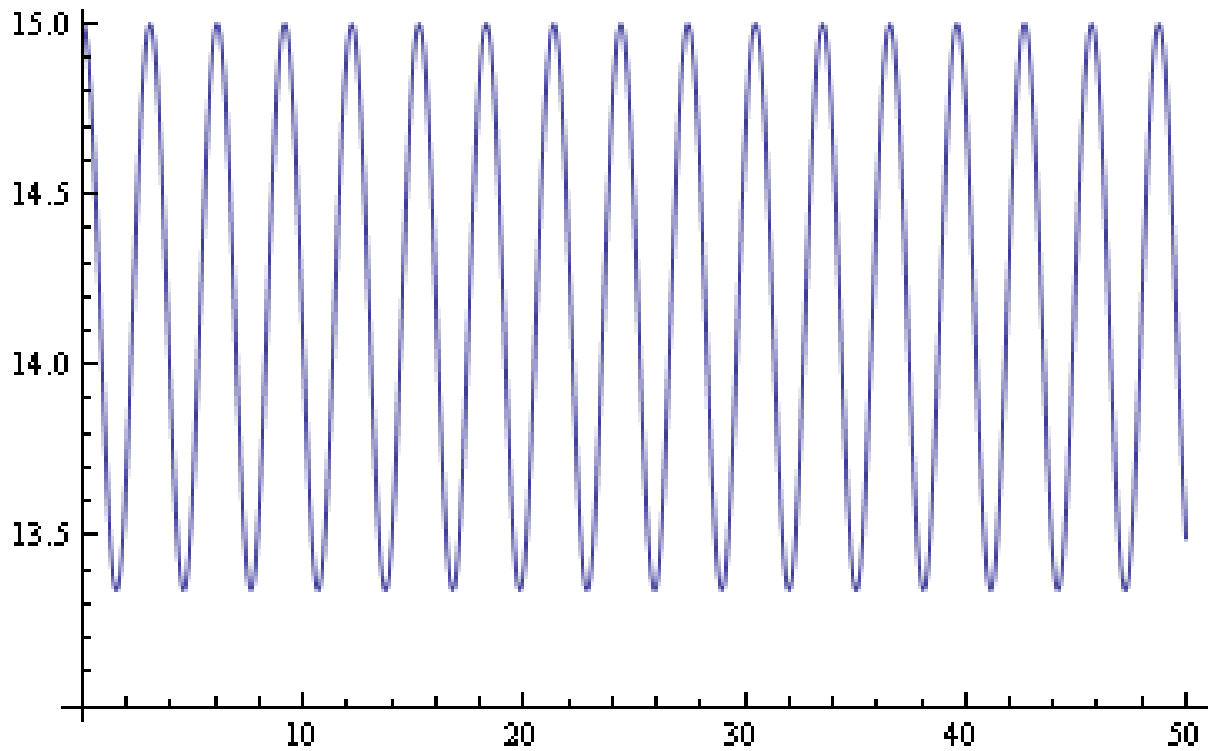


Figure 7. Acceleration $|\ddot{\vec{r}}| = \sqrt{(\ddot{r} - r\dot{\phi}^2)^2 + (2\dot{r}\dot{\phi} + r\ddot{\phi})^2}$ of the batch of inertons versus time for the case of the trajectory shown in Fig. 5. The maximal acceleration is $a_{\max} \approx 15$ m/s².

In the case of the Newton-type potential, expression (12) changes to

$$U(r, \dot{\varphi}) = -\frac{\gamma}{r} + \frac{\beta}{2} r^2 \dot{\varphi}. \quad (17)$$

Then the equations of motion for the Lagrangian (11) become

$$\ddot{r} - r\dot{\varphi}^2 + \frac{\gamma}{\mu r^2} + \frac{\beta}{\mu} r\dot{\varphi} = 0, \quad (18)$$

$$r\ddot{\varphi} + 2\dot{r}\left(\dot{\varphi} - \frac{\beta}{2\mu}\right) = 0 \quad (19)$$

The solution to these equations is shown in Fig. 8.

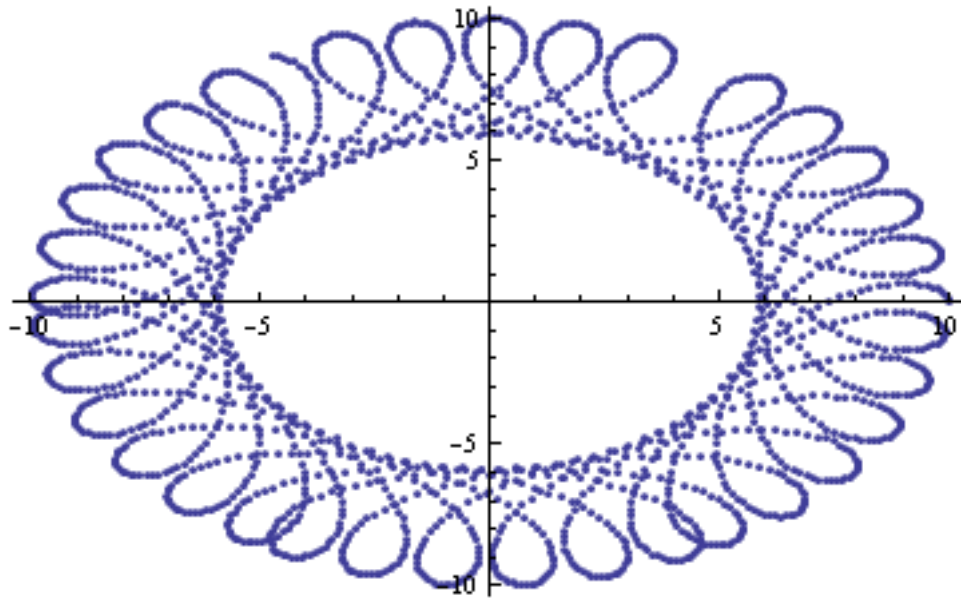


Figure 8. Trajectory of the motion of inertons in the rotating central field with parameters $\gamma/\mu = 1 \text{ m}^3 \text{ s}^{-2}$, $\beta/\mu = 0.1 \text{ s}^{-1}$; $r(0) = 10 \text{ m}$, $\dot{r}(0) = 0$, $\varphi(0) = 0$, $\dot{\varphi}(0) = 0.01 \text{ s}^{-1}$.

In Fig. 9 we show the solution to the equations of motion of a batch of inertons for the case of simplified potential (17), namely, when it is represented only by the Newton-type potential $U(r) = -\gamma/r$.

Figures 4 and 7 give an estimate for the acceleration a of the batch of inertons: $a = 10$ to 15 m/s^2 .

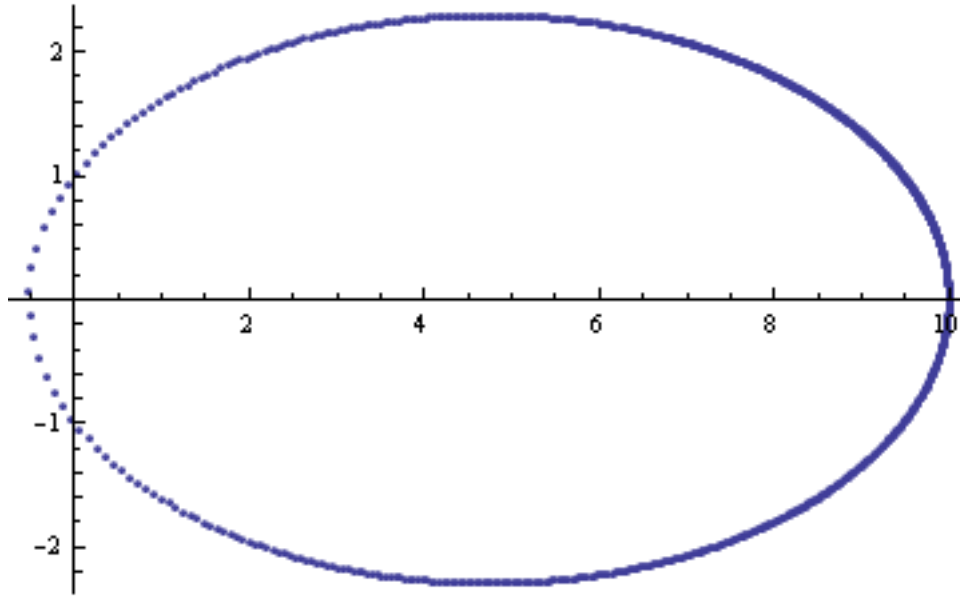


Figure 9. Elliptic trajectory of the motion of inertons in the Newton-type potential with parameters $\gamma/\mu = 1 \text{ m}^3 \cdot \text{s}^{-2}$, $\beta/\mu = 0 \text{ s}^{-1}$; $r(0) = 10 \text{ m}$, $\dot{r}(0) = 0$, $\varphi(0) = 0$, $\dot{\varphi}(0) = 0.01 \text{ s}^{-1}$.

Figures 2, 4, 8 and 9 depict possible patterns of crop circles generated by flows of the mantle-crust inertons.

Let us estimate now the intensity of inerton radiation needed to form a crop circle of total area $A \approx 100 \text{ m}^2$. Let M_{rocks} be the mass of the mantle-crust rocks that generate inertons owing to their magnetostriiction activity. We have to take into account the magnetostriiction coefficient C , which describes an extension strain of rocks. In view of the fact of that low frequencies should accompany geophysical dynamical processes, we can assume that the striction activity of a local group of rocks occurs at a low frequency ν (i.e. rocks collide N times per a time Δt of radiation of inertons). Having these parameters, we can evaluate a flow of mass μ_{Σ} that is shot in the form of inerton radiation at the striction of rocks: $\mu_{\Sigma} \approx NCM_{\text{rocks}}$.

If we put $M \sim 10^7 \text{ kg}$, $C \sim 10^{-5}$, and $N = 5$ we obtain $\mu_{\Sigma} \approx 500 \text{ kg}$. This mass μ_{Σ} is distributed along the area of A in the form of a flow of the inerton field. Let each square metre be the ground for the growth of 1000 stalks. Then 10^5 stalks can grow in the area of $A = 100 \text{ m}^2$. This means that each stalk is able to catch an additional mass $\mu = \mu_{\Sigma}/10^5 = 5 \text{ g}$ from the underground inerton flow; this value is of the order of the mass of a stalk itself.

Knowing the mass $\mu = 5 \times 10^{-3} \text{ kg}$ of the batch of inertons which interacts with a stalk and the acceleration of this inerton batch $a = 10$ to 15 m/s^2 , we can rate the force of inertons that bends and breaks up stalks in the large area A : $F \approx 0.05$ to 0.075 N . This estimation exceeds not only the threshold bending force f , but also the gravity force f_g (10) evaluated in section 3. Therefore, the model developed in this work is plausible.

5. Kaleidoscope model

This kaleidoscope model gives a static description of inerton structures. We assume that a bunch of inertons depicted in the centre of Fig. 10 is reflected from the walls, whose geometry was selected rectangular in this particular example. Multiple reflections from the walls produce the pattern shown in Fig. 10. This model can be assumed as an analogy of geometrical optics with light reflecting from the mirrors. Uniting the rotating central field model described in the previous section and the kaleidoscope model can generate yet more complex patterns.

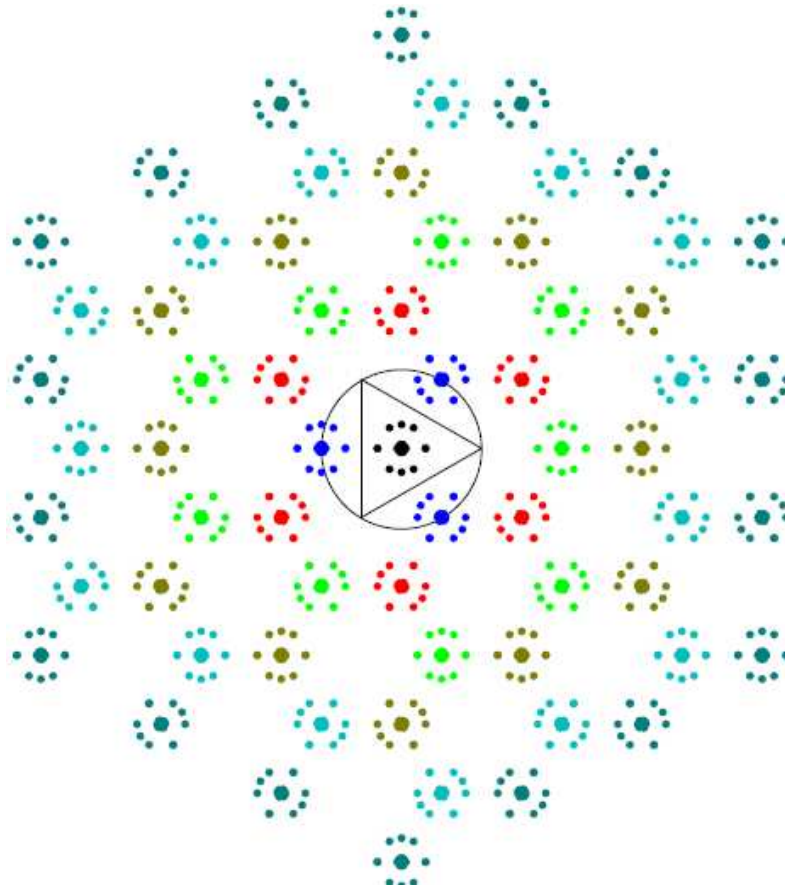


Figure 10. Kaleidoscope model

6. Conclusion

In this study we have shown a radically new approach to the conception and description of crop circles. The theory developed is multi-aspect and based on first submicroscopic principles of fundamental physics. The theory sheds light also on fine processes occurring in the crust and the mantle of the terrestrial globe.

The investigation will allow following researchers to improve the mathematical model of the description of shapes of crop circles, to correctly concentrate on biological changes in plants taken from crop circles, to reach more progress in understanding a subtle dynamics of the earth crust, and to contemplate a more delicate approach to the development of new methods of earthquake prediction.



References

- [1] W. C. Levensgood, Anatomical anomalies in crop formation plants, *Physiologia Plantarum* **92**, 356-363 (1994).
- [2] W. C. Levensgood and J. Bruke, Semi-Molten Meteoric Iron Associated with a Crop Formation, *J. Scient. Exploration* **9**, No. 2, pp. 191-199 (1995).
- [3] J. A. Bruke, The physics of crop formations, *MUFON Journal*, October, pp. 3-7 (1998).
- [4] W. C. Levensgood and N. P. Talbott, Dispersion of energies in worldwide crop formations, *Physiologia Plantarum* **105**, 615-624 (1999).
- [5] J.-C. Pratsch, Relative motion in geology: some philosophical differences, *J. Petroleum Geology* **13**, No. 2, 229-234 (1990).
- [6] W. H. Munk and G. J. F. Macdonald, *The Rotation of the Earth. A Geophysical Discussion* (Cambridge University Press, London, 1975).
- [7] H. Jeffreys, *The earth. Its origin, history and physical constitution* (Cambridge University Press, London, 1976).
- [8] K. Yamazaki, Possible mechanism of earthquake triggering due to magnetostriction of rocks in the crust, *American Geophysical Union, Fall Meeting 2007*, abstract #S33B-1307, Dec. 2007.
- [9] M. Bounias and V. Krasnoholovets, Scanning the structure of ill-known spaces: Part 1. Founding principles about mathematical constitution of space, *Kybernetes: The Int. J. Systems and Cybernetics* **32**, Nos. 7/8, 945-975 (2003); arXiv.org: physics/0211096.
- [10] M. Bounias and V. Krasnoholovets, Scanning the structure of ill-known spaces: Part 2. Principles of construction of physical space, *ibid.* **32**, Nos. 7/8, 976-1004 (2003); arXiv: physics/0212004.
- [11] M. Bounias and V. Krasnoholovets, Scanning the structure of ill-known spaces: Part 3. Distribution of topological structures at elementary and cosmic scales, *ibid.* **32**, Nos. 7/8, 1005-1020 (2003); arXiv: physics/0301049.
- [12] M. Bounias and V. Krasnoholovets, The universe from nothing: A mathematical lattice of empty sets. *Int. J. Anticipatory Computing Systems* **16**, 3-24 (2004); arXiv.org: physics/0309102
- [13] V. Krasnoholovets, Submicroscopic deterministic quantum mechanics, *Int. J. Computing Anticipatory Systems* **11**, 164-179 (2002); arXiv: quant-ph/0109012.
- [14] V. Krasnoholovets, Inerton fields: Very new ideas on fundamental physics, *American Inst. Phys. Conf. Proc.* – Dec. 22, 2010 - Volume **1316**, pp. 244-268. Search for fundamental theory: The VII International Symposium Honoring French Mathematical Physicist Jean-Pierre Vigi r (12-14 July 2010, Imperial College, London); doi:10.1063/1.3536437.
- [15] V. Krasnoholovets and J.-L. Tane, An extended interpretation of the thermodynamic theory including an additional energy associated with a decrease in mass, *Int. J. Simulation and Process Modelling* **2**, Nos. 1/2, 67-79 (2006); also arXiv.org: physics/0605094.
- [16] V. Krasnoholovets, Variation in mass of entities in condensed media, *App. Phys. Research* **2**, No. 1, 46-59 (2010).
- [17] V. Krasnoholovets, N. Kukhtarev and T. Kukhtareva, Heavy electrons: Electron droplets generated by photogalvanic and pyroelectric effects. *Int. J. Modern Phys. B* **20**, No. 16, 2323-2337 (2006); arXiv.org: 0911.2361[quant-ph].
- [18] L. D. Landau and E. M. Lifshits, *The theory of elasticity* (Nauka, Moscow, 1987), pp. 106-107 (in Russian).



- [19] G. Skubisz, The dependence of the Young's modulus of winter wheat stalk in various phenological phases, *Proceedings of the 2nd International Conference on physical properties of agricultural materials*, Godollo, Hungary, 26-28 August 1980, Vol. 2. (1980), p. 9.
- [20] G. H. Dunn and S. M. Dabney, Modulus of elasticity and moment of inertia of grass hedge stems, *Transactions of the ASAE* **39**, No. 3, 947-952 (1996).
- [21] M. Nazari Galedar, A. Jafari, S. S. Mohtasebi, A. Tabatabaeefar, A. Sharifi, M. J. O'Dogherty, S. Rafiee and G. Richard, Effects of moisture content and level in the crop on the engineering properties of alfalfa stems, *Biosystems Engineering* **101**, No. 2, 199-208 (2008).
- [22] H. Tavakoli, S.S. Mohtasebi, A. Jafari, Effects of moisture content, internode position and loading rate on the bending characteristics of barley straw, *Research in Agricultural Engineering* **55**, No. 2, 45-51 (2009).
- [23] A. Esehaghbeygi, B. Hoseinzadeh, M. Khazaei and A. Masoumi, Bending and shearing properties of wheat stem of alvand variety, *World Applied Sciences J.* **6**, No. 8, 1028-1032 (2009).



Studying the Non-Linearity of Tumour Cell Populations under Chemotherapeutic Drug Influence¹

George I. Lambrou, Apostolos Zaravinos, Maria Adamaki and Spiros Vlahopoulos

^{1st} Department of Pediatrics, University of Athens, Choremeio Research Laboratory, Athens, Greece
E-mail: glamprou@med.uoa.gr

Abstract: Biological systems are characterized by their potential for dynamic adaptation. Such systems, whose properties depend on their initial conditions and response over time, are expected to manifest non-linear behaviour. In a previous work we examined the oscillatory pattern exhibited by leukemic cells under *in vitro* growth conditions, where the system was simulating the dynamics of growth with disease progression. Our question in the previous study evolved around the nature of the dynamics of a cell population that grows, or even struggles to grow, under treatment with chemotherapeutic agents. We mentioned several tools that could become useful in answering that question, as for example the *in vitro* models which provide information over the spatio-temporal nature of such dynamics, but *in vivo* models could prove useful too.

In the present work we have studied the non-linear effects that arise from cell population dynamics during chemotherapy. The study was performed not only in the sense of cell populations *per se* but also as an attempt of identifying sub-populations of cells, such as apoptotic cells and cells distributed within the cell cycle. The temporal transition from one state to the next was revealed to follow non-linear dynamics. We have managed to approximate the non-linear factor that influences these temporal space transitions. To the best of our knowledge there are not many studies dealing with this topic, which makes it even more interesting. Such approaches could become very useful in understanding the nature of cell proliferation and the role that certain chemotherapeutic drugs play in cell growth, with emphasis given on the underlying drug resistance and cell differentiation mechanisms.

Keywords: Proliferation, oscillations, non-linearity, CCRF-CEM, glucocorticoids.

1. Introduction

Population dynamics have been the subject of study of various groups. It has already been shown that even cells growing under normal conditions can manifest proliferation dynamics of non-linear nature [1, 2]. In addition, other groups have demonstrated that this non-linear behaviour can also exist under the influence of drugs [3], or similarly, under the influence of environmental factors. Any new knowledge on the mechanisms underlying cell proliferation is

¹ This study is supported in part by Norwegian, Iceland, Lichtenstein & Hellenic ministry of Finance Grant EL0049.



of major importance, and even the smallest of indications towards a certain direction could enable us to further discover differences in the mechanisms distinguishing between health and disease. This issue is especially important in tumors, the incidence of which is approaching that of an epidemic. In the present study we have focused on the dynamics that have been revealed through an *in vitro* cell system and particularly on the dynamics manifested under the influence of a certain type of chemotherapeutic i.e. glucocorticoids. Glucocorticoids (GC) are among the most important alternatives in the treatment of leukemia. Resistance to glucocorticoids represents a crucial parameter in the prognosis of leukemia [4-6], whereas it has been shown that GC-resistant T-cell leukemia cells manifest a biphasic mechanism of action or imply an inherent resistance mechanism of action to glucocorticoids [7]. New questions arise regarding the nature of the dynamics of a cell population under the influence of a drug. If certain physical measures, such as proliferation, are observed on the phenotypic level, how are these translated on the molecular, genomic level? For example, if a cell population increases its rate of proliferation, does it mean that the genes required for this effect transcribe faster than usual? An interesting report by *Mar et al. (2009)* suggested that gene expression takes place in quanta, i.e. that it happens discretely and not continuously [8, 9]. Also, in two other reports it was suggested that gene expression follows oscillatory patterns, which makes things even more complicated with regards to the proliferation rate, be it growth acceleration or deceleration [10, 11]. This means that cells cannot simply transit from one state to another in terms of growth rate. Should the hypothesis of oscillatory modulation of gene expression, which implies non-linearity, stand correct, then a much more complicated regulatory pattern is required by a cell so as to change its state, as a function of environmental stimuli. The present work provides evidence supporting this view, with respect to glucocorticoids.

2. The Model and Simulations

In order to establish a modeling approach to the phenomenon described above, we have discriminated between different cell populations. That is, if at time t a cell population is considered to be N , then this is a mixture of cells in various stages. More specifically, we have discriminated between the cell cycle phases and cell death. The cell cycle is the path through which cells manifest proliferation. The identification of cells in specific cell cycle phases is of critical importance since it will determine cellular proliferation, cessation or cell death. Also, in various systems the detection of cells at specific cell cycle points denotes a mechanism of reaction to an environmental stimulus, as for example in the present case is the glucocorticoid. In Figure 1, we present the model diagrammatically.

The diagram in Figure 1, represents the three phases of the cell cycle. Where, $G_{1,t}$, $G_{1,t+1}$, $G_{1,t+n}$ is the number of cells in G_1 phase at time t , $t+1$ and $t+n$ respectively, S_t , S_{t+1} , S_{t+n} is the number of cells in S phase at time t , $t+1$, $t+n$ respectively, $G_{2,t}$ is the number of cells in G_2 phase at time t , $t+1$, $t+n$ respectively and CD_t , CD_{t+1} , CD_{t+n} is the number of dead cells at time t , $t+1$,

$t+n$ respectively. The arrows connecting the different cell states denote the possibilities that a cell has to transit from one state to another. So, for example, a cell in G_1 phase has three possibilities: to remain in the G_1 phase, to transit to the S phase or to become apoptotic i.e. cell death (CD). This means that it is impossible for the cell to go from the G_1 phase to G_2 phase. A very important factor denoted in Figure 1 is the $K_{factor,t}$, which denotes the rate of transition from one cell state to another. Hence, the factor k will take the following subscripts:

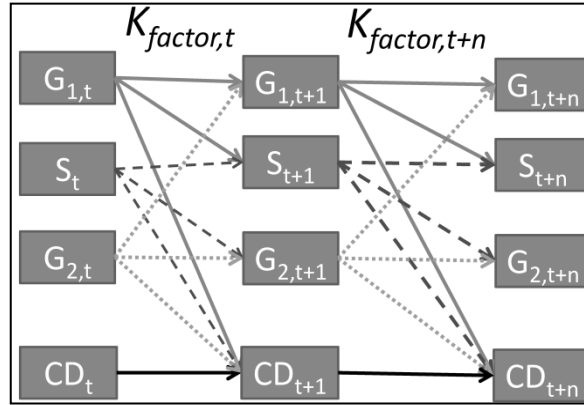


Fig. 1. A schematic representation of the model approach for cell population showing transitions between cell cycle phases and cell death.

$$\begin{aligned} G_{1,t} &\rightarrow G_{1,t+1}: k_1, G_{1,t} \rightarrow S_{t+1}: k_2, G_{1,t} \rightarrow CD_{t+1}: k_3, \\ S_t &\rightarrow S_{t+1}: k_4, S_t \rightarrow G_{2,t+1}: k_5, S_t \rightarrow CD_{t+1}: k_6 \\ G_{2,t} &\rightarrow G_{2,t+1}: k_7, G_{2,t} \rightarrow G_{1,t+1}: k_8, G_{2,t} \rightarrow CD_{t+1}: k_9 \\ CD_t &\rightarrow CD_{t+1}: k_{10} \end{aligned}$$

The following equations describe the transitions from one state to the next:

$$N_{G_{1,t+1}} = N_{G_{1,t}} \cdot k_1 + N_{G_{2,t}} \cdot k_8$$

$$N_{S_{t+1}} = N_{S_t} \cdot k_4 + N_{G_{1,t}} \cdot k_2$$

$$N_{G_{2,t+1}} = N_{G_{2,t}} \cdot k_7 + N_{S_t} \cdot k_5$$

$$N_{CD_{t+1}} = N_{CD_t} + N_{G_{1,t}} \cdot k_3 + N_{G_{2,t}} \cdot k_9 + N_{S_t} \cdot k_6$$

Where, N denotes the respective cell population at time t . These equations could be formulated in more generalized form since each population at time $t+1$ consists of two other populations at time t . Hence, the generalized form would be:

$$N_{p_x,t+1} = N_{p_y,t} k_y + N_{p_z,t} k_z$$

In other words, our model shows that the next state is defined by the previous one. Each cell subpopulation consists of parts of the other subpopulations.

These equations appear to be of linear form and are simple to solve. Yet, the factor k is a non-linear factor, which can be determined only experimentally. It is dependent upon environmental factors $f(environmental)$, such as nutrient availability and space, and in the present case is a function of glucocorticoid concentration $f(C_p)$. In Figure 2, experimental measurements are presented as an effort to calculate the rate of population change for the total population and data were fitted with Fourier series. We have reported this previously, that cell populations defined experimentally, could be described with Fourier series, with respect to the transition factor k [12].

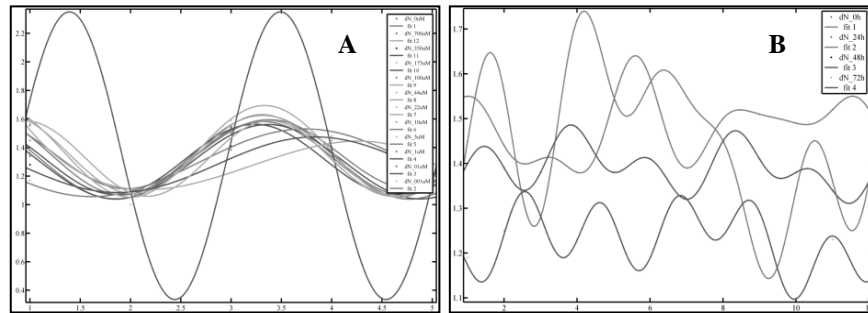


Fig. 2. Simulating the factor k in relation to time (A) and glucocorticoid concentration (B) showed that both could be fitted with Fourier series. In (A) the x-axis corresponds to experimental values from time point measurements of cell numbers, while each curve corresponds to the respective k factor of each glucocorticoid concentration. Similarly, in (B) the x-axis corresponds to the glucocorticoid concentrations and each curve corresponds to the time points measured.

The generalized form of the series we have used for our approach was given by:

$$f(x, y) = a_0 + a_1 \cos(xy) + a_2 \sin(xy)$$

Hence, the factor k for each transition, meaning from one cell state to the next would be given by the following system of equations:



$$\begin{aligned}
 k_1 &= a_{0,1} + a_{1,1} \cos(N_{G_{1,t}} \cdot N_{G_{1,t+1}}) + a_{2,1} \sin(N_{G_{1,t}} \cdot N_{G_{1,t+1}}) \\
 k_2 &= a_{0,2} + a_{1,2} \cos(N_{G_{1,t}} \cdot N_{S_{t+1}}) + a_{2,2} \sin(N_{G_{1,t}} \cdot N_{S_{t+1}}) \\
 k_3 &= a_{0,3} + a_{1,3} \cos(N_{G_{1,t}} \cdot N_{CD_{t+1}}) + a_{2,3} \sin(N_{G_{1,t}} \cdot N_{CD_{t+1}}) \\
 k_4 &= a_{0,4} + a_{1,4} \cos(N_{S_t} \cdot N_{S_{t+1}}) + a_{2,4} \sin(N_{S_t} \cdot N_{S_{t+1}}) \\
 k_5 &= a_{0,5} + a_{1,5} \cos(N_{S_t} \cdot N_{G_{2,t+1}}) + a_{2,5} \sin(N_{S_t} \cdot N_{G_{2,t+1}}) \\
 k_6 &= a_{0,6} + a_{1,6} \cos(N_{S_t} \cdot N_{CD_{t+1}}) + a_{2,6} \sin(N_{S_t} \cdot N_{CD_{t+1}}) \\
 k_7 &= a_{0,7} + a_{1,7} \cos(N_{G_{2,t}} \cdot N_{G_{2,t+1}}) + a_{2,7} \sin(N_{G_{2,t}} \cdot N_{G_{2,t+1}}) \\
 k_8 &= a_{0,8} + a_{1,8} \cos(N_{G_{2,t}} \cdot N_{G_{1,t+1}}) + a_{2,8} \sin(N_{G_{2,t}} \cdot N_{G_{1,t+1}}) \\
 k_9 &= a_{0,9} + a_{1,9} \cos(N_{G_{2,t}} \cdot N_{CD_{t+1}}) + a_{2,6} \sin(N_{G_{2,t}} \cdot N_{CD_{t+1}}) \\
 k_{10} &= 1
 \end{aligned}$$

We could write this system of equations in a more generalized form, which would be:

$$k = a_0 + a_1 \cos(N_{p_{y,z},t} N_{p_{x,t+1}}) + a_2 \sin(N_{p_{y,z},t} N_{p_{x,t+1}})$$

Where k is the transition factor, $a_{0,1,2}$ are constants, $N_{p1,t}$ and $N_{p2,t+1}$ are the populations implicated in the transition at time t and $t+1$ respectively.

Substituting the equation describing the generalized k with the equation of the generalized $N_{p,t+1}$ we obtain:

$$\begin{aligned}
 N_{p_{x,t+1}} &= N_{p_{y,t}} \left[a_0 + a_1 \cos(N_{p_{y,t}} N_{p_{x,t+1}}) + a_2 \sin(N_{p_{y,t}} N_{p_{x,t+1}}) \right] \\
 &\quad + N_{p_{z,t}} \left[a_0 + a_1 \cos(N_{p_{z,t}} N_{p_{x,t+1}}) + a_2 \sin(N_{p_{z,t}} N_{p_{x,t+1}}) \right]
 \end{aligned}$$

This equation describes the transition of a cell population from one state to the next but it cannot be solved analytically. Solutions can only be found numerically, since future populations (N_x) depend on the previous ones and on the fraction of other future cell populations ($N_{y,z}$). In Figure 3, we have performed numerical approximations of the function in order to represent it schematically. The function appeared to give interesting dynamics as it manifested a saddle point. Also, these phenomena were time dependent, as clearly seen on the experimental level. Thus, by differentiating with respect to time we could obtain a possible role of the temporal factor in this system. Similarly, we have made numerical approximations in order to design the dynamics of the first derivative for both variables, that is $N_{p,y}$ and $N_{p,z}$. The result is presented in Figure 4.

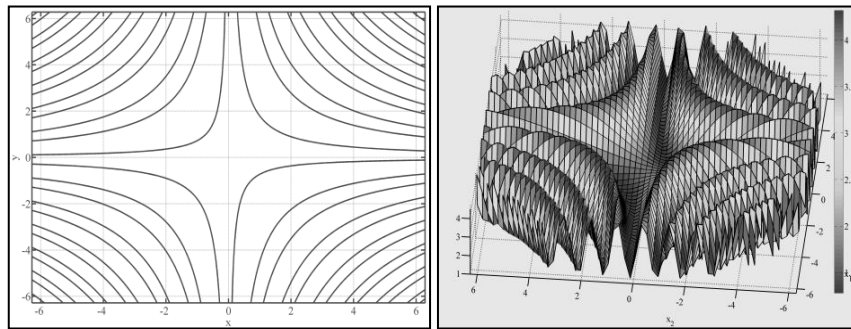


Fig. 3. Using a numerical approximation of the function describing the population transitions manifested interesting dynamics as they formed a saddle.

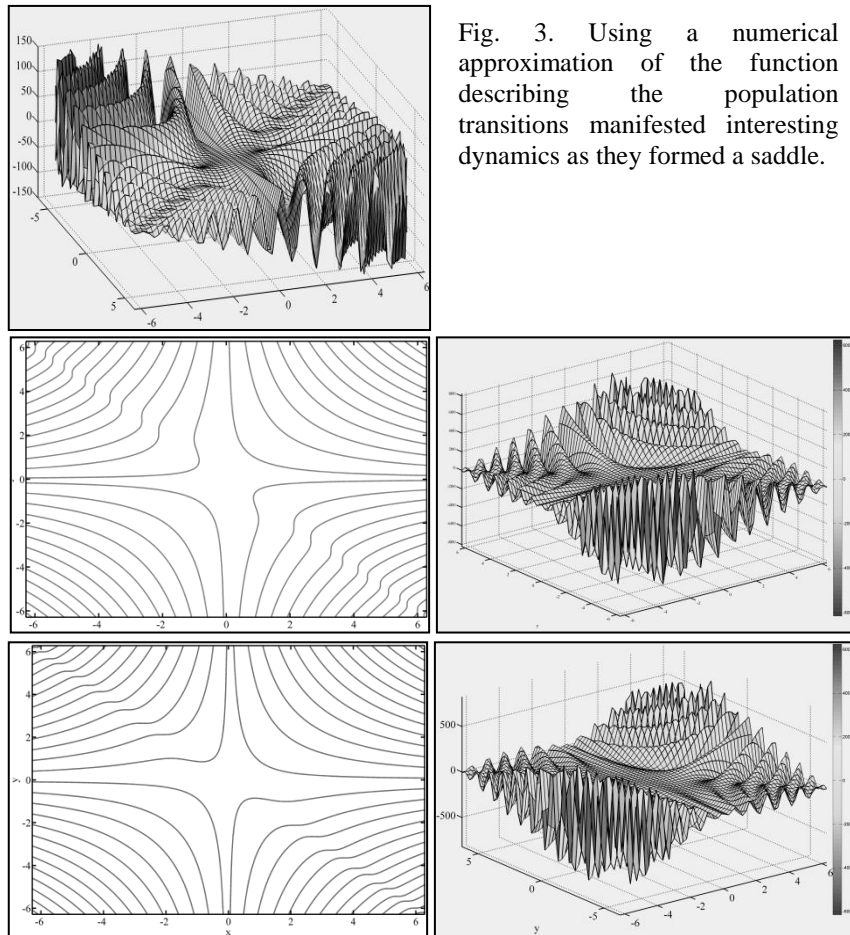


Fig. 4. Numerical representation of the first partial derivative with respect to $N_{p,y}$ (upper left and right) and with respect to $N_{p,z}$ (lower left and right).



3. Conclusions

In the present work we have attempted to identify non-linear factors of cell proliferation under the influence of chemotherapeutics, and more specifically under the influence of the glucocorticoid prednisolone. We have attempted to establish an initial theoretical framework for the analysis of such phenomena and for future considerations. Cell growth appeared to be of a non-linear character. This knowledge could prove useful in the treatment of tumors since understanding the biology of proliferation would lead us to a better understanding of cellular resistance to chemotherapeutics. Biological systems are extremely complicated and they manifest, without doubt, non-linear/chaotic phenomena. Therefore, as we have mentioned in previous works, we believe that the maturity of biological sciences would come through integration with other disciplines, such as mathematics and physics, and the ability to give generalized models for these phenomena. Such an example is the understanding of cell proliferation in which we attempted to contribute with hints.

References

1. Wolfrom, C., et al., *Evidence for deterministic chaos in aperiodic oscillations of proliferative activity in long-term cultured Fao hepatoma cells*. J Cell Sci. **113** (Pt 6): p. 1069-74, 2000.
2. Laurent, M., J. Deschatrette, and C.M. Wolfrom, *Unmasking chaotic attributes in time series of living cell populations*. PLoS One. **5**(2): p. e9346,
3. Guerroui, S., J. Deschatrette, and C. Wolfrom, *Prolonged perturbation of the oscillations of hepatoma Fao cell proliferation by a single small dose of methotrexate*. Pathol Biol (Paris). **53**(5): p. 290-4, 2005.
4. Den Boer, M.L., et al., *Patient stratification based on prednisolone-vincristine-asparaginase resistance profiles in children with acute lymphoblastic leukemia*. J Clin Oncol. **21**(17): p. 3262-8, 2003.
5. Lauten, M., et al., *Clinical outcome of patients with childhood acute lymphoblastic leukaemia and an initial leukaemic blood blast count of less than 1000 per microliter*. Klin Padiatr. **213**(4): p. 169-74, 2001.
6. Cario, G., et al., *Initial leukemic gene expression profiles of patients with poor in vivo prednisone response are similar to those of blasts persisting under prednisone treatment in childhood acute lymphoblastic leukemia*. Ann Hematol. **87**(9): p. 709-16, 2008.
7. Lambrou, G.I., et al., *Prednisolone exerts late mitogenic and biphasic effects on resistant acute lymphoblastic leukemia cells: Relation to early gene expression*. Leuk Res, 2009.
8. Mar, J.C. and J. Quackenbush, *Decomposition of gene expression state space trajectories*. PLoS Comput Biol. **5**(12): p. e1000626, 2009.
9. Mar, J.C., R. Rubio, and J. Quackenbush, *Inferring steady state single-cell gene expression distributions from analysis of mesoscopic samples*. Genome Biol. **7**(12): p. R119, 2006.
10. Chabot, J.R., et al., *Stochastic gene expression out-of-steady-state in the cyanobacterial circadian clock*. Nature. **450**(7173): p. 1249-52, 2007.
11. Degenhardt, T., et al., *Population-level transcription cycles derive from stochastic timing of single-cell transcription*. Cell. **138**(3): p. 489-501, 2009.



12. Lambrou, G.I., et al. *Studying the Nonlinearities of T-cell Leukemia Growth and the Underlying Metabolism Upon Glucocorticoid Treatment through the Application of Dynamic Mathematical Methodologies* in *ITAB 2010*. 2010. Corfu, Greece: IEEE.



Decoding of Atmospheric Pressure Plasma Emission Signals for Process Control

Victor J Law¹, F T O'Neill², D P Dowling², J L Walsh³, F Iza³, N B Janson⁴,
and M G Kong³

¹Dublin City University, National Centre for Plasma Science and Technology, Collins Avenue, Glasnevin, Dublin 9, Dublin, Ireland.

(e-mail: vic.law@dcu.ie)

²School of Mechanical and Materials Engineering, University College Dublin, Belfield, Dublin 4, Ireland.

³Department of Electronic and Electrical engineering, Loughborough University, Leicestershire LE11 3TU UK.

⁴School of Mathematics, Loughborough University, Leicestershire LE11 3TU UK.

Abstract: Three-dimensional phase-space representation and 3-dimensional surface imaging using single scalar time series data obtained from two very different atmospheric pressure plasma systems is presented. The process of delay embedding, Savitzky-Golay digital filtering and deconvolution of frequency-domain data is described.

Keywords: Plasma, Electrical measurement, Electro-acoustic, Overtones, LabVIEW.

1. Introduction

Low-temperature, non-thermal atmospheric pressure plasma jets (APPJ) are being developed for surface treatment of biomedical devices, sterilisation, and therapeutic techniques, such as wound sterilisation and cancer treatment [1]. In addition to these medical applications, APPJ are now routinely employed in the automotive (car head lamps) and aerospace (fuselage and wing components) industry for surface activation of polymer prior to bonding [2]. This paper describes some of the emerging plasma electrical and electro-acoustic metrology that is being developed for the diagnostics and control of APPJ systems. In particular the requirement for extraction of information that describes the tempo-spatial heterogeneous processes. The methodology to obtain this information is currently in its infancy when compared to low pressure plasma metrology [3]. In this paper the multivariate analysis tools for the 3-dimensional phase-space representation from a single scalar time series, either of a single observable in the time-domain, or temporal-spatial deconvolutions of a single observable in the frequency-domain are given. The use of these tools to obtain measurements on two APP jet systems is presented: a hand-held plasma jet [4]; and an industrial scale computer numerical controlled PlasmaTreat OpenAir™ APPJ system [5 and 6]. By comparing the diagnostic information obtained using these two APPJ systems the robustness of the diagnostic techniques for both laboratory and industrial scale APPJ are demonstrated.

2. 3-D representation of a signal observation: Current

Cold APPJ pens (some times called pencils or needles) are increasingly used in many processing applications due to a distinct combination of their inherent plasma stability with excellent reaction chemistry that is often enhanced downstream. The term *cold* used here refers to temperatures of less than 50°C at the point of contact and so enables the treatment of temperature sensitive living tissue and organic polymers. An example of the helium APPJ pen examined in this study, which is driven at a drive frequency of 18 kHz, is shown in figure 3.1 and discussed in detail in references [1 and 4].

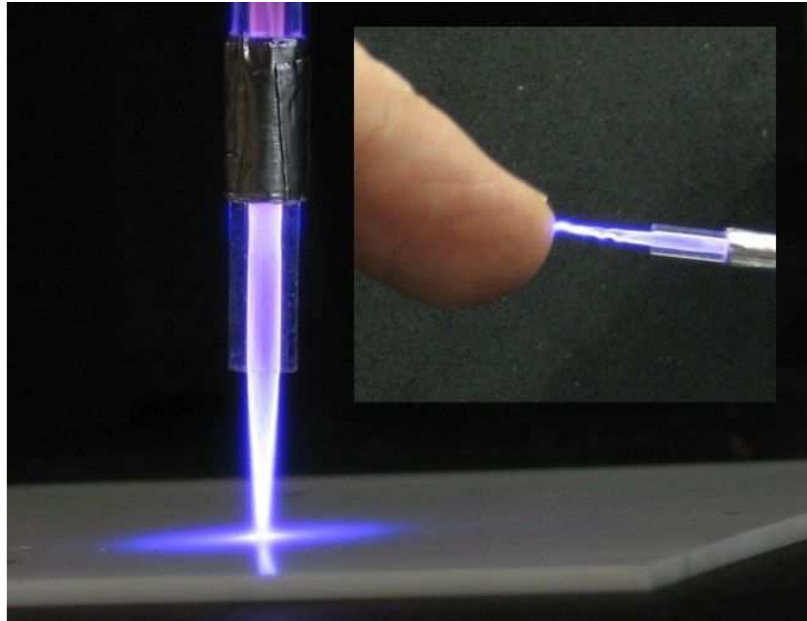


Figure 2.1: Image of a cold AAPJ pen and interaction with human figure.

This section of the paper describes one of the emerging metrology techniques that can characterise the APPJ pen's three modes of operation (chaotic, bullet and continuous). However, when there is access to only one single observable, namely, the current at the driving electrode $I(t)$, defining these modes becomes a challenge. Figure 2.2 details the current waveform for each of the three modes of operation. A common feature of all three modes is that their current waveform has one distinct peak every positive half cycle of the applied voltage and one current peak every negative half cycles, but later this is not always the case. The chaotic mode is observed immediately after breakdown, and an increase in the input power eventually leads to the bullet mode and then to the continuous mode. As the mode changes to bullet and then on to continuous, the current peaks become stronger and regular and finally adding an additional current peak per voltage cycle in the continuous mode.

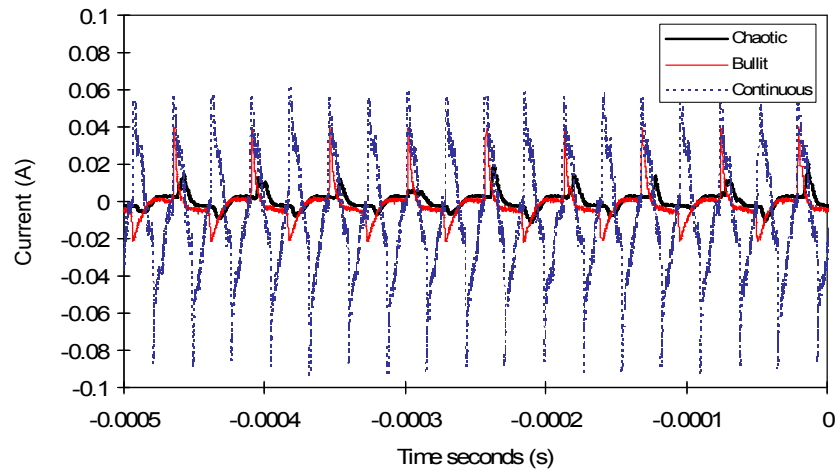


Figure 2.2: APPJ pen current waveforms in the chaotic, bullet and continuous modes.

In order to introduce a phase-space representation of the APPJ current waveform the technique of embedding is used [7]. In particular, we use the delay embedding within which the state vector at time t in the 3-dimensional phase space is reconstructed as a vector whose coordinates are the values of the single observable taken at time moments separated by a certain delay τ , namely, $(I(t), I(t + \tau), I(t + 2\tau), \dots, I(t + (m - 1)\tau))$. The number m is the embedding dimension and depends on the dimension of the attractor in the original dynamical system. For visualization purposes, here we choose $m = 3$. The time delay τ can be chosen by a variety of methods, but one of the most popular approaches is to calculate the mutual information from the variables $I(t)$ and $I(t + \tau)$ as a function of τ , and to choose its first minimum [8]. The value of τ obtained by this method was close to $4\mu\text{s}$ for all datasets and was chosen for the phase-space reconstruction in this study.

Figures 2.3(*chaotic*), (*bullet*) and (*continuous*) shows 3-dimensional phase space reconstructions for the APPJ pen operating in the chaotic, bullet and continuous modes, respectively. For each mode, the phase trajectory is shown during several hundred excitation cycles. Whereas figures 2.3(*bullet*) and (*continuous*) show limit cycles (i.e. periodic attractors), figure 2.3(*chaotic*) shows a set that does not look similar to a limit cycle, nor to a low-dimensional torus representing a quasi periodic (i.e. non-chaotic) behaviour. We therefore suggest that this is a projection of a chaotic Attractor into a three-dimensional space

An alternative to the 3-dimensional phase-space reconstruction of the current waveform is to cut the block of sequentially sampled data points in to n -frames, with each frame length equal to one complete drive frequency period, T , (where $T = 1/f$), followed by alignment of each frame, to a common zero-crossing-point, within the block of data. The data displayed in figure 2.2 is used for this time-domain reconstruction and has been performed in a LabVIEW program [9]

where the recorded length was found to be 555 points per period of the 18 kHz drive frequency. The computed results are shown in figure 2.4 for each of the modes (*chaotic*, *bullet* and *continuous*).

Initial comparison between the two methods visually demonstrates that both reconstructions delineate the chaotic mode. Indeed the positive current peak deterministic Jitter, as measured in the time-domain, is of the order of $5\mu\text{s}$, which is close to the τ value used in the phase space reconstructions. However, the 3-dimensional phase space reconstructions provide poor visual discrimination between the bullet and continuous modes. This is because the current frequency doubling information contained in the continuous time-domain display is not clearly resolved in the phase space reconstruction. The outcome of this limited comparison suggest that a suitable attractor for representing the three APPJ pen modes can be found within the supposition of n -frames within a current waveform data block. In addition time-domain n -frame suppositions reveal the modes and therefore can be used to characterize and map the time resolved visual properties of each mode, see reference [4].

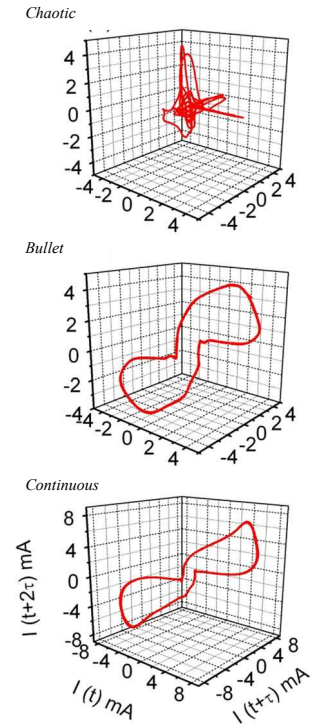


Figure 2.3: APPJ pen phase space reconstruction for each mode.

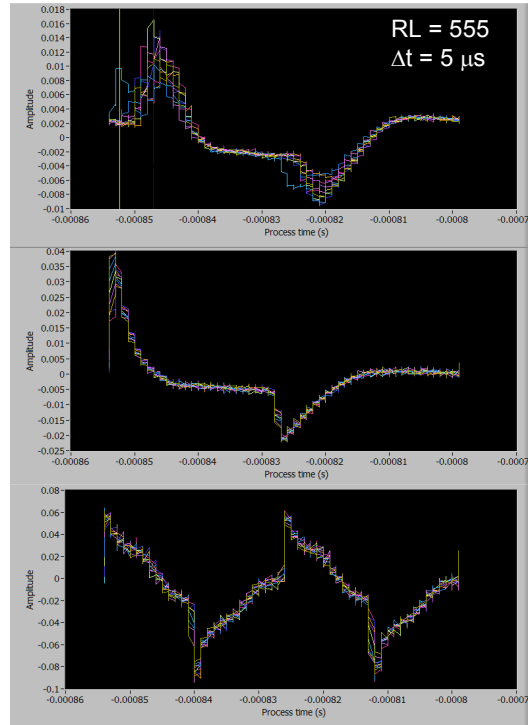


Figure 2.4: APPJ time-domain n -frame representation for each mode.



3. Deconvolution of a single observation: Electro-acoustic

The PlasmaTreat OpenAir™ APPJ is used worldwide and represents a typical APPJ in the manufacturing sector. Full technical details of the APPJ are given in references [5, 6]. In this study the APPJ is electrically driven at 19 kHz and the working (ionisation) gas is Air. The first impression of this APPJ that it is much larger than the plasma pencil design, and the sound emitted by this APPJ is generally 30 dB above the environment sound level. This section is concerned with the decoding of the APPJ electro-acoustic emission [10] and the use of parts of the conditioned signal for process control.

As with reference [10] the electro-acoustic signal is captured by a microphone and sampled using a computer soundcard followed by a Fast Fourier Transform. LabVIEW 8.2 software is used to present the raw data in frequency-domain (0-60 kHz span). Within the software a Savitzky-Golay digital filter [11] is chosen to piece-by-piece smooth the raw data by least square minimisation with a polynomial function ($m = 1$) within a moving window. The windowing is express in the following form, where k is the \pm sampled data points.

$$2k + 1$$

Figure 3.1a and b shows the raw un-filtered dataset (gray trace) and the filtered dataset (black trace) under plasma plume free expansion conditions. Experimentally it is found that a $k = 10$ preserves the high Q-factor ($f/\Delta f$ -3 dB bandwidth ~ 200) frequency registration of the 19 kHz drive signal and its harmonics plus reduces the measurement noise floor to -100 dB that results in a signal-to-noise ratio (SRN) of 50 dB ± 3 dB: a 20 dB improvement when compared to the unfiltered dataset SRN. The second feature of note is the 3 broad peaks at 10-11, 25-30 and 45 kHz. The frequency spacing between these peaks may be represented mathematically using a quarter standing-wave closed air-column (clarinet model) [7] and so describes the longitudinal mode within the APPJ nozzle.

$$f_n = \frac{nc}{4(L + 0.6r)}$$

In the above equation, n is modulo frequency number, L is the physical length of the nozzle ($L = 8$ mm), $0.6r$ is the end correction, where r is the internal radius of the nozzle) and c_{sound} is the sound velocity in air. For this model the exit aperture of the nozzle defines the maximum pressure vibration, and the internal nozzle aperture, (where the compressed air is at 1.5 atmospheres) is the antinode. Using this quarter standing-wave model only the fundamental and odd number overtones are supported. For example, f_0 and $n = 3, 5$, etc.... This model, at room temperature 25°C (where the speed of sound in air equates to 346.26 m.s⁻¹) yields frequency values of $f_n = 9.11$ kHz, $f_3 = 27.33$ kHz, and $f_5 = 45.55$ kHz. The values of f_n and $f_3 = 3$ approximates to the broad peaks observed in figure 3.1a.

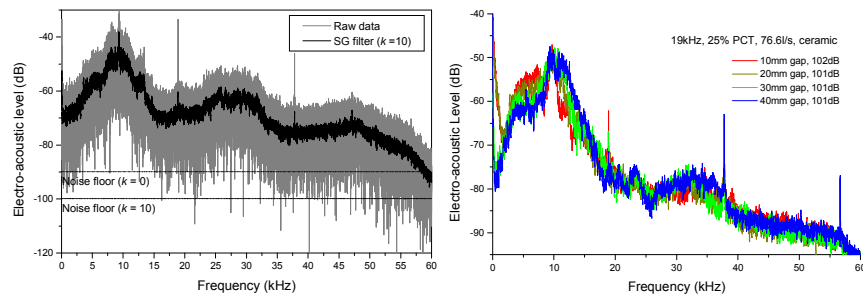


Figure 3.1a: APPJ raw signal and SG filtered signal. Figure 3.1b: APPJ SG filtered signal as a function nozzle-surface distance.

Having established the typical spectrum of the APPJ electro-acoustic emission, the focus of this section now moves to examining the electro-acoustic signal as a function APPJ nozzle to surface distance, or gap. Figure 3.1.b provides four measurements at gaps: 10, 20, 30 and 40 mm at $k=10$. Under these conditions the electrical drive at $f_0 = 19$ kHz and its harmonics ($f_2 = 38$ kHz and $f_3 = 57$ kHz) are constant in their frequency registration. In addition the three broad peaks are still present. However a new broad peak at 4-8 kHz emerges and grows in amplitude as the gap distance is reduced. In addition, sound pressure level measurements indicate an increase of 1 dB from 101 to 102 dB.

The information obtained from this study allows the single observable electro-acoustic signal to be tested for specific conditions at discrete frequency bands. This procedure is readily implemented in LabVIEW software using lower and upper limits at the discrete frequency bands. When the signal amplitude breaches these limits, an out of bound condition fail is registered and a simple audio-visual alarm is triggered to warn the operator, or a binary code (0 or 1) from the comparator [30] may also be hard wired for data logging.

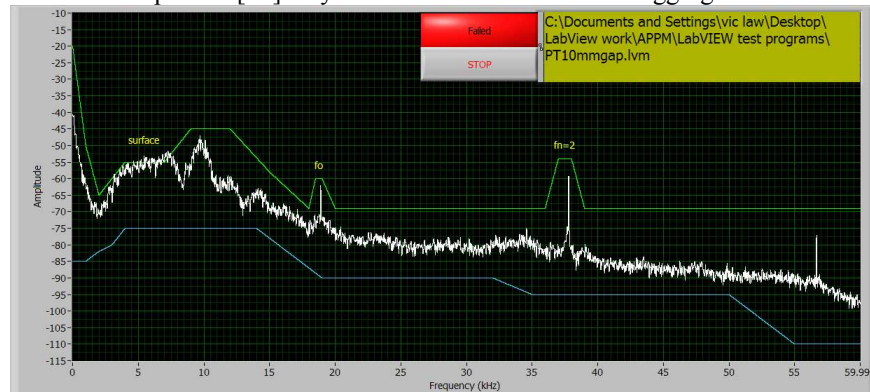


Figure 3.2: A LabVIEW screen data demonstrating how the system can be used for process control. In this case 'Fail' is associated with variation in signal in the 4 to 8 kHz frequency range.

The ability to locate a surface has many technological uses including 3-dimensional imaging of plasma treated topographical surfaces. This section presents a LabVIEW program [10] that records the electro-acoustic emission, as the APPJ traverse back and forth across a metal work piece, and transfers the sequentially sampled data points into n-frames within a block to produce a 3-D image of the topographical surface. Figure 3.3 provides a simplified block diagram of the software where some of the control subroutines (vi(s)) have been removed for clarity.

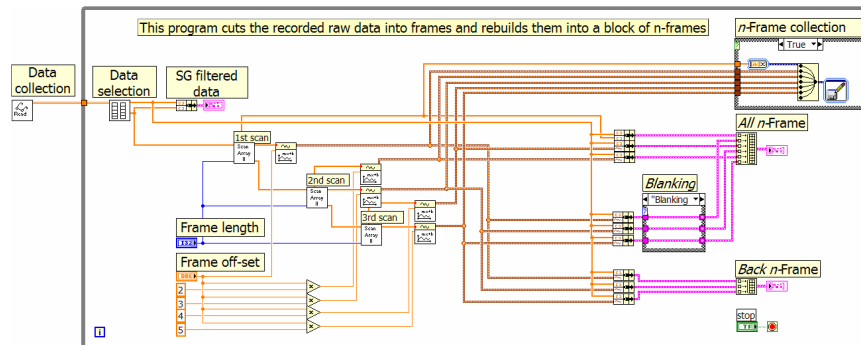


Figure 3.3: Simplified block diagram of the 3-D surface imaging software.

Figure 3.4 provides a 3-dimensional image of a 10 mm wide by 2 mm thick plate with a 2 mm diameter hole drilled in the middle of the surface. Each of the 9 scans is off-set by 2 mm, with the first scan recording the CNC positioning the APPJ to the start of the plasma process. Only the forward scans are recorded with the return blanked off. Note the acoustic discontinuity where the 2 mm hole is located.

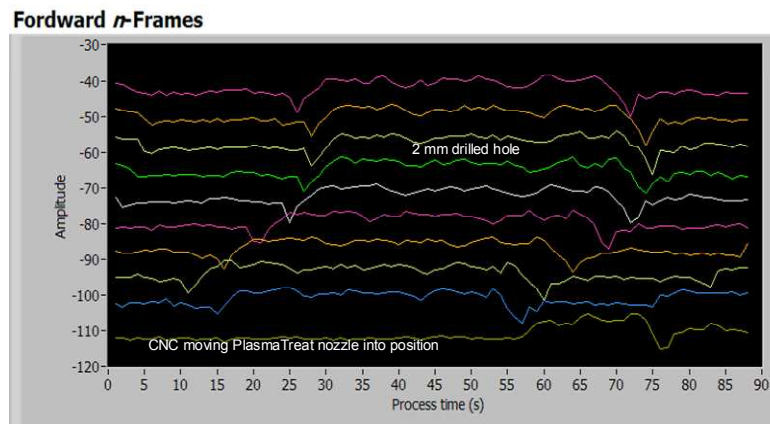


Figure 3.4: Nine scan 3-D surface image of metal surface with a 2 mm hole. Blanking turned on.



4. Conclusions

Atmospheric pressure plasma jets offer enhanced quality of care at reduced cost and will be of immense societal and commercial value. This invited paper has reviewed both time-domain current waveforms and deconvolution of electro-acoustic emission (in the frequency-domain) of two (hand-held and industrial scale APPJ systems). In the first case, 3-dimensional delay embedding was compared to periodic analysis using n -frames within a data block was compared. Both techniques provide information on the chaotic mode, with the latter yielding information on all three modes.

For the industrial scale system, single scalar time series, in the form of electro-acoustic emission is readily available. Here temporal-spatial deconvolution of the data provides information on the jet nozzle surface location and surface topology.

Acknowledgements

This work is supported by Science foundation Ireland 08/SRC/I1411. MGK, FI and JLW thank support from EPSRC.

References

1. M. G. Kong, G. Kroesen, G. Morfill, T. Nosenko, T. Shimizu, J. van Dijk and J. L. Zimmermann. Plasma medicine: an introductory review. *New Journal of Physics*, Vol. 9, 115012 (35pp), 2009.
2. R. Suchentrunk, H. J. Fuessler, G. Staudigl, D. Jonke, and M. Meyer. Plasma surface engineering - innovative processes and coating systems for high-quality products. *Surface and Coatings Technology*, vol. 112, no. 1-3, 351-357, 1999.
3. J. Ringwood, S. Lynn, G. Bacilli, B. Ma, E. Ragnoli and S. Mcloone. Estimation and Control in Semiconductor etch: practice and possibilities. *IEEE, Trans, Semicond, Manuf*, vol. 23, no.1, 87-96, 2010.
4. J. L. Walsh, F. Iza, N. B. Janson, V. J. Law and M. G. Kong Three distinct modes in a cold atmospheric pressure plasma jet. *J, Phys, D: Appl, Phys*, vol. 43, no. 7, 075201 (14pp), 2010.
5. D. P. Dowling, F. T. O'Neill, S. J. Langlais and V. J. Law, Influence of dc pulsed atmospheric pressure plasma jet processing conditions on polymer activation. *Submitted to Plasma Process Polym.* 2010.
6. V. J. Law, F. T. O'Neill and D. P. Dowling. Evaluation of the sensitivity of electro-acoustic measurements for process monitoring and control of an atmospheric pressure plasma jet system. *Submitted to PSST.* 2010.
7. N. Packard, J. Crutchfield, D. Farmer, and R. Shaw. Geometry from time series. *Phys. Rev. Lett*, vol. 45, no. 9, 712-716, 1990.
8. A M Fraser and H L Swinney. Independent coordinates for strange attractors from mutual information. *Phys. Rev A*, vol. 33, no. 2, 1134-1140, 1986.
9. The LabVIEW software can be obtained from the principal author: vic.law@dcu.ie
10. V J Law, C E Nwankire, D P Dowling, and S Daniels. Acoustic emission within an atmospheric helium corona discharge jet. "Chaos Theory: Modeling, Simulation and Applications.". Editors: C H. Skiadas, I Dimotikalis and C Skiadas. Publisher: World Scientific Publishing Co Pte Ltd. pp 155-164, 2011.
11. A. Savitzky, and M. J. Golay. Smoothing and differentiation of data by simplified least squared procedures. *Analitical chemistr*, vol. 36, no.8, 1627-2639, 1964.



Chaos in a simply formulated dry-friction oscillator

Gábor Licskó¹ and Gábor Csernák²

¹ Department of Applied Mechanics

Budapest University of Technology and Economics

² HAS-BUTE Research Group on Dynamics of Machines and Vehicles

Műegyetem rkp. 5., 1111 Budapest, Hungary

(E-mail: licsko@mm.bme.hu, csernak@mm.bme.hu)

Abstract. Chaotic oscillators with Coulomb-type friction were extensively studied in the past. However, these investigations mostly deal with rather complex mechanical models that are closely related to everyday's engineering applications. In the present paper, we introduce a stick-slip oscillator consisting only of a spring and a block sliding on a rough surface, and the block is periodically forced. A simple friction law is implemented in which we consider sticking and sliding coefficients of friction. We show with the help of numerical simulation that the system can behave chaotically in certain parameter domains. We use common numerical techniques to visualize chaos and also try to estimate the value of the maximal Lyapunov exponent. We also point out the possibility of transient chaos by means of cobweb diagrams.

Keywords: dry-friction, stick-slip, forced oscillator, transient chaos.

1 Introduction

Investigating piecewise-smooth dynamical systems became very prevalent during the last decade. Plenty of studies deal with non-smooth systems subjected to dry-friction and try to unfold non-linear phenomena and chaotic behaviour. However, in most cases the mechanical model is derived from real-world applications such as disc brakes which makes the models rather complex [1,2]. Some other investigations use very simple models with the simplest variant of Coulomb-type friction and carry out a detailed non-smooth bifurcation analysis [3,4]. They investigate bifurcation scenarios that are peculiar to systems with dry-friction.

In this article the very simple frictional oscillator presented in [5–8] will be used and extended with a little more advanced friction model already mentioned by Hinrichs et al. [2]. It will be shown that for certain parameters the system will behave chaotically. Moreover, signs of transient chaos will be highlighted.

2 The mechanical and mathematical model

The mechanical model consists of a block sliding on a rough surface. It is driven by a harmonic excitation force while supported by a linear spring as depicted in Fig. 1. The equation of motion of the system can be written in

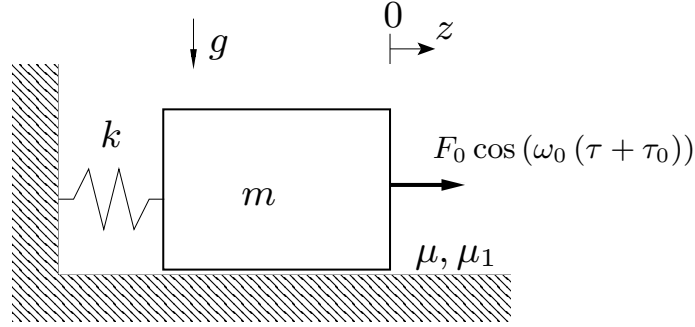


Fig. 1. Mechanical model

the following form:

$$mz'' + kz = F_0 \cos(\omega_0 (\tau + \tau_0)) - \mu mg f(z'),$$

where τ is time and $()'$ denotes time derivative, z is the displacement of the block, m is the total mass of the moving elements, k is the spring stiffness, F_0 is the amplitude of the excitation force, ω_0 is the angular excitation frequency, μ is the sliding coefficient of friction, g is the gravitational acceleration and $f(z')$ can be an arbitrary function of the velocity that models the friction characteristics.

After transforming the system into dimensionless form (See [7]) we obtain the following equations that describe the motion:

$$\ddot{x} + x = \cos(\Omega(t + t_0)) - Sf(\dot{x}) \quad (1)$$

$$f(\dot{x}) \in \begin{cases} 1 & \text{if } \dot{x} > 0 \\ [-S_1/S, S_1/S] & \text{if } \dot{x} = 0 \\ -1 & \text{if } \dot{x} < 0 \end{cases},$$

where $\dot{()}$ denotes non-dimensional time derivative. We rescaled time by $t = \tau\sqrt{k/m}$ and displacement by $x = zk/F_0$. The non-dimensional constants are $\Omega = \omega\sqrt{m/k}$, $S = \mu mg/F_0$ and $S_1 = \mu_1 mg/F_0$. Here the friction function assumes that the friction force at sticking can be greater than at sliding. Therefore μ_1 will be the sticking coefficient of friction. This model will be the subject of our further investigations.



3 Numerical analysis

Exact solutions exist that satisfy Eq.(1) between two consecutive stops, i.e. when the velocity is zero in the form:

$$x^{\pm}(t) = A^{\pm} \cos(t) + B^{\pm} \sin(t) + L \cos(\Omega t) + K \sin(\Omega t) \mp S, \quad (2)$$

where A^{\pm} and B^{\pm} are determined by initial conditions. The plus and minus signs indicate different constants for positive and negative velocity respectively. K, L can be expressed as

$$K = \frac{\sin(\Omega t_0)}{\Omega^2 - 1}, \quad L = -\frac{\cos(\Omega t_0)}{\Omega^2 - 1}.$$

This enables us to avoid solving the system of ordinary differential equations however, we also tried this latter approach. When using Eq.(2) the only uncertainty will be finding the time instants when velocity changes sign and also when the stuck body starts sliding again. A Matlab program was developed that considers these cases and performs the simulation of the model.

Earlier investigations [7] of one of the present authors showed that the behaviour of the system changes at resonant excitation frequencies, namely, the symmetric solutions become asymmetric in the sense that the absolute values of turnaround displacements during one excitation period become different. Also the resonant bands open up if a friction coefficient for sticking different from sliding is introduced. This led us to choose parameters for resonant solutions. We stuck to the case $\Omega = 0.5$ and $S_1 = 0.4$ and carried out numerical simulations. First a brute-force bifurcation analysis was done for positive initial conditions where the last ten sticking displacements were registered at the end of each run.

We found period-doubling bifurcation and signs of chaotic behaviour if the ratio S/S_1 is small enough (See Fig. 2). In this particular case period-adding occurs at $S/S_1 = 0.17175$ (Point *I* in Fig. 2) followed by a chaotic band at $S/S_1 = 0.139$ that suddenly vanishes at $S/S_1 = 0.109$ (Point *II*). Furthermore periodic solution exists between $S/S_1 = 0.089 - 0.109$ (Point *III*) and a more extended chaotic motion can be seen below $S/S_1 = 0.089$ (Point *IV*). In addition to the results in [7] we found that the solution's symmetry also vanishes at $S/S_1 = 0.835$ by the separation of sticking and sliding coefficients of friction (Point *V*). For the characterization of symmetry of the solutions we introduced the following formula:

$$\aleph = \sum_{i=1}^n x(\sigma_i)$$

assuming σ_i to be time instants in one excitation period when $\dot{x}(\sigma_i) = 0$ ($\sigma_i \in [0; \frac{2\pi}{\Omega}]$, $i = 1, \dots, n$). The symmetry-changing can be seen in panel two of Fig. 2 where $\aleph = 0$ means that the solution is symmetric. Solutions

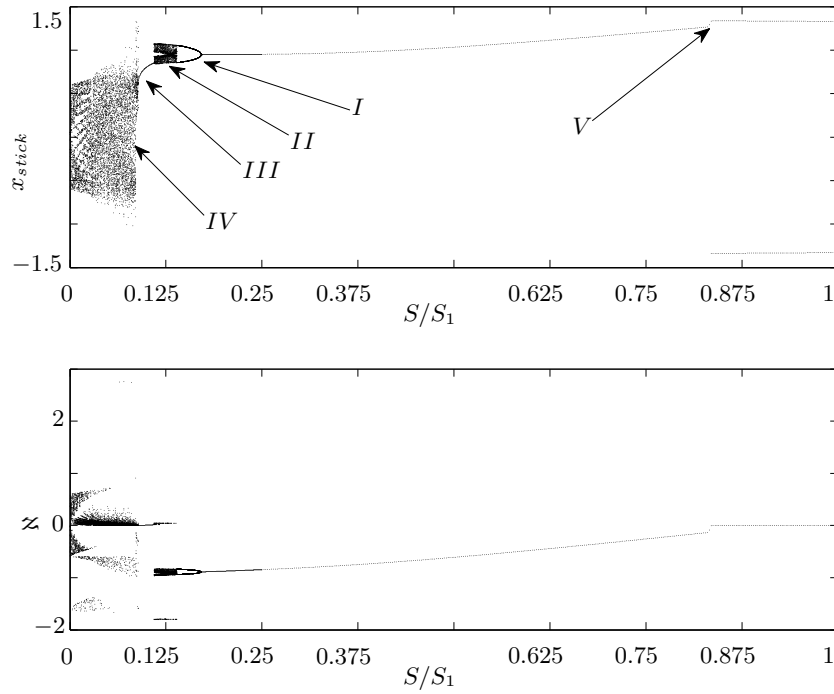


Fig. 2. Monte Carlo bifurcation diagram for $S/S_1 = 0 - 1$ depicting the sticking displacement and asymmetry of solutions. Parameters were $S_1 = 0.4$ and $\Omega = 0.5$.

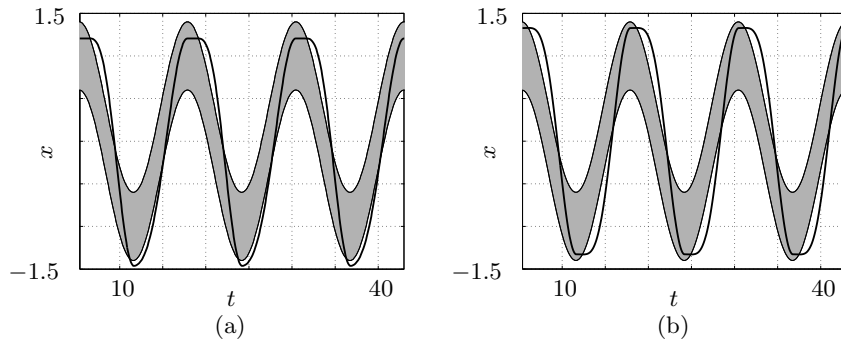


Fig. 3. (a) Asymmetric ($S/S_1 = 0.75$) and (b) symmetric ($S/S_1 = 1$) solutions for the parameters $S_1 = 0.4$ and $\Omega = 0.5$.



become asymmetric in a way that one of the two sticking occurrences vanishes during an excitation period by a *crossing-sliding* bifurcation according to [3]. An asymmetric and a symmetric solution can be seen in Fig. 3 before and after the symmetry breaking. The grey filled area in the figure is the region of sticking. If the solution's velocity becomes zero inside this area then it will be stuck until the excitation overcomes the sticking friction force and the spring force.

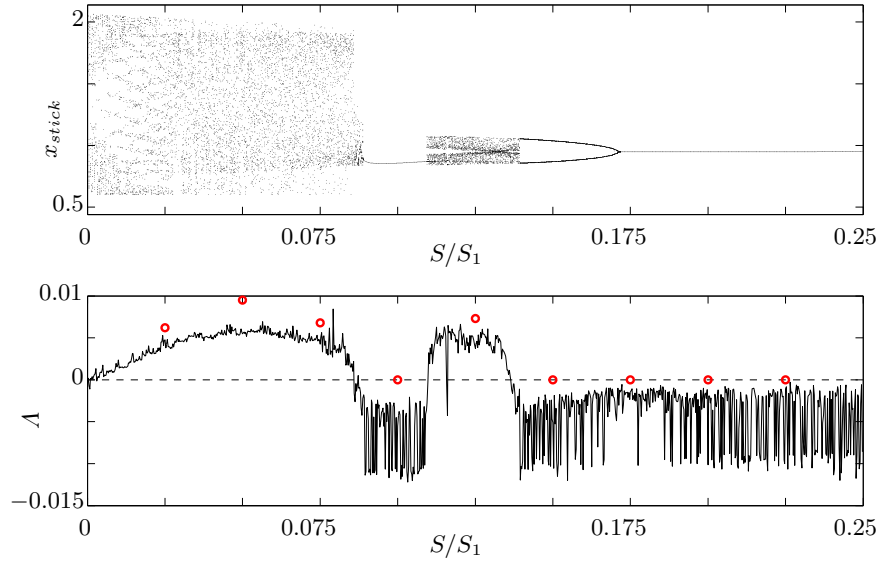


Fig. 4. Bifurcation diagram and Lyapunov exponents for $S/S_1 = 0 - 0.25$ with parameters $S_1 = 0.4$ and $\Omega = 0.5$. (Solid lines - direct numerical simulation of nearby trajectories, red circles - method for non-smooth systems [9]).

Fig. 4 is the enlargement of Fig. 2 for the parameters $S/S_1 = 0 - 0.25$ also showing the maximal Lyapunov exponent. Black solid lines indicate results computed from two nearby trajectories' separation while red circles refer to a method published by Stefanski and Kapitaniak [9] that is developed for piecewise-smooth systems. This latter method relies on the synchronisation of two similar systems by a coupling parameter q . In our case the coupled system of first order equations are as follows:

$$\begin{aligned} \dot{x}_1 &= x_2 \\ \dot{x}_2 &= -x_1 + \cos(\Omega(t + t_0)) - Sf(x_1) \\ \dot{x}_3 &= x_4 + q(x_1 - x_3) \\ \dot{x}_4 &= -x_3 + \cos(\Omega(t + t_0)) - Sf(x_3) + q(x_2 - x_4) \end{aligned}$$

In order to obtain the maximal Lyapunov exponent we have to carry out a brute-force bifurcation analysis taking q as bifurcation parameter. When the two coupled systems are fully synchronised, i.e. the solutions evolve identically then the coupling parameter will become the maximal Lyapunov exponent. An example for the process [9] can be seen in Fig. 5. The method

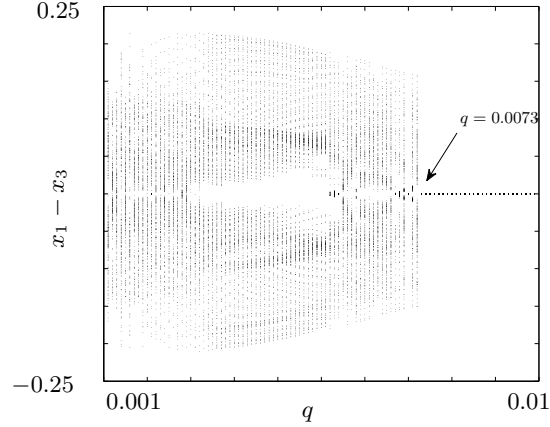


Fig. 5. Monte Carlo diagram for the coupling parameter q as bifurcation parameter. Synchronisation occurs at $q = 0.0073$ thus $\Lambda = 0.0073$. ($S/S_1 = 0.125$, $\Omega = 0.5$)

is only able to return positive value for the exponent. If the system does not behave chaotically then we only can say that Λ is less than or equal to zero. An acceptably good coincidence between direct simulation and the synchronisation method can be seen though the one described in [9] could be accepted as more exact since here we have to deal with non-smooth equations.

$$\Lambda = \frac{1}{n} \sum_{i=1}^n \frac{1}{\Delta t} \frac{|d_{i+1}|}{|d_i|}, \quad (3)$$

During direct numerical simulation Eq.(3) is evaluated for the nearby trajectories where d_{i+1} is the distance between the trajectories at the $i+1$ -st time sample Δt time after distance d_i was sampled. One certain issue with this calculation can be when one of the initial trajectories suddenly sticks while the other one still slides. In this case the rate of separation of the trajectories may not be exponential. Another issue arises when both trajectories stick at the same displacement hence the quotient when computing the Lyapunov exponent will be either zero (when both solutions just stuck) or infinity when the earlier distance was zero. These cases have to be neglected in the calculation.

In order to illustrate chaos cobweb diagrams are often used. This was one of the earliest methods that we deployed searching for chaos. At that early stage we integrated the first order system of ODE's to obtain numerical solution. We discovered that at certain parameters the solution seems to escape from a repellor into an attractor. This scenario is depicted in Fig. 6. The parameters were $S/S_1 = 0.125$, $S_1 = 0.4$ and $\Omega = 0.5$. If we look

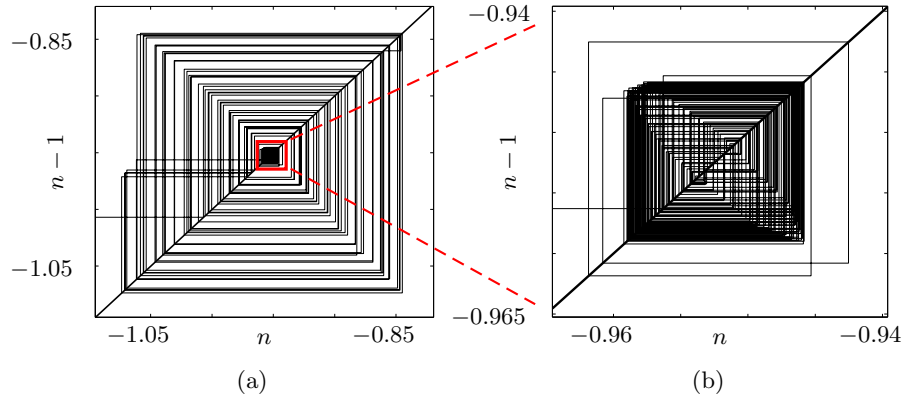


Fig. 6. Cobweb diagrams showing how solutions of the system of ODE's escape from a repellor. Panel (b) is the enlargement of the red square on panel (a). ($S/S_1 = 0.125$, $S_1 = 0.4$, $\Omega = 0.5$.)

at Fig. 2, we see that for these values there is purely chaotic behaviour to expect. However not far away from this point in Fig. 4 a negative spike can be discovered in the Lyapunov exponent plot ($S/S_1 = 0.116$). If we run simulation with the analytical solutions and plot the displacement against time, we see a slight change in behaviour (See Fig. 7). This qualitative change is hardly visible in any cobweb diagram since the magnitude of displacements are almost the same, however it may be a sign of transient chaos that should be investigated in detail.

4 Conclusions and future work

In this work we carried out a numerical bifurcation analysis of a simply formulated dry-friction oscillator. We showed that by using different coefficients of friction for sliding and sticking a qualitative change occurs in the behaviour of the system. Namely, symmetric solutions become asymmetric. Moreover, by further decreasing the sliding coefficient of friction chaotic motion arises that is followed by a periodic band and end up in chaos. This chaotic behaviour was proved by calculating the maximal Lyapunov exponent in two

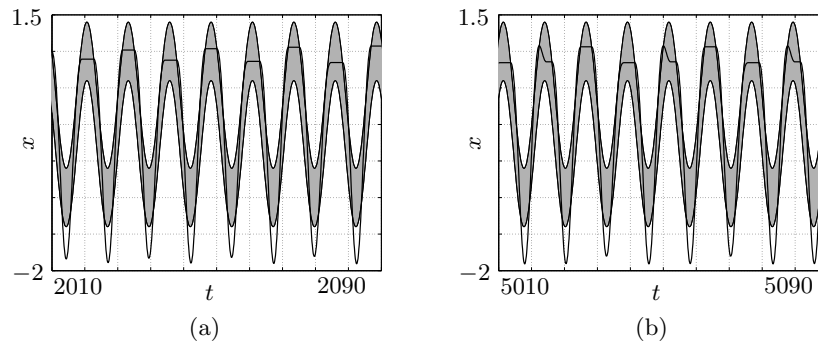


Fig. 7. Chaotic behaviour (a) turns into a period-three motion (b). ($S/S_1 = 0.116$, $S_1 = 0.4$, $\Omega = 0.5$)

different ways that show acceptable coincidence. Finally, we highlighted the possibility of transient chaos that may arise inside a very narrow band of the bifurcation parameter.

Further investigation will focus on the chaotic behaviour of the system if friction coefficients are closer to each other since this case is closer to reality. Closer attention should be paid to unfold the transient chaotic behaviour.

Acknowledgement: This research is supported by the Hungarian Scientific Research Found under Grant no. OTKA 83890.

References

- 1.K. V. Avramov and J. Awrejcewicz. Frictional oscillations under the action of almost periodic excitation. *Meccanica*, 40:2, 2006.
- 2.N. Hinrichs, M. Oestreich and K. Popp. On the modelling of friction oscillators. *Journal of Sound and Vibration*, 216:3, 1998.
- 3.P. Kowalczyk and P. T. Piiroinen. Two-parameter sliding bifurcations of periodic solutions in a dry-friction oscillator. *Physica D* 237:8, 2008.
- 4.M. Guardia et al. An analytical approach to codimension-2 sliding bifurcations in the dry friction oscillator. *SIAM J. on App. Dyn. Sys.*, 9:3, 2010.
- 5.J.P. Den Hartog. Forced Vibrations with Combined Coulomb and Viscous Damping. *Trans. Am. Soc. Mech. Eng.* 53, 1930.
- 6.S.W. Shaw. On the dynamic response of a system with dry friction, *Journal of Sound and Vibration*. *Journal of Sound and Vibration* 108:2, 1986.
- 7.G. Csernák and G. Stépán. On the periodic response of a harmonically excited dry friction oscillator. *Journal of Sound and Vibration* 295:3-5, 2006.
- 8.G. Csernák, G. Stépán and S. W. Shaw. Sub-harmonic resonant solutions of a harmonically excited dry friction oscillator. *Nonlinear Dynamics* 50:1, 2007.
- 9.A. Stefanski and T. Kapitaniak. Using chaos synchronisation to estimate the largest Lyapunov exponent of nonsmooth systems. *Discrete Dynamics in Nature and Society* 4:3, 2000.



Fractal Geometry and Architecture Design: Case Study Review

Xiaoshu Lu^{1,3}, Derek Clements-Croome², Martti Viljanen¹

¹Department of Civil and Structural Engineering, School of Engineering, Aalto University, PO Box 12100, FIN-02150, Espoo, Finland

E-mail: xiaoshu@cc.hut.fi

²School of Construction Management and Engineering, Whiteknights, University of Reading, PO Box 219, Reading RG6 6AW, U.K

³Finnish Institute of Occupational Health, Finland

Abstract: The idea of building in harmony with nature can be traced back to ancient Egyptians, China, Greeks and Romans. The increasing concerns on sustainability oriented on buildings have added new challenges in building architectural design and called for new design responses. Sustainable design integrates and balances the human geometries and the natural ones. As the language of nature, it is, therefore, natural to assume that fractal geometry could play a role in developing new forms of aesthetics and sustainable architecture design. This paper gives a brief description of fractal geometry theory and presents its current positioning and recent developments through illustrative review of some fractal case studies in architectural design, which provides a bridge between fractal geometry and architecture design.

Keywords: Fractal geometry, Architecture design, Sustainability.

1. Introduction

The idea of building in harmony with nature can be traced back to ancient Egyptians, China, Greeks and Romans. At the beginning of 21st century, the increasing concerns on sustainability oriented on buildings have added new challenges in building architectural design and called for new design responses. As the language of nature [1,2], it is, therefore, natural to assume that fractal geometry could play a role in developing new forms of design of sustainable architecture and buildings.

Fractals are self-similar sets whose patterns are composed of smaller-scales copied of themselves, possessing self-similarity across scales. This means that they repeat the patterns to an infinitely small scale. A pattern with a higher fractal dimension is more complicated or irregular than the one with a lower dimension, and fills more space. In many practical applications, temporal and spatial analysis is needed to characterise and quantify the hidden order in complex patterns, fractal geometry is an appropriate tool for investigating such complexity over many scales for natural phenomena [2,3]. Order in irregular pattern is important in aesthetics as it embraces the concept of dynamic force,



which shows a natural phenomenon rather than mechanical process. In architecture design terms, it represents design principle. Therefore, fractal geometry has played a significant role in architecture design.

In spite of its growing applications, such works in literature are rather narrow, i.e. they mainly focus on applications for fractal design patterns on aesthetic considerations. Few works have related to comprehensive and unified view of fractal geometry in structural design, for example, as it is intended in this study. We aim to fill in this gap by introducing fractals as new concepts and presenting its current positioning and recent developments in architecture through illustrative review of some fractal case studies in design. The paper shows that incorporating the fractal way of thinking into the architecture design provides a language for an in-depth understanding of complex nature of architecture design in general. This study distills the fundamental properties and the most relevant characteristics of fractal geometry essential to architects and building scientists, initiates a dialogue and builds bridges between scientists and engineers.

2. Basic Theory of Fractal Geometry

2.1. Basic Theory

The mathematical history of fractals began with mathematician Karl Weierstrass in 1872 who introduced a Weierstrass function which is continuous everywhere but differentiable nowhere [4]. In 1904 Helge von Koch refined the definition of the Weierstrass function and gave a more geometric definition of a similar function, which is now called the Koch snowflake [5], see Figure 1. In 1915, Waclaw Sielpinski constructed self-similar patterns and the functions that generate them. Georg Cantor also gave an example of a self-similar fractal [6]. In the late 19th and early 20th, fractals were put further by Henri Poincare, Felix Klein, Pierre Fatou and Gaston Julia. In 1975, Mandelbrot brought these work together and named it 'fractal'.

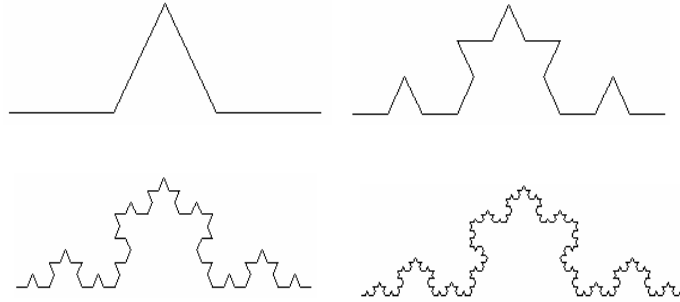


Fig. 1. Illustration of Koch Curve.

Fractals can be constructed through limits of iterative schemes involving generators of iterative functions on metric spaces [2]. Iterated Function System (IFS) is the most common, general and powerful mathematical tool that can be used to generate fractals. Moreover, IFS provides a connection between fractals and natural images [7,8]. It is also an important tool for investigating fractal sets. In the following, an introduction to some basic geometry of fractal sets will be approached from an IFS perspective. In a simple case, IFS acts on a segment to generate contracted copies of the segment which can be arranged in a plane based on certain rules. The iteration procedure must converge to get the fractal set. Therefore, the iterated functions are limited to strict contractions with the Banach fixed-point property.

Let (X, d) denotes a complete metric space and $H(X)$ the compact subsets of X , the Hausdorff distance is defined as

$$h(A, B) = \max \{d(A, B), d(B, A)\} \quad \forall A, B \in H(X) \quad (1)$$

It is easy to prove that h is a metric on $H(X)$. Moreover, it can be proved that $(H(X), h)$ is also a complete metric space [7] which is called the space of fractals for X .

A contraction mapping, or contraction $w: X \mapsto X$ has the property that there is some nonnegative real number $k \in [0, 1)$, contraction factor k , such that

$$d(w(x), w(y)) \leq k d(x, y) \quad (2)$$

In non-technical terms, a contraction mapping brings every two points closer in the metric space it maps. The Banach fixed point theorem guarantees the existence and uniqueness of fixed points of contract maps on metric spaces: If



$w: X \mapsto X$ is a contraction, then there exists one and only one $x \in X$ such that $w(x) = x$.

The Banach fixed point theorem has very important applications in many branches of mathematics. Therefore, generalisation of the above theorem has been extensively investigated, for example in probabilistic metric spaces. The theorem also provides a constructive method to find fixed-point.

An IFS [9] is a set of contraction mappings w_i defined on (X, d) with contraction factor k_i for $i = 1, 2, \dots, N$. We denote it as $\{X; w_i, i = 1, 2, \dots, N\}$ with contraction factor $k = \max\{k_i, i = 1, 2, \dots, N\}$.

Based on the above described work, Hutchinson [9] proved an important theorem on a set of contraction mappings in which IFS is based: Let $\{X; w_i, i = 1, 2, \dots, N\}$ be an IFS with contraction factor k . Then $W: H(X) \mapsto H(X)$ defined as

$$W(B) = \bigcup_{i=1}^N w_i(B) \quad \forall B \in H(X) \quad (3)$$

is a contraction mapping on $(H(X), h)$. From Banach's theorem, there exists a unique set $A \in H(X)$, the attractor of IFS, such that

$$A = W(A) = \bigcup_{i=1}^N w_i(A) \quad (4)$$

It can be seen that A is self-similar since it is expressed as a union of transformations (copies) of itself. The attractor A can be taken as a definition of deterministic fractals.

2.2. Fractal dimensions

Mandelbrot [2] proposed a simple but radical way to qualify fractal geometry through fractal dimension based on a discussion of the length of the coast of England. The dimension is a statistical quantity that gives an indication of how completely a fractal appears to fill space, as one zooms down to finer and finer scales. This definition is a simplification of Hausdorff dimension that Mandelbrot used to based. We focus on this one and briefly mentions box-counting dimension because of its widely practical applications. However, it should be noted that there are many specific definitions of fractal dimensions, such as Hausdorff dimension, Rényi dimensions, box-counting dimension and correlation dimension, etc, none of them should be treated as the universal one.



For $A \in H(X)$, let $n(A, \varepsilon)$, $\varepsilon > 0$, denote the smallest number of closed balls of radius ε needed to cover A . If

$$D = \lim_{\varepsilon \rightarrow 0} \frac{\log n(A, \varepsilon)}{\log \frac{1}{\varepsilon}} \quad (5)$$

exists, then D is called the fractal dimension of A .

So $n(A, \varepsilon)$ is proportional to ε^{-D} as $\varepsilon \rightarrow 0$ or the exponent D is in $n(A, \varepsilon) = \varepsilon^{-D}$ which is the power law relationship. A power law describes a dynamic relationship between two objects which portrays a wide variety of natural and man-made phenomena. A key feature of the power law is that the power law relationship is independent of scales. A good example of intuition of fractal dimension is a line with the length of ε_n , where ε is the measuring length. Assume the line is divided in 3 equal parts and $\varepsilon = \frac{1}{3}$ then the simplified $n(A, \varepsilon) = \varepsilon^{-D}$ gives $3 = (1/3)^{-D}$ with $D = 1$. Similarly, the Koch curve's fractal dimension is $D = \frac{\log 4}{\log 3} = 1.26$.

Practically, the fractal dimension can only be used in the case where irregularities to be measured are in the continuous form. Natural objects offer a lot of variation which may not be self-similar. The Box-counting dimension is much more robust measure which is widely used even to measure images. To calculate the box-counting dimension, we need to place the image on a grid. The number of boxes, with size s_1 , that cover the image is counted (n_1). Then the number of a smaller grid of boxes, with size s_2 , is counted (n_2). The fractal dimension between two scales is then calculated by the relationship between the difference of the number of boxed occupied and the difference of inverse grid sizes [10]. In more chaotic and complex objects such as architecture and design, more flexible and robust measures, such as range analysis, midpoint displacement, etc, can be employed. For more detailed information, readers may refer to Bovill's book [10].

2.3. Examples of IFS applications

Fractal geometry is at the conceptual core of understanding nature's complexity and the IFS provides an important concept for understanding the core design of the natural objects as well as approximating the natural design. In this subsection we outline the evolution of the idea of IFS with our calculation examples.



We know that the Banach's fixed-point theorem forms the basis of the IFS applications. However, applying the theorem in practice raises two central questions. One is to find the attractor for a given IFS. The other is to find IFS for a given attractor, an inverse problem of the first.

For the first problem, the attractor can be obtained by successive approximations from any starting point theoretically. From a computational point of view, two techniques, deterministic and stochastic, can be applied. The deterministic algorithm starts with an arbitrary initial set to reach the attractor. The stochastic algorithm is often more complex but more efficient. A stochastic algorithm associates to the IFS system a set of probabilities by assigning a probability to each mapping, which are used to generate a random walk. If we start with any point and apply transformations iteratively, chosen according to the probabilities attached, we will come arbitrarily close to the attractor. The associated probabilities determine the density of spatially contracted copies of the attractor. Therefore, the probabilities have no effect on the attractor but influence significantly the rendering of its approximations.

The second problem, the inverse problem, can be solved by Barnsley's Collage Theorem, a simple consequence of Banach's fixed point theorem. Such procedure was illustrated nicely through the 'Barnsley fern' in [9] and [11] using four-transformation IFS with associated probabilities. Figure 2 shows our calculation examples of fractals using four-transformation IFS with variations and their associated probabilities produced by Matlab, where 20000 iterations were set. These fractals actually have more than one attractor. In Figure 2, the four-transformation matrices are

$$A = \begin{bmatrix} 0 & 0 & 0 \\ 0 & 0.18 & 0 \\ 0 & 0 & 1 \end{bmatrix} B = \begin{bmatrix} 0.19 & -0.25 & 0 \\ 0.22 & 0.23 & 1.7 \\ 0 & 0 & 1 \end{bmatrix} C = \begin{bmatrix} -0.15 & 0.28 & 0 \\ 0.24 & 0.25 & 0.44 \\ 0 & 0 & 1 \end{bmatrix} D = \begin{bmatrix} 0.76 & 0.04 & 0 \\ -0.05 & 0.95 & 1.7 \\ 0 & 0 & 1 \end{bmatrix} \quad (6)$$

D has the probability 0.75 and others 0.083.

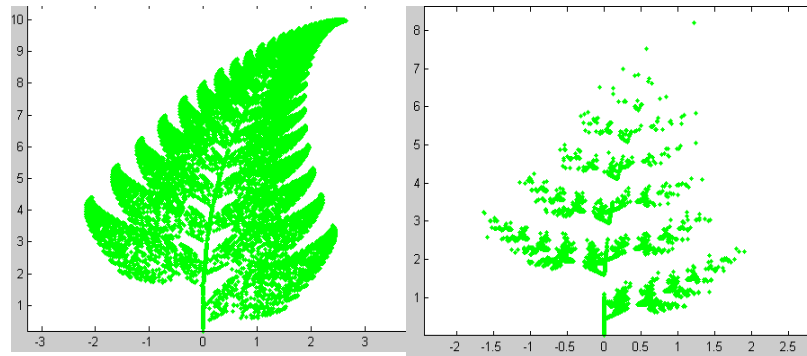


Fig. 2. Calculation examples of fractals using IFS with variations.

3. Applications of Fractal Geometry to Architecture Design

3.1. Applications of IFS

IFS provides wide range of architectural design applications in patterns and structures. Very often, IFS codes are used to generate fractals. For example, topology (layout) optimization has been proposed and is based on IFS representations with various applications [12]. Chang [13] proposed a hierarchical fixed point-searching algorithm for determining the original coordinates of a 2-D fractal set directly from its IFS code. The IFS code can be modified according to the desired transformation. Figure 3 shows the Castle with different reflection directions generated by the modified IFS codes.

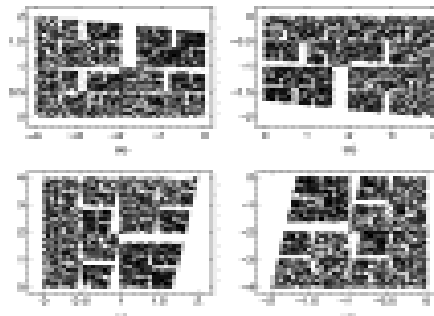


Fig. 3. Castle example generated by the modified IFS codes [13].

3.2. Applications of fractal geometry

Fractal geometry has been applied in architecture design widely to investigate fractal structures of cities [14] and successfully in building geometry [15,16] and design patterns [10].

Early fractal building patterns can be traced to ancient Maya settlement. Brown et al. analysed fractal structures of Maya settlement and found that fractals exhibit both within communities and across regions in various ways: at the intra-site, the regional levels and within archaeological sites. Moreover, spatial organisation in geometric patterns and order are also fractals, which presents in the size-frequency distribution, the rank-size relation among sites and the geographical clustering of sites [17]

In Europe, fractals were found in the early 12th century buildings. The floor of the cathedral of Anagni in Italy built in 1104 is adorned with dozens of mosaics in a form of a Sierpinski gasket fractal (See Figure 4).



Fig. 4. The floor of the cathedral of Anagni in Italy [18].

Fractals have been applied to many elevation structures to exclusively address power and balance. Some very excellent examples of classical architecture can be seen in many parts of the Europe, in the Middle East and Asia which have effects of fractal elevations, for example, Reims' cathedral and Saint Paul church in France, Castel del Monte in Italy and many palaces in Venice (ca' Foscari, Ca' d'Oro, Duke Palace, Giustinian Palace) in Italy. Venice has been one of the most talked about fractal Venice [18] (see Figure 5). More vital evidence shows that fractals exist in Gothic cathedral in general. The pointed arch, an impression of elevation, appear in entrance, at windows, at the costal arch with many scales and details [19]. Figure 6 displays the elevations of a five-floor tenement building in the historical part of Barcelona which shows self-organisation structure.

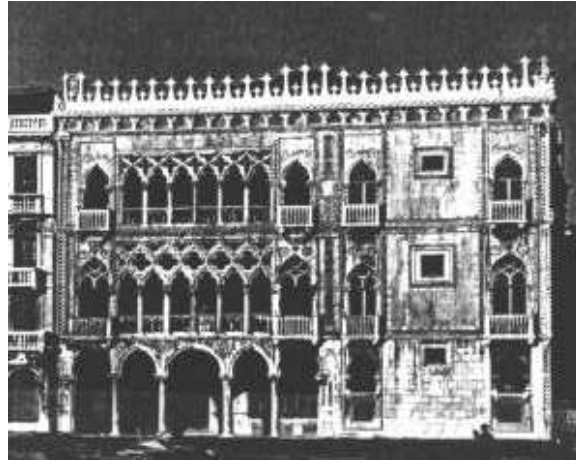


Fig. 5. Fractal building in Venice [18].

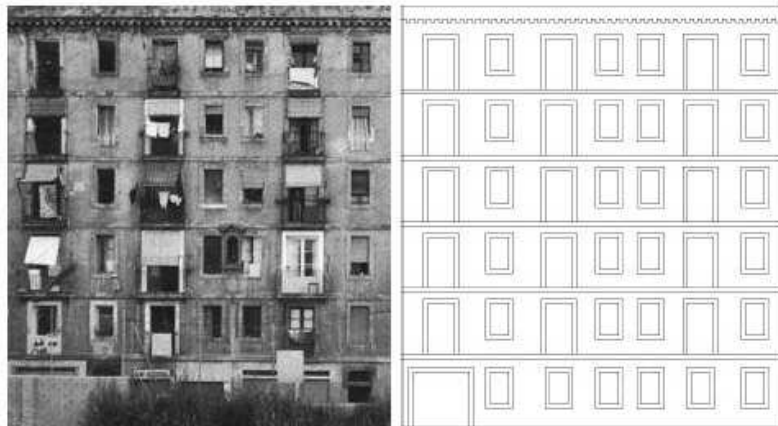


Fig. 6. A tenement house in the historical part of Barcelona, Spain: the elevation's photograph from the 90-s (left part of figure); the geometric synthesis shows the original architecture design (middle part) [20].

In the Middle East, fractal patterns have been adopted widely in designing stucco, a typically Persian art form for the decoration of dome interiors. In Figure 7, the pattern in the dome interior has four attractors surrounding the main one at the center (Sarhangi).



Fig. 7. Stucco dome interior in a private house in Kashan [21].

In Asia, architectures with fractal structures have also been found in Humayun's Mausoleum, Shiva Shrine in India and the Sacred Stupa Pha That Luang in Laos. Fractals have been used to study Hindu temples. In China, some mosques in the west were more likely to incorporate such domes which are fractals. One important feature in Chinese architecture is its emphasis on symmetry which connotes a sense of grandeur [22].

Besides geographical localities, in recent times, the concept of fractals has been extended in many well known architectures including Frank Lloyd Wright's 'Robie House', 'Fallingwater', 'Palmer house' and 'Marion County Civic', which demonstrate that fractals have universal appeal and are visually satisfying because they are able to provide a sense of scale at different levels. Wright is one of the most representatives of organic architects. His designs grew out of the environment with regards to purpose, material and construction [10]. Fractals have inspired many great modern designers such as Zaha Hadid, Daniel Liebeskind, Frank Gehry and others with many notable fractal architectures [20]. Indeed, according to Ibrahim et al, architects and designers started to adopt fractals as a design form and tool in 1980th [10]. Yessios et al. was among the first utilizing fractals and fractal geometry design in architecture [23]. They developed a computer program to aid architecture using fractal generators. In 1990th, Durmisevic and Ciftcioglu applied fractal tree as an indicator of a road infrastructure in the architecture design and urban planning [24].

Wen et al. established the fractal dimension relations matrix table analysis to classify architecture design style patterns for the masterpieces of three modern architecture masters: Frank Lloyd Wright, Le Corbusier and Mies van der Rohe [25]. Figure 8 shows the results. It can be seen that the temporal trends of individuals vary. The fractal dimensions of Frank Lloyd Wright are average with low beginning in the early 1900th and end in the mid 1930th. The trend of Le Corbusier goes downside with gentle slope from mid 1900th to mid 1950th. For the period shown in the grape, the trend of Mies van der Rohe has the same trend as that of Frank Lloyd Wright from the early 1900th to the mid 1930th. The average trend of these three masters goes down in general starting from 1930th.

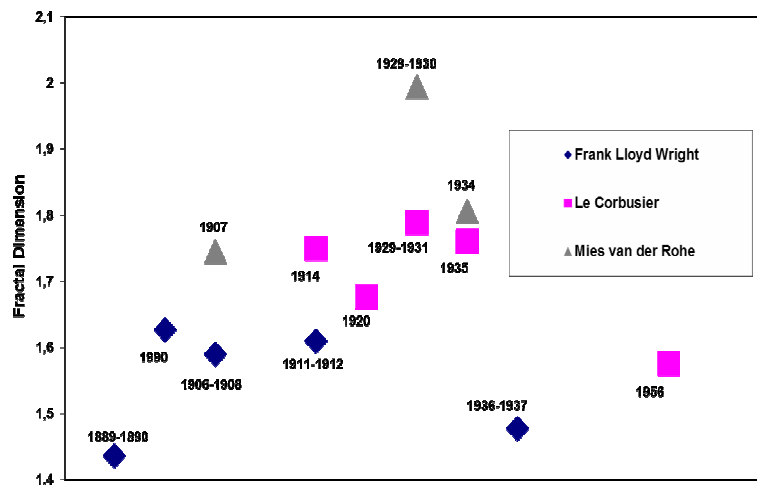


Fig. 8. Fractal dimensions for the masterpieces of three modern architects.

4. Conclusions

This paper has reviewed the fundamental concepts and properties of fractal geometry theory essential to architectural design, as well as the current state of its applications. Fractal geometry has important implications for buildings. The representative review shows that architecture design is not made to be isolated but to anticipate changes in the environment. Accumulation of technological modernisations, destroying, adapting and many changes have caused the design temporal and spatial diversity and complex. More specifically, sustainable development in a building can be looked upon as adaptability and flexibility over time when it comes to responding to changing environment. Chaos and many other nonlinear theories have explained that extremely deterministic and linear processes are very fragile in maintaining stability over a wide range of conditions, whereas chaotic and fractal systems can function effectively over a wide range of different conditions, thereby offering adaptability and flexibility.



In this context, fractal geometry theory offers prescriptive for architecture design. This paper provides a bridge between building engineering and architecture and fractal geometry theory.

References

1. B. Mandelbrot. *Fractals, Form, Chance and dimension*, Freeman, San Francisco, 1977.
2. B. Mandelbrot. *The Fractal Geometry of Nature*. W.H. Freeman and Company, 1982.
3. P.A. Burrough. Fractal dimensions of landscapes and other environmental data. *Nature* 294: 240–242, 1981.
4. K. Weierstrass, On continuous functions of a real argument that do not have a well-defined differential quotient, in G. Edgar, ed *Classics on Fractals*, Addison-Wesley, Reading, Massachusetts, 3-9, 1993.
5. H. von Koch. On a continuous curve without tangents constructible from elementary geometry, in G. Edgar, ed *Classics on Fractals*, Addison-Wesley, Reading, Massachusetts, 25-45, 1993.
6. G. Cantor. On the Power of Perfect Sets of Points. in G. Edgar, ed *Classics on Fractals*, Addison-Wesley, Reading, Massachusetts, 11-23, 1993.
7. M. Barnsley. *Fractals Everywhere*. Academic Press, 1988.
8. H.O. Peitgen. 1988. Fantastic Deterministic Fractals, in: H.O. Peitgen, D. Saupe. *The Science of Fractal Images*, 202, Springer, New York, 1988.
9. J.E. Hutchinson. Fractals and self similarity. *Indiana Univ. Math. J.* 30: 713–747, 1981.
10. C. Bovill. *Fractal Geometry in Architecture and Design*, Birkhauser, Boston, 1996.
11. M. Ebrahimi, E.R. Vrsay. Self-similarity in imaging, 20 years after "Fractals Everywhere", <http://ticsp.cs.tut.fi/images/3/3f/Cr1023-lausanne.pdf>.
12. H.T. Chang. Arbitrary affine transformation and their composition effects for two-dimensional fractal sets. *Image and Vision Computing* 22: 1117-1127, 2004.
13. H. Hamda, F. Jouve, E. Lutton, M. Schoenauer, M. Sebag, Compact unstructured representations for evolutionary topological optimum design. *Appl Intell* 16: 139-155, 2002.
14. M. Batty, P. Longley. *Fractal Cities*, London: Academic Press, 1994.
15. K. Trivedi. Hindu temples: models of a fractal universe. *The Visual Computer* 5: 243-258, 1989.
16. N. Sala. The presence of the Self-similarity in Architecture: some examples. *Emergent Nature - Patterns, Growth and Scaling in the Sciences*, World Scientific 273-282, 2002.
17. C.T. Brown, W.R.T. Witschey. The fractal geometry of ancient Maya settlement. *Journal of Archaeological Science* 30: 1619-1632, 2003.
18. N. Sala. Fractal models in architecture: a case of study. <http://math.unipa.it/~grim/Jsala-workshop.PDF>.
19. W.E. Lorenz. *Fractals and Fractal Architecture*, Mater Thesis, Vienna, 2003.
20. P. Rubinowicz. Chaos and geometric order in architecture and design. *Journal for Geometry and Graphics* 4: 197-207, 2000.
21. http://en.wikipedia.org/wiki/Islamic_architecture.
22. J.S. Cowen. Muslims in China: The mosque. *Saudi Aramco World*. Retrieved 2006-04-08, 30-35, 1985.
23. C.I. Yessios. A fractal studio. *ACADIA '87 Workshop Proceedings*, 1987.
24. S. Durmisevic, O. Ciftcioglu. Fractals in architectural design. *Mathematics and Design*. Javier Barrallo the university of the Basque Country, 1988.



25. K-C. Wen, Y-N. Kao. An analytic study of architectural design style by fractal dimension method, *22nd International Symposium on Automation and Robotics in Construction* ISARC 2005, Italy, 2005,
<http://www.iaarc.org/publications/fulltext/isarc2005-63wen.pdf>





Chaos and Complexity Models and Sustainable Building Simulation

Xiaoshu Lu^{1,3}, Charles Kibert², Martti Viljanen¹

¹Department of Civil and Structural Engineering, School of Engineering, Aalto University, PO Box 12100, FIN-02150, Espoo, Finland

E-mail: xiaoshu@cc.hut.fi

²Powell Center for Construction & Environment, University of Florida, PO Box 115703, Gainesville, Florida 32611-5703 USA

³Finnish Institute of Occupational Health, Finland

Abstract: This paper intends to provide suggestions of how sustainable building simulation might profit from mathematical models derived from chaos and complexity approaches. It notes that with the increasing complexity of sustainable building systems which are capable of intelligently adjusting buildings' performance from the environment and occupant behavior and adapting to environmental extremes, building performance simulation is becoming more crucial and heading towards new challenges, dimensions, concepts, and theories beyond the traditional ones. The paper then goes on to describe how chaos and complexity theory has been applied in modeling building systems and behavior, and to identify the paucity of literature and the need for a suitable methodology of linking chaos and complexity approaches to mathematical models in building sustainable studies. Chaotic models are proposed thereafter for modelling energy consumption, nonlinear moisture diffusion, and building material properties in building simulation. This paper provides an update on the current simulation models for sustainable buildings.

Keywords: Chaos theory, Sustainable building simulation, Energy consumption, Moisture diffusion and Material properties.

1. Introduction

Buildings represent a large share of world's end-use energy consumption. Due to rapid increase in energy consumption in the building sector, the climate change driven by global warming, and rising energy shortage, there is no doubt that renewable energy and sustainable buildings play an role in the future. Today, sustainable buildings are seen as a vital element of a much larger concept of sustainable development that aims to meet human needs while preserving the environment so that the needs can be met not only in the present, but in the indefinite future [1]. Moreover, the concept itself keeps on evolving and resulting in iterations of sustainability [2]. Technically, sustainable buildings require integration of a variety of computer-based complex systems which are capable of intelligently adjusting their performance from the



environment and occupant behavior and intelligently adapting to environmental extremes [2].

With the increasing complexity of building systems, simulation based design and predictive control of building performances are more and more important for a sustainable energy future. Consequently, this makes building performance models more complex and crucial which are heading towards new challenges, dimensions, concepts, and theoretical framework beyond the traditional building simulation theories. It has been suggested that as a basis chaos and complexity theory is valid and can handle the increasingly complexity of building systems that have dynamic interactions among the building systems on the one hand, and the environment and occupant behavior on the other. Here we do not distinguish chaos and complexity theories in this paper even though there has been a debate about their differences [3].

The chaos models have already been applied to some problems in building simulation applications. Chow et al. investigated chaos phenomena of the dynamic behavior of mixed convection and air-conditional systems for buildings with thermal control [4]. Weng et al. applied chaos theory to the study of backdraft phenomenon in room fires [5]. Morimoto et al. studied an intelligent control technique for keeping better quality of fruit during the storage process [6]. For humidity control purpose, the sampled relative humidity data in storage house were measured and analyzed. Chaos phenomenon was identified in such measured relative humidity time series over daytime hours.

In spite of the studies discussed above, the application of chaos theory to building performance simulation, especially to sustainable buildings, is still in its infancy. Building performance simulation models can be roughly classified into either the physical model or the black-box approach. Some may be difficult to categorize in this way. As far as the physical model is concerned, there is a voluminous literature on the models ranging from detailed to local thermal analysis of energy demand, passive design, environmental comfort and the response of control [7,8]. These physical models often require sufficient information on systems, control and environmental parameters for buildings. The output of the model is only as accurate as input data.

Presently many input data for buildings are poorly defined, which creates ambiguity or uncertainty in interpreting the output. This is the general drawback of these models. Therefore, for many practical applications, a black-box approach, a model without internal mechanisms or physical structure, is often adopted. For example, neural networks and fuzzy logic models [9] and time series models [10] which are generally better suited for prediction. However, these models have several limitations. Take neural networks as an example. Firstly, large experimental input and output data are needed in order to build neural networks which can be difficult and expensive to obtain in practice. Secondly, they are susceptible to over-training. Above all, the models have been



criticized as 'black box' model with no explanation of the underlying dynamics that drive the study systems [11].

More specifically, as for sustainable buildings, the current models often lack the long-term economics factors, evolving factors, and flexibility necessary for dynamic predictions. These weaknesses and the current status of sustainable building simulation models have encouraged us to focus instead on a chaos-based model incorporating physical model to enhance our understanding and prediction of building physical behaviour. Chaos theory is characterized by the so-called 'butterfly effect' described by Lorenz [12]. It is the propensity of a system to be sensitive to initial conditions so that the system becomes unpredictable over time. Yet, a chaotic process is not totally random and has broadened existing deterministic patterns with some kind of structure and order [12]. This paper extends the literature by proposing potential chaotic models in sustainable building simulation. Below we describe three such models. The first is building energy consumption model. The second deals with nonlinear moisture diffusion model. The third is related to building material properties.

2. Building Energy Consumption Model

Swan provided an up-to-date review of various simulation models used for modeling residential sector energy consumption and sustainability [13]. Most models rely on input data whose levels of details can vary dramatically. Li presented an overview of literature regarding long-term energy demand and CO₂ emission forecast scenarios [14]. These reviews reflect general modeling approaches currently in existence for sustainable buildings. Two approaches are generally adopted: top-down and bottom-up. The top-down approach utilizes historic aggregate energy values and regresses the energy consumption of the housing stock as a function of top-level variables such as macroeconomic indicators. While the general employed techniques may account for future technology penetration based on historic rates of change, they lack of evolving factors. Hence an inherent drawback is that there is no guarantee that values derived from the past will remain valid in the future, especially given the fact that the levels of details of input data vary significantly [13].

The bottom-up approach extrapolates the estimated energy consumption of a representative set of individual houses to regional and national levels, and consists of two distinct methodologies: the statistical method and the engineering method [13]. Methodologically, extrapolation has been questioned for many good reasons. It is therefore noted that the statistical technique is hampered by multicollinearity resulting in poor prediction of certain end-uses while engineering technique requires many more inputs and has difficulty estimating the unspecified loads [13, 15].



The major disadvantage of these models is their lack of flexibility due to the fact that there is no deterministic structure provided to characterize the input data. In this context, chaos theory offers a solid theoretical and methodological foundation for interpreting the fundamental deterministic structure of the data which present the increasingly complexity of building systems. Karatasou applied chaos theory in analyzing time series data on building energy consumption [16]. The correlation dimension 3.47 and largest Lyapunov exponent 0.047 were estimated for the data, which indicated that chaotic characteristics exist in the energy consumption data set. Therefore, chaos theory techniques, based on phase space dynamics for instance, can be used to model and predict buildings energy consumption.

3. Strong Nonlinear Moisture Diffusion Model

Building envelopes can be susceptible to moisture accumulation which may cause growth of moulds and the deterioration of both occupant health and building materials. A certain duration of exposure conditions, such as humidity, temperature, and exposure time, is required for the growth of organisms and the start of the deterioration process. Critical exposure duration depends on the particular exposure and material. Take a critical moisture level as an example. If the moisture level in the material exceeds the critical level, there is a risk of damage [17] and mould growth [18]. Trechsel summarised that the critical moisture level can be presented as the critical factors such as 'the critical moisture content' and 'the critical accumulative exposure time' [19]. He emphasized that with qualitative criteria it is not possible to assess the risk. Qualitative criteria can be used only if performance limit states are known which need statistical data. Evidence has shown the existence of inherent randomness and nonlinearity in mould growth and the data [18]. Therefore, moisture transfer process manifestly has chaos.

From a physical modelling point of view, heat and moisture transfer phenomena in a medium are governed by heat or diffusion equations which are partial differential equations. For a homogeneous and isotropic medium, the diffusivity coefficient is often assumed to be constant in the entire domain under study. In inhomogeneous media, it depends on the coordinates and even on the temperature [20]. Until now, there is no model that considers time-dependent diffusivity. However, time-dependent diffusivity, which might be due to the time-dependent perturbation of environment such as sudden structural change, is an optional explanation for the critical moisture level.

Yao studied one-dimensional Kuramoto–Sivashinsky (KS) equation, a nonlinear partial differential equation, in the hope of clarify the role of nonlinear terms the their consequences [21]:

$$u_t + 4u_{xxxx} + \lambda(u_{xx} + uu_x) = 0 \quad (1)$$



Nonlinear stability analysis was investigated with respect to time-dependent λ . After certain time ($t=4$), the chaotic behavior was observed.

It is not difficult to see that the KS equation and heat or diffusion equations do not differ significantly. Thus the KS equation example is expected to more easily expose major points and hopefully identify open questions that are related to the critical moisture level or mould phenomena in relation to chaos phenomena.

4. Material Properties Model

Porous materials have played a major role in building engineering applications. They are important elements of heat and mass conservation for buildings and have been extensively studied [22]. A porous material has a unique structure of complex geometry which is characterized by the presence of a solid matrix and void phases with porosity. The heat and mass transport behavior of porous media is largely governed by the interactions among coexisting components. These interactions occur through interfaces. Theoretically, transport processes in a porous medium domain may be described by a continuum at the microscopic level, based on the Navier-Stokes equations for example, as taking into account the multi-phase nature of the domain. However, for most cases this is impractical because of the inability to describe the complex geometry and trace a large number of interfacial boundaries for the porous domain. Therefore, the porous media models are often constructed through averaging the governing equations, for example Navier-Stokes equations, in continua at the microscopic level over a length scale such as representative elementary volume [23]. During the averaging process some integrals are performed, introducing a weighted average of the relevant variables, parameters and properties which can be determined by laboratory and field measurements.

However, both laboratory and field measurements are often tedious, time consuming and expensive. This has motivated researchers toward the development of mathematical modeling approaches from routinely measured properties. In general, three types of mathematical models are used to model material transport properties: empirical, bundle of tubes, and network models [24]. The empirical models provide a set of analytical functions to fit the measurement data for material properties. The model has the advantage of simplicity but the disadvantage of limited flexibility and adjustability and hence low reliability.

Depending on how they represent the geometry of the material, both the bundle of tubes and the network models rely on the pore structure, such as distribution, connectivity and tortuosity, to derive the material's transport properties. These models are also called pore-distribution models and were pioneered by Fatt [25-27]. The bundle of tubes model approximates the pore structure in a fairly simple way, for example a set of parallel tubes [24]. Networks models



approximate the pore structure by a lattice of tubes and throats of various geometrical shapes on the microscopic scale. Creating a network model is laborious and not straightforward especially for 3D models [28].

Most importantly, these models, or current state of property modeling approaches, are case sensitive depending on the excited boundary or the environment. Therefore, variations of material properties under different conditions are large, which has been a challenge for modelers. On a longer time scale, large quantity of data is often needed to build the model and this can be difficult and expensive to accomplish in practice. In addition, in a wide environment setting when different environmental phenomena overlap, material properties become complicated and difficult to predict [29]. This is due to the lack of a deterministic structure or a core mechanism characterizing the material transport properties. Chaos theory provides a set of diagnostic tools to exploit the underlying structures that appear random or unpredictable under traditional analysis.

Stazi et al. applied chaos theory to investigate the hygrometric properties of building materials, such as adsorption and suction curves [29]. The constitute relationship of material's water content and the environment humidity, the core of this study, was modelled on the basis of fractal geometry using the material's pore radius as:

$$u = u(\phi, D) \quad (2)$$

where u is the hygroscopic content inside the material and ϕ the relative humidity of the material. Their relationship was determined through finding the material's fractal dimension of water inside the pores, D , which was 2.5265 for mortar [29].

The novelty of the model lies in its ability to construct the relationship between the water content inside the material and the relative humidity of the environment based on the material's geometric property characterized by fractal dimension. The knowledge of the fractal dimension of the pore spacing in a porous medium is enough to work out the suction and adsorption curves of the material. It is, therefore, natural for us to consider chaos theory as a source of inspiration to envisage the importance of the concerns raised in research in different fields of building material properties.

5. Conclusions

This paper aims to provide a suggestion to update the current status of simulation models for sustainable buildings. Three chaotic models are proposed. The first is the building energy consumption model as chaotic characteristics has been observed in the specific energy consumption data set. The second is dealing with investigation of nonlinearity of the moisture diffusion model. The



third model involves the investigation of material physical properties. The conclusion to be drawn is that chaos theory may reflect real situations, deepen our understanding, and make predictions more realistic in sustainable building simulation.

References

1. Wikipedia-The Free Encyclopedia, Sustainable Development. http://en.wikipedia.org/wiki/Sustainable_development, June, 2008.
2. C. Du Plessis. Thinking about the Day after Tomorrow. New Perspectives on Sustainable Building. *Rethinking Sustainable Construction 2006 Conference*, Sarasota, Florida, USA 2006.
3. R.C. Zahra. From Chaos to Cohesion—Complexity in Tourism Structures: An Analysis of New Zealand's Regional Tourism Organizations. *Tourism Management* 28: 854-862, 2007.
4. K. Chow, G. Xin, A. Liu. A Further Study on Multiple Attractors of Mixed Convection in Confined Spaces. *Building and Environment* 40: 1021-1031, 2005.
5. W.G. Weng, W.C. Fan. Nonlinear Analysis of the Backdraft Phenomenon in Room Fires. *Fire Safety Journal* 39: 474-464, 2004.
6. T. Morimoto, Y. Hashimoto. An Intelligent Control for Greenhouse Automation, Oriented by the Concepts of SPA and SFA- An Application to a Post-harvest Process. *Computers and Electronics in Agriculture* 29: 3-20, 2004.
7. X. Lu, D. Clements-Croome, M. Viljanen. Past, Present and Future Mathematical Models for Buildings: Focus on Intelligent Buildings (Part 1). *Intelligent Building International* 1:22-38, 2009.
8. X. Lu, D. Clements-Croome, M. Viljanen. Past, Present and Future Mathematical Models for Buildings: Focus on Intelligent Buildings (Part 2). *Intelligent Building International* 2:131-141, 2009.
9. A.I. Dounis, C. Cariscos. Advanced Control Systems Engineering for Energy and Comfort Management in a Building Environment : A Review. *Renewable and Sustainable Energy Reviews* 13: 1246-1261, 2009.
10. D. Popescu, F. Ungureanu, A. Henandez-Guerrero. Simulation Models for the Analysis of Space Heat Consumption of Buildings. *Energy* 34: 1447-1453, 2009.
11. M. Aydinalp, V.I. Ugursal, A. Fung. Modeling of the Appliance, Lighting, and Space-cooling Energy Consumptions in the Residential Sector Using Neural Networks. *Applied Energy* 72: 87-110, 2002.
12. E. Lorenz. Deterministic Nonperiodic Flow. *Journal of Atmospheric Science* 20: 130-141, 1963.
13. L.G. Swan, V.I. Ugursal. Modeling of End-use Energy Consumption in the Residential Sector: A Review of Modeling Techniques. *Renewable and Sustainable Energy Reviews* 13: 1819-1835, 2009.
14. J. Li. Towards a Low-carbon Future in China's Building Sector-A Review of Energy and Climate Models Forecast. *Energy Policy* 36: 1736-1747, 2008.
15. B.M. Larsen, R. Nesbakken. Household Electricity End-use Consumption: Results from Econometric and Engineering Models. *Energy Economics* 26: 179-200, 2004.
16. S. Karatasou, M. Santamouris. Detection of Low-dimensional Chaos in Buildings Energy Consumption Time Series. *Communications in Nonlinear Science and Numerical Simulation* 15: 1603-1612, 2010.



17. V. Leivo, J. Rantala. Moisture Behaviour of Slab-on-ground Structures in Operating Conditions: Steady-state Analysis. *Construction and Building Materials* 22: 526-531, 2008.
18. H.J. Moon, G.A. Augenbroe. A Mixed Simulation Approach to Analyse Mold Growth under Uncertainty. *Ninth International IBPSA Conference*, Montreal, Canada, August 15-18, 2005.
19. H.R. Trechsel. Moisture Analysis and Condensation Control in Building Envelopes. *ASTM Manual* 40, Philadelphia, USA, 2001.
20. R.C. Gaur, N.K. Bansal. Effect of Moisture Transfer across Building Components on Room Temperature. *Building and Environment* 37: 11-17, 2002.
21. L-S, Yao. Is a Direct Numerical Simulation of Chaos Possible? A Study of Model Nonlinearity. *International Journal of Heat and Mass Transfer* 20: 2200-2207, 2007.
22. X. Lu. Modeling Heat and Moisture Transfer in Buildings: (I) Model Program. *Energy and Buildings* 34: 1033-1043, 2002.
23. J. Bear. *Dynamics of Fluids in Porous Media*, Elsevier: New York, NY, USA, 1972.
24. F.A.L. Dullien. *Porous Media: Fluid Transport and Pore Structure*, Academic Press: New York, 1979.
25. I. Fatt. The Network Model of Porous Media I. Capillary Pressure Characteristics. *Trans. AIME*. 207: 144-159, 1956.
26. I. Fatt. The Network Model of Porous Media II. Dynamic Properties of a Single Size Tube Network. *Trans. AIME*. 207: 160-163, 1956.
27. I. Fatt. The Network Model of Porous Media III. Dynamic Properties of Networks with Tube Radius Distribution. *Trans. AIME*. 207: 164-181, 1956.
28. W.B. Lindquist. Network Flow Model Studies and 3D Pore Structure. *Contemporary Mathematics* 295: 355-366, 2002.
29. A. Stazi, M. D'Orazio, E. Quagliarini. In-life Prediction of Hygrometric Behaviour of Buildings Materials: An Application of Fractal Geometry to the Determination of Adsorption and Suction Properties. *Building and Environment* 37: 733-739, 2002.